2-14-2014

Spectroscopic Studies of Conformation and Packing in Polythiophenes

Edwards Niles

Edwards T. Niles
_____
Candidate

Department of Chemistry
_____
Department

This dissertation is approved, and it is acceptable in quality and form for publication:

Approved by the Dissertation Committee:

 Dr. Jonh Grey, Chairperson
_____

Dr. Yang Qin
_____

Dr. Terefe Habteyes
_____

Dr. David Dunlap
_____

_____

_____

_____

_____

Spectroscopic Studies of Conformation and Packing in Polythiophenes

By

EDWARDS T. NILES

B.S. Chemistry, University of New Mexico, 2005

DISSERTATION Submitted in Partial Fulfillment of the

Requirements for the Degree of

Doctor of Philosophy

Chemistry

The University of New Mexico Albuquerque, New Mexico

July, 2013

DEDICATION

The work in this thesis is dedicated to Raymond R. Niles III. I wish you were here.

ACKNOWLEDGMENTS

I would like to thank those who have made this degree become a reality. First, my deep appreciation and gratitude to my advisor, Professor John K. Grey, he patiently provided the vision, and advice necessary for me to succeed in completing and defending my thesis. I express my appreciation to Karen Ann Smith and the NMR facility for the financial support and the opportunity to learn how to maintain, service, and repair NMR spectrometers and super conducting magnets. I would also like to recognize and thank my committee members, Dr. Yang Qin, Dr. Terefe Habteyes and Dr. David Dunlap who took time out of their busy schedules to assist me in completing my degree. Dr. David Tierney recognized my potential as a chemist and gave me years of laboratory experience; for this I am truly grateful.

I would like to thank the people I worked with in the labs. First of all, Yongqian Gao for all his help and guidance in my introduction to hands-on polymer chemistry and homebuilt spectrometers. Next, thank you to Eric Martin, Adam Wise, Jian Gao, Alan Thomas, Tom Martin, for their advice and help in the daily contemplations of physical chemistry. To Dr. Kirk and members of his group, I would like to acknowledge my appreciation for their help with EPR measurements, Eileen Dueler for training on the X-ray diffractometer, the guys at CRLS for their help with my weekly LN_2 fills, and Fred Fuchs for his help fixing the day to day problems in the labs.

I wish to thank my parents and sisters; I owe them everything and want them to know how much I love and appreciate their support throughout my life. To my children, who are my inspiration and driving force, whose love and encouragement has allowed me to finish this journey; thanks for hanging in there with Dad.

The work to get this degree was demanding and finishing it as a single parent of three great children has been the most challenging time of my life. There have been many ups and downs in my path towards this educational goal and many influential people have shared this journey with me and I would like to thank those who are not cited for helping me achieve this goal.

Spectroscopic Studies of Conformation and Packing in Polythiophenes

BY

Edwards Niles

B.S, Chemistry

University of New Mexico, 2005

Ph.D., Chemistry

UNIVERSITY OF NEW MEXICO, 2013

ABSTRACT

This thesis employs variants of spectroscopic techniques to evaluate intermolecular interactions between P3HT chains in solution and in the solid state. Emphasis was put on understanding not only how intermolecular interactions within P3HT chains affect electronic properties, but also to assess changes due to the addition of weak and strong electron acceptors. To this end, optical and magnetic spectroscopies were focused on to correlate observed changes in electronic properties to physical changes in the polymer structure.

To assess changes in intermolecular interactions, self-assembly was used to form P3HT nanofibers and were studied using resonance Raman, and transient absorption, and temperature- and pressure-dependent photoluminescence spectroscopy. Nanofiber spectra revealed an increase in intrachain order, a change in aggregation and the utility of self-assembly to control P3HT chain interactions.

Resonance Raman, and optical absorption of different wt/wt loadings of P3HT/PCBM blends were measured to study the effect of weak acceptor interactions on thin film morphology and photocurrent output in donor/acceptor blends. The changes in optical spectra lineshapes were fit with the weakly coupled H-aggregate model to reveal decreases in the relative amounts of aggregated/unaggregated P3HT chains as weight fraction of PCBM increased.

Electron paramagnet and nuclear magnetic resonance were combined with pre-resonance Raman and optical absorption to evaluate charge transfer salts. The electronic structure was altered the addition of a strong electron acceptor that formally oxidized a

segment of the polymer chain. Paramagnetic signals were observed with EPR after radicals formed in donor/acceptor blends that coincided with observations of new low energy absorption bands and changes in chemical shift. The Raman spectra revealed increased backbone planarity after ground state complexation and led to the conclusion that strong acceptor blends enhanced planarity of polymer chains after charge separation.

TABLE OF CONTENTS

LIST OF FIGURES

LIST OF ABBREVIATIONS

A	Electron Acceptor
A_{0-0}	Absorption intensity of principle electronic transition
AFM	Atomic Force Microscopy
BHJ	Bulk Heterojunction
CCD	Charge Coupled Detector
cm^{-1}	Wavenumber
CSS	Charge Separate State
CT	Charge transfer
CTC	Charge Transfer Complex
D	Electron donor
DDQ	2,3-Dichloro-5,6-dicyano-1,4-benzoquinone
E_{0-0}	Absorption energy of principle electronic transition
EQE	External Quantum Efficiency
EPR	Electron Paramagnetic Resonance
eV	electron Volt
HOMO	Highest Occupied Molecular Orbital
h	Planck constant
J_0	Coupling constant
LUMO	Lowest Unoccupied Molecular Orbital
MDMO-PPV	Poly[2-methoxy-5-(3′,7′-dimethyloctyloxy)-1,4-phenylenevinylene]
NMR	Nuclear Magnetic Resonance
nm	Nanometer

PCBM	[6, 6]-phenyl-C61-butyric acid methyl ester
PEDOT: PSS	Poly (3, 4-ethylenedioxythiophene) poly (styrenesulfonate)
PL	Photoluminescence
PPV	Poly-phenylenevinylene
P3HT	Poly(3-hexylthiophene-2,5-diyl)
r-Ra	regio-Random
r-Re	regio-Regular
F_4-TCNQ	2,3,5,6-tetrafluoro-7,7,8,8-tetracyanoquinodimethane
TCSPSC	Time Correlated Single Photon Counting
UV-VIS-NIR	Ultraviolet-Visible-Near Infrared
wt/wt	Weight\Weight
W	Exciton bandwidth
XRD	X-ray Diffraction

CHAPTER 1

Introduction

1.1 Overview

Intermolecular interactions between conjugated polymer chains in aggregates and donor/acceptor complexes are examined using spectroscopy. In particular, optical and magnetic spectroscopies are used to reveal how physical and electronic structures in polymers and polymer/acceptor blends change with various processing methods. The research presented here emphasizes understanding how changes in the conformation and packing interactions of poly(3-hexylthiophene-2,5-diyl) (P3HT), a prototypical optoelectronic polymer, affect its electronic structures and coupling. P3HT is one of the few conducting polymers that can form crystalline stacks of planar polymer chains in flexible thin films cast from solutions. [1-6] P3HT is considered a prototypical material for organic optoelectronics, such as solar cells, field-effect transistors and sensors, owing largely to its high optical absorptivity and ordered conformations that promote efficient charge transport.[4,5] However, the choice of processing techniques modulates the degree of crystallinity as well as the sizes of these crystalline regions and therefore bulk material performance.[1-3] The nature and degrees of polymer chain interactions vary substantially throughout thin films, the common functional forms of these materials, which affect charge and energy transfer processes. Control of P3HT conformation and packing is vital for optimizing its performance in device applications. However, a fundamental

1

understanding of the relationships between molecular conformation and packing and electronic properties is first needed.
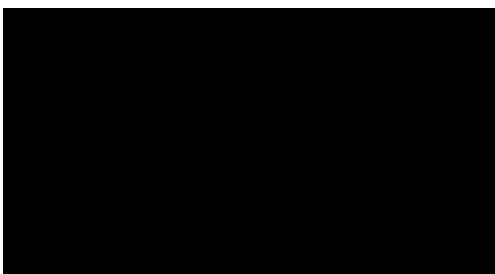
Figure 1.1: Structure of Poly(3-hexylthiophene-2,5-diyl) (P3HT).

The work presented herein involves novel self-assembly techniques which regulate polymer chain interactions in P3HT aggregates and allow for exquisite control of coupling between photoexcitations between the established H- and J-aggregate type limits. Additionally, the presence of other electron accepting molecules used in solar cells or other additives used to dope polymers can have a large effect on the physical and electronic structures of P3HT[7-10]. For example, the interactions between P3HT with weak and strong electron acceptors are studied in detail in chapters four and five which show a wide range of tunability for the electronic properties of P3HT. [7,8,11]

1.2 Background

Polymers have been utilized in chemical applications for nearly a century; however it was not until the 1970's that the conductive properties of conjugated polymers were documented by Shirakawa et al.[4] Conducting polymers typically consist of chains

of conjugated segments of a statistically varying number of monomer units demarcated by torsional twists and defects in the polymer backbone. The two main structural characteristics of electronically or optically active polymer design are a conjugated backbone for photon absorption and side chain substitution for solubility.[12,13] Solution-processed thin films of polymers with these characteristics have demonstrated their viability as active layers for a variety of optoelectronic applications including: light-emitting diodes (LED), field effect transistors (FET), and organic photovoltaics (OPV). [13-24] However, reliable control of material performance in these functional forms has remained difficult due to the random nature of molecular conformations, packing, and morphology.

1.3 P3HT

P3HT is a prototypical conjugated polymer that has seen considerable use in FET applications due to its unusually high crystallinity. It is this high degree of crystallinity that gives this polymer its relatively high conductivities (charge mobilities). [6,25,26] In the early 2000's, P3HT began to see use in OPV applications; and when blended with soluble fullerene derivatives, has served as the benchmark OPV polymer for a number of years.

Since the first uses of P3HT in FET and OPV applications, extensive studies have been conducted on its optoelectronic properties. A large number of these studies have been focused on its charge transport characteristics, the dependence of these characteristics on aggregation, and its electron donating ability in OPV devices.[27-33] Like other conjugated polymers, material performance depends largely on the conditions in

which they are processed. This translates into large variations in electronic spectra as well as device performance, namely, solar cell power conversion efficiency. Although a consensus on P3HT packing and aggregate microstructure has been reached, e.g., characteristic π-stacking face to face distances of ~3.8 Å in crystalline aggregates,[26,34-43] the impact of subtle changes of conformations within these structures are still not entirely understood. Understanding chain interactions in ordered regions and the role disordered chains have on aggregates is an important step to develop a clearer picture of how polymer microstructures affect optical and electronic properties.

Regio-regularity of P3HT also plays a large role in its ability to aggregate. For example, P3HT with >95% head-to-tail arrangement of monomers is generally considered to be regio-regular and can most readily form crystalline aggregates. On the other hand, regio-random samples have no well-defined arrangement and are typically considered to adopt only random coil or, solution-like conformations. These aspects are considered carefully in this thesis and it is shown that the amounts of ordered and disordered species within a sample will impact its properties and performance.

Perhaps the most widely used physical technique to distinguish between ordered and disordered (crystalline and amorphous) P3HT is optical spectroscopy. Optical absorption and photoluminescence offer detailed views of microstructure in P3HT materials and are very simple in nature to use. P3HT aggregates exhibit partially resolved vibronic structure in the dominant C=C symmetric stretching vibration of the backbone. Moreover, the 0-0 vibronic transition is modulated by the type of exciton coupling in crystalline aggregates. This, in turn, is dependent on the degree of order

(planarity) of monomers within the P3HT π-stack. Conversely, spectroscopic signatures of disordered P3HT chains are broad, featureless optical lineshapes significantly blue-shifted from aggregate transitions.[27,44-48]

More recently, Gao et al, demonstrated that resonance Raman spectroscopy of P3HT systems can be used to discern not only the amounts of crystalline and amorphous species, but also their excited vibrational displacements and dynamics.[27,28,49] The Raman approach avoids complications from overlapping transitions and Franck-Condon broadened lineshapes mainly owing to the much faster timescales of these transitions compared to optical spectra. This thesis employs variants of these techniques and even approaches the single molecule level to understand how P3HT packing interactions are affected by structural and electronic perturbations.

1.4 P3HT Chain Interactions

Understanding the alignment and interaction of chains in aggregates can be simplified if we consider the transition dipole moment of a monomer and the effect of dimer formation. The arrows shown in Figure 1.2 represent the interacting dipoles in an energy level diagram. The interactions result in the excited state energy level splitting into exciton states with discrete allowed and forbidden transitions.[2,50-52] Allowed electronic transitions, shown with colored vertical lines, result from in-phase alignment of dipoles. Dipole interactions with net transition dipole moment of zero result in forbidden transitions. The diagram depicts two types of aggregation found in P3HT, "H" and "J" which are common in conjugated polymers. The lowest energy exciton state is

the allowed transition for the head-to-tail alignment shown with red arrow. This describes the coupling in J-aggregates with alignment of transition dipoles like boxcars linked on a train.[50,51] Conversely, the high energy state is the allowed transition in the face-to-face alignment shown with blue arrow. This describes the card stacking alignment of transition dipoles in H-aggregation. When multiple transition dipoles interact in aggregates the features of the electronic transition spectra vary with the net vector sum of the dipole interactions. The allowed and forbidden transitions determine the optical absorption and emission characteristics of the aggregate.
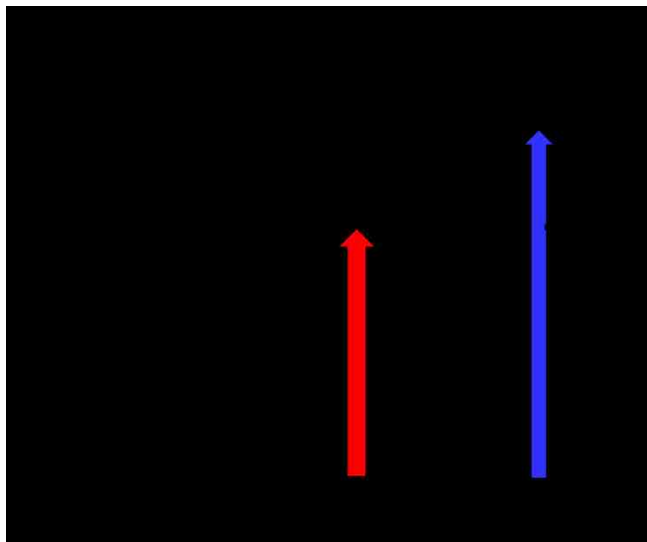
Figure 1.2: Energy diagram for exciton band structure that arise from alignments of transition dipoles in molecular dimers.

1.5 Lineshapes of Optical Spectra as Diagnostics for Aggregation

The intensity profile of an optical lineshape can be described by a Poisson distribution, Equation 1.1, in its simplest form (i.e., harmonic approximation).

$$I_{0 \to m} \approx (\hbar \omega_{vib})(S^m e^{-S}/m!) \qquad (1.1)$$

Where m denotes the phonon level quantum number, ω_{vib} is the phonon mode coupled to the electronic transition, and S is the Huang-Rhys (HR) factor given in Equation 1.2.

$$S = \Delta Q^2/2 \qquad (1.2)$$

S represents the electron-phonon coupling and ΔQ is the nuclear displacement (distance between harmonic potential energy surfaces of the excited and ground electronic states). For a single phonon mode the relative intensity of overtones is varied by only nuclear displacement and the quantum transition. However, molecular dipole-dipole interactions of the polymer chains form different amounts and types of aggregates that affect electronic transition characteristics. Photon absorption in conjugated polymers results in an electronic transition between π bonding and π^* anti-bonding orbitals. Many polymer systems have strong coupling between vibrational and electronic degrees of freedom that result in a vibronically excited central molecule that is surrounded by molecules that are vibrationally but not electronically excited.[51] This can be easily visualized as a bowling ball moving across bed springs (for a detailed description, see references 32,33,44,47,51) The compressed spring directly under the ball resembles the electronically excited molecule, while the partially compressed neighboring springs resemble vibrationally excited molecules. This coupling results in optical spectra with non-Poissonian lineshapes[32,33,44,51] owing to the formation of exciton states as discussed above.

To understand how coupling affects optical transitions, the model of weakly interacting H-aggregate states was developed by Spano and co-workers[32,33,44,47,51] and provides a theoretical lineshape analysis that specifically accounts for aggregation effects. The theoretical parameters can be iteratively adjusted to fit experimental data as discussed below and in chapters two, three and four. The model focuses on how molecular dipole-dipole interactions in different packing conformations of polymer chains effect electronic transition properties such as changes in relative overtone intensity in absorption and emission spectra that results from an ensemble average of different interactions of polymer chains.

In aggregates the excited state level of a molecule is split into high and low energy exciton states as describe above. The energy difference of the exciton states is a function of the electronic coupling, J_0 which reduces exponentially as the separation between faces of the polymer chains increases. P3HT commonly forms H-aggregates in thin films and the deviations from a Poisson distribution in absorption spectra lineshape can be modeled with Equation 1.3.

$$A \propto \sum_{m=0}(e^{-S}S^m/m!)\left(1 - (We^{-S}/2E_p)G_m\right)^2 \Gamma\left(\hbar\omega - E_{00} - mE_p\right) \quad (1.3)$$

Where A is the absorption intensity, J_0 is represented by the exciton bandwidth parameter $W = 4J_0$, G_m is the sum of all transitions from n to m; $G_m = \sum_{m\neq n} S^m/n!\,(n-m)$, and Γ represents a Gaussian inhomogeneous line shape function. Since exciton bandwidth is dependent upon chain order and packing, one of the most commonly used features of the H-aggregate model is to determine the magnitude of W to describe aggregation which,

can be estimated from the absorption intensity ratio of the fundamental transition, (A_{0-0}) to the first overtone (A_{0-1}) with Equation 1.4.

$$A_{0-0}/A_{0-1} \approx \left(\left(1 - (0.24W/E_P)\right)/\left(1 + (0.73W/E_P)\right)\right)^2 \qquad (1.4)$$

Where E_p denotes the intrachain phonon coupled to the electronic transition. For P3HT E_p is the frequency of C=C symmetric vibration. In H-aggregates, the ratio is <1and W is inversely proportional to $(A_{0-0})/(A_{0-1})$ ratio; larger ratios indicate increased intramolecular order and smaller values are indicative of an increase in H-aggregation. The opposite trends are expected for J-aggregates which are very rare for P3HT. The magnitude of W is often used to qualify the degree of crystalline quality in P3HT aggregates.[27,32,45,46,53] In fact, the weakly coupled H-aggregate model of Spano has been successfully used to deconvolute the contributions from aggregates as well as estimate the coupling strength and intrachain order within aggregates.[32,33] The fits of H-aggregate lineshapes to P3HT absorption spectra have revealed microscopic details about the interplay between polymer structure and electronic properties. Figure 1.3 shows simulated optical spectra lineshapes using the Spano model where interchain exciton coupling is varied between H- and J-type limits. Importantly, this model assumes that the magnitude of exciton coupling is smaller than the frequency of the dominant displaced phonon vibration in P3HT (i.e., C=C mode).
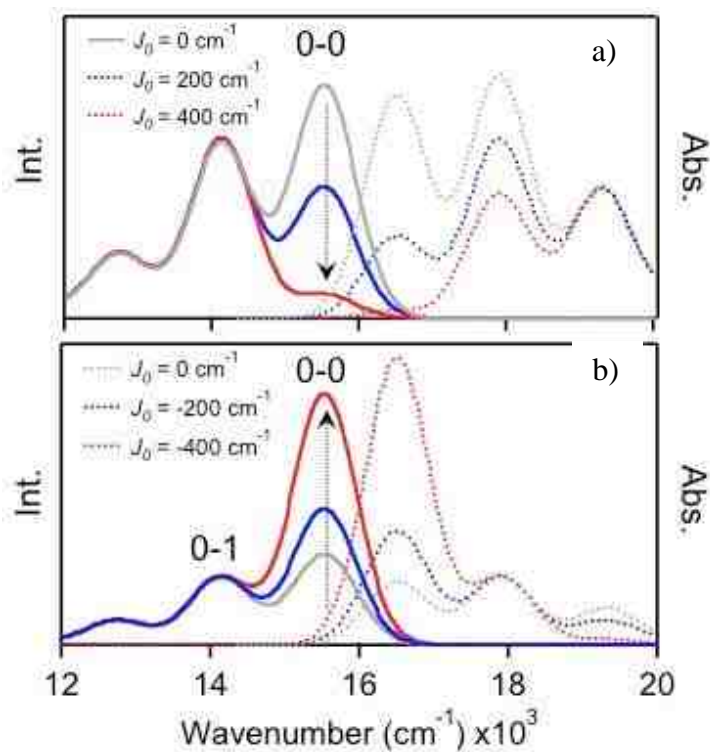
Figure 1.3: Theoretical optical spectra for H- and J-aggregates: a) H-aggregate, b) J-aggregate . Emission is the solid trace, absorption is the dotted trace.

Because of the stochastic nature of P3HT samples (i.e., polydispersity, etc.) and processing, disorder usually limits aggregates' degree of crystallinity and size. Consequently, the intrachain order, or planarity, is low, suggesting large torsional displacements between monomers. This situation results in limited exciton coherence and enhances interchain communication between P3HT segments resulting in the prevalent H-aggregate type exciton. However, when crystallization of P3HT is carefully controlled, large enhancements of intrachain order are possible and the exciton coupling switches from the common H-type to the elusive J-type. This is achieved through self-

assembly techniques to spatially control ordered segments of the polymer chain by forming ordered nanostructures in solution. These ordered nanostructures often take the form of nanofibers. This approach is unique in that it can selectively exclude disordered chains from the aggregate thereby reducing stacking faults.[54] Namely, the assembly mechanism selects high molecular weight chains with high regioregularity, ensuring high intrachain order. This method offers greater potential to control electronic coupling and predict order by pre-forming aggregates in solution and thus avoiding diversity of polymer chain interactions that result from solution casting procedures. Figure 1.4 displays the experimental absorption spectrum of NF solution and fit using a weakly coupled aggregate model. As well as estimating the couple constant of aggregates in thin film the aggregate model can also be used to deconvolute the ratio of ordered/disordered conformations from absorption. The fit spectrum is subtracted from experimental spectrum then dilute solution P3HT spectra are scaled to the onset and peak absorbance of difference spectrum. The dilute solution spectrum is fit with a Gaussian function and the order/disorder ratio can be estimated by integrating the curves.
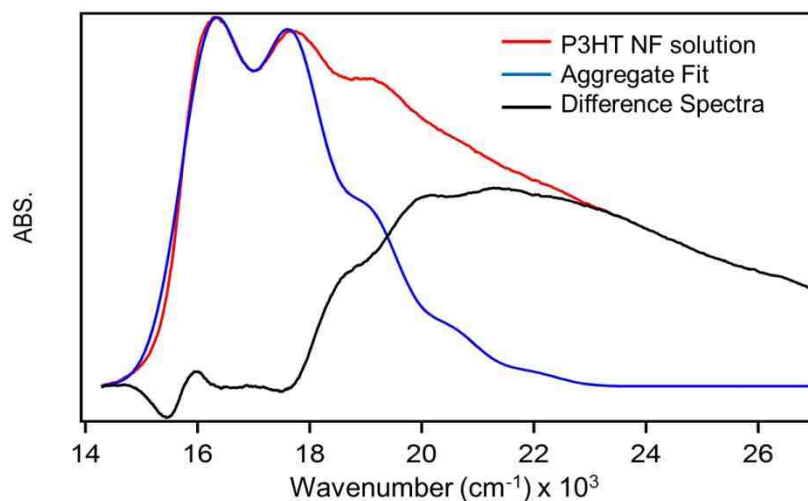
Figure 1.4: Experimental absorption spectrum of NF solution and fit using a weakly coupled aggregate model. Fit spectra were subtracted and difference spectrum was fit with Gaussian curve to estimate disorder.

1.6 Donor/Acceptor Blends

To enhance a conducting polymer's capability to convert photons to electrical energy for various OPV applications, electron acceptors can be added.[5,55,56] The strength (~electron affinity) determines the type of interaction with P3HT as well as the impact on the conformation and packing state. For example, weak acceptors, such as soluble fullerenes, are blended with polymers to form an OPV active layer. This is most readily achieved by simple solution phase blending of polymer donors (*D*) and acceptors (*A*), where casting into thin films yields a bulk heterojunction (BHJ) layer consisting of an interpenetrating network of interfaces.[57-64] In other settings, the P3HT electronic structure can be altered by adding a strong electron acceptor which formally oxidizes a

12

segment of a polymer chain. [65,66] Both weak and strong acceptors have a significant impact on the ability of P3HT to aggregate as well as the conformations of chains within these structures. A goal of this research is to understand not only how intermolecular interactions within pristine P3HT chains affect electronic properties but also to assess changes due to the addition of weak and strong acceptors used in various device applications. Of particular interest is the manner in which the different aforementioned electron acceptors interact with the distinct polymorphs of P3HT.

1.7 Charge Transfer Complexes

Addition of an electron acceptor to P3HT results in a molecular interface that can be understood in terms of the more common semiconductor band theory. Briefly, when a significant energetic offset exists between a donor and acceptor a charge transfer interaction exists which modifies the electronic structures of the pristine molecules. These so-called charge transfer complexes (CTC) play a vital role in determining important performance figures or merit of OPV devices but are poorly understood. CTC's are generally thought of as ground state interactions at the interface between the polymer and acceptor. [67,68] The CTC strength is determined by the relative energetic offset of the P3HT highest occupied molecular orbital (HOMO) and acceptor lowest unoccupied molecular orbital (LUMO) and is best described according to Mulliken charge transfer theory. [65,69] Excited state interactions are also possible, and are in fact the basis for OPV operation. Equations 1.5a and b describe two energy states of the CTC: the ground state (Ψ_G) and the excited state (Ψ_E) after photon absorption.

13

$$\Psi_G = C_1\psi_{(D,A)} + C_2\psi_{(D^+-A^-)} \tag{1.5a}$$

$$\Psi_E = C_4\psi_{(D^+-A^-)} - C_3\psi_{(D^{*+},A^{*-})} \tag{1.5b}$$

Where the coefficient C_n are the population of each state: $\psi_{(D,A)}$ describes the pristine donor and acceptor ground states, $\psi_{(D^+-A^-)}$ describes a state with energy transfer from D to A, and $\psi_{(D^{*+},A^{*-})}$ describes a charged radical state of the D and A. In the excited state the electron hole pair is separated to form charged molecules that have unpaired electrons, D^{*+} and A^{*-}. Figure 1.5 displays a schematic of the photoexcited charge transfer process at a D/A interface. Frame I represents an electron-hole pair formed after photon absorption. Frame II is the state after energy transfer with a bound electron-hole pair, and frame III represents the charge separated state with unpaired electron on D and A.

Paramagnetic resonance signals from both the radical species formed at the D / A interfaces have been observed in light induced electron paramagnetic resonance (LEPR) studies on P3HT and other conducting polymers.[70-74] However the sub-nanosecond time scales of the electronic transition make it difficult to measure and record changes in the molecular system that result from charge separation after photoexcitation.[76,77]
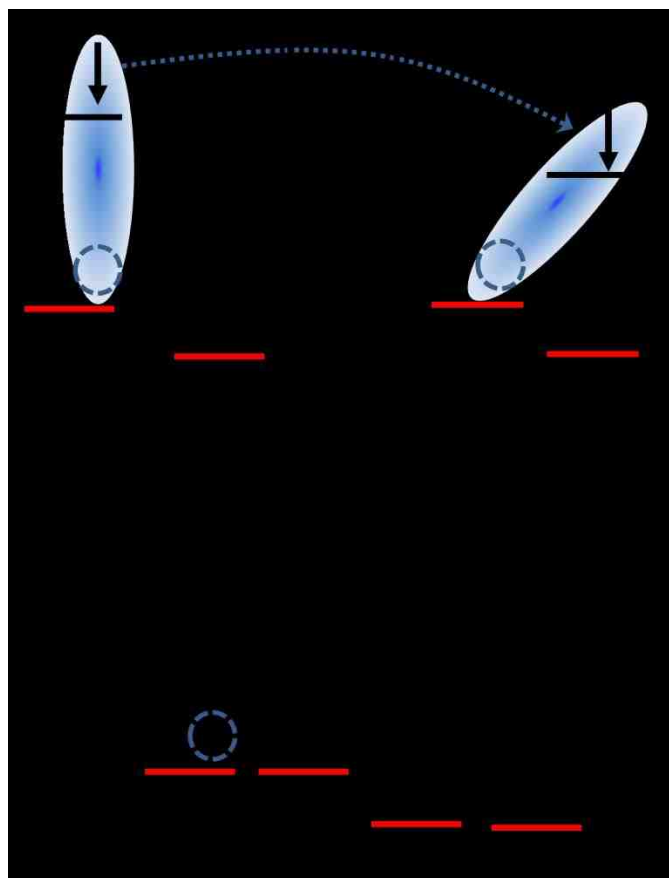
Figure 1.5: Schematic of photoexcited charge transfer process at D/A interface.

The kinetically unstable CTC states are important diamagnetic intermediates in the generation of free charge carries from bound electron hole pairs (excitons).[75] To follow the extent of interactions in D/A blends the population of the ground or excited state CTC, (C_2) or (C_4), could be monitored from a low energy absorption unique to the CTC state with optical spectroscopy.[76-79] However, analysis of the charge transfer state is difficult; it has a small absorption cross section and is often not radiatively coupled to other states which results in low signal to noise ratio that renders spectroscopic

measurements difficult to interpret. Evaluation of the extent and identity of electronic transitions and phonon modes displaced in the CTC has important implications for charge and energy transfer in OPV's. Interactions of D/A systems with energetically favorable charge transfer in the ground state may be used to form an analog of the excited state CTC to better understand the charge transfer state and the affects it has on donor structure.

1.8 Strong Acceptors

A simple redox reaction in Equation 1.6 describes the mechanism of intermolecular electron transfer from the mixing of states to form a charge transfer salt.[75,65]

$$D + A \rightleftarrows [D^+, A^-] \rightleftarrows D^{*+} + A^{*-} \tag{1.6}$$
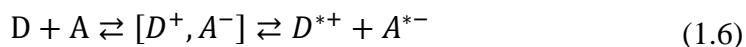
The rate of electron transfer in the formation of $[D^+, A^-]$, the CTC state, is described by an Arrhenius type process[80,81] with the oxidation potential of the donor and the electron affinity of the acceptor as the energy differences. Figure 1.6 shows an energy level diagram of the potentials for P3HT, PCBM and 2,3,5,6-tetrafluoro-7,7,8,8-tetracyanoquinodimethane (F_4-TCNQ). F_4-TCNQ is a small molecule strong acceptor that can spontaneously react and support integer electron transfer from the donor to form charged D and A species with unpaired electrons.[65,66,68,81] However, the energy binding the electron-hole pair is affected by more than the electronic properties of the molecules. Nuclear reorganization occurs after the transfer of electrons which suggests that D/A

blends with strong acceptors have the potential to control polymer microstructures by adding a formal charge to the polymer.
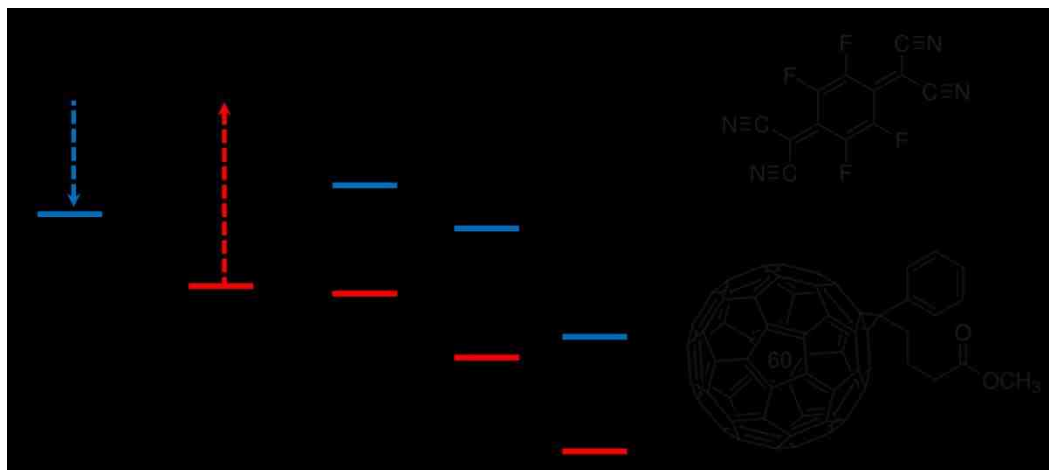
Figure 1.6: Oxidation and reduction potential energy diagram with HOMO and LUMO energy levels of donors and acceptors. Structures: a) F$_4$-TCNQ and b) PCBM.

Formation of the charge separated state (CSS), $D^{*+} + A^{*-}$ is result of integer charger transfer from D to A.[66,68] The formal charge on the polymer chain promotes relaxation of the backbone structure to stabilize the ion by redistributing electron density across the polymer backbone which may also contribute to relaxation of the molecular lattice.[73,76,78,82,83] The non-interacting unpaired electrons give rise to paramagnetic species that have unique spectroscopic markers and can help us to understand the how charge redistribution on the polymer chain changes conformation and packing. These alterations in structure can be identified with infrared, Raman, and nuclear magnetic resonance spectroscopies then optical and electron paramagnetic resonance techniques

17

can be used to track changes in the electronic state of the polymer and acceptor that result from changes in charge density. Controlling integer charge transfer on polymer structures may in turn enable control of polymer packing in D/A blends to help reduce variability of structures that result from solution processing techniques. In Figure 1.7 a schematic represents the ground state interaction of a strong electron acceptor with the donor. Frame A is of the energetically favorable charge transfer D/A interface. Frame B represents the charge transfer complex and frame C shows the charge separated state. The extent of CTC formation in this type of D/A reaction is not clear. The top arrow indicates a potential direct integer charge transfer reaction path that may result from strong acceptors reacting with the polymer.
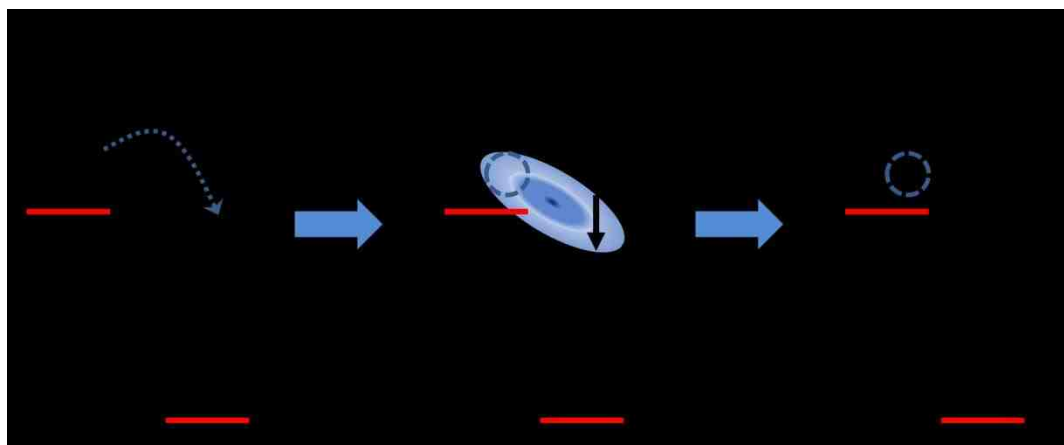
Figure 1.7: Ground state interaction of strong electron acceptor with donor.

In chapter 2 the details of experiments, spectroscopy, and characterization are presented. In chapter 3, nanofibers assembled from P3HT under varying conditions are examined to illustrate the effects of controlling the organization of the polymer before thin film casting in effort to improve the optoelectronic properties. The nanofiber polymer systems represent a new testbed for understanding aggregation without the complicating effects of polydispersity encountered in current conventional P3HT aggregate systems. The assembly procedure gives rise to a highly ordered J-aggregated conformation.

Chapter 4 presents a spectroscopic study of the effects of loading P3HT with the electron acceptor PCBM. Changes in P3HT packing with an increase in PCBM weight fraction led to an increase in relative disorder. These effects were correlated with

19

resonance Raman imaging and in-situ photocurrent images to evaluate effects of structural changes on current output.

Chapter 5 presents an investigation of the role of polymer conformation and aggregation on doping efficiency. F_4-TCNQ, a strong electron acceptor, was mixed with regio-regular (r-Re) and regio-random (r-Ra) P3HT to better understand how aggregates affect ground state charge transfer reaction products. Upon addition of the strong acceptor a charge transfer salt formed in both r-Re and r-Ra P3HT, however the reaction was very limited in r-Ra relative to r-Re P3HT blends.

Chapter 6 presents future directions of this research. A brief review of how donor and acceptor blends can be used to control the bimodal distribution of species in poly[2-methoxy-5-(3′,7′-dimethyloctyloxy)-1,4-phenylenevinylene] (MDMO-PPV) at room temperature. The strong electron acceptor, 2,3-Dichloro-5,6-dicyano-p-benzoquinone (DDQ) was used in blends to look at structural changes in this polymer renowned for its tendency toward amorphous conformations. We show a change in the frequency of the fundamental vibrational mode due to structural changes caused by the formation of charged paramagnetic species on the polymer chain. This was supported with IR and ^{13}C NMR that display structure changes of the DDQ from the quinone to the benzone form as would be expected after reduction.

CHAPTER 2

Instruments and Procedures

Optical absorption spectra were recorded on a UV-Visible spectrophotometer (Shimadzu UV-240IPC) in a scan range from 300 to 900 nm. Solution emission spectra were measured on a Varian Cary Eclipse Fluorimeter with broad-band excitation sources. Infrared spectra were collected on a Thermo Electronic Nicolet 380 FT-IR with a Smart Orbit, 30,000 to 200 cm^{-1} diamond accessory. The 780 nm pre-resonance Raman spectra were recorded with a Thermo Scientific DXR Smart Raman with 180 ° collection and standard low resolution grating. X-band EPR was measured with a Bruker EMX EPR spectrometer with an oxford cryostat mounted in the cavity. An Advance 300 Bruker spectrometer was used to measure NMR chemical shifts in a 300 MHz field. The magnet was equipped with standard 5 mm probe, the signal was locked on deuterated chloroform and standard acquisition parameters were used for ^{19}F, ^{13}C, and ^{1}H. A Bruker Dimension Icon Atomic Force Microscope system was used to collect images of nanofibers prepared from p-xylene, a similar solvent to toluene. The instrument was used in tapping mode and tapping force was carefully controlled to avoid damaging the fibers and pulling fibers off the substrate. Experiments were conducted on home-built microscope spectrometers with confocal and widefield set-ups outfitted with adapters for a cryostat, and a high pressure anvil. Electron multiplying charge coupled device (CCD) cameras and avalanche photo diodes were used to measure emission from samples. Figure 2.1 diagrams a setup for Raman imaging used in chapter four. An Ar-Kr ion laser beam is

directed into the microscope and focused on the sample. Raman scattering from the sample is reflected by a dichroic mirror (DM) through a Raman edge filter (EF) and focused on the CCD camera entrance slits. Photocurrent is recorded using a lock-in amplifier which is synchronized to Raman scattering collection. Further details of the microspectroscopy set-up are described previously.[27,28,49]
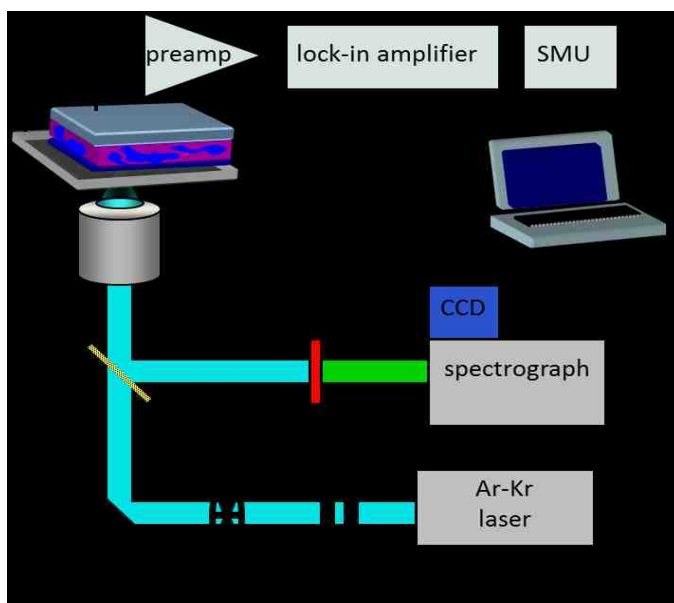
Figure 2.1: The experimental set-up of Raman/photocurrent imaging (Reference 49).

Work was performed under a nitrogen environment. Dissolved materials were filtered using a 0.2 μm filter (Whatman) to remove any undissolved solid before use. Glass substrates and indium-tin oxide ITO coated glass substrates were cleaned by sonication in trichloroethylene, acetone, and methanol for 15 min each. Thin films of polymer and blends were prepared by spin-cast onto clean glass coverslips at 600 rpm.

Thermal annealing treatments were performed by heating samples on a hot plate at 110 °C for 20 minutes.

2.1 Self-Assembled Nanofiber Fabrication

For the assembly of nanofibers poly-3-hexylthiophene (P3HT >95 % regioregularity, 30-60 kDa Plextronics) from Aldrich was dissolved in HPLC grade toluene from Burdick and Jackson and high purity pentane from Omni Solv. 1 : 100 wt/wt P3HT (2 mg) to toluene (200 mg) solutions were sealed and sonicated at 80 °C using a hot water bath resulting in an orange transparent solution with no apparent particulates. The solution was cooled slowly in the water bath at a rate of 20 °C/hr to room temperature. A gradual change in color from orange to purple occurs as nanofibers are formed, as shown in Figure 2.2. The nanofibers were separated from supernatant by centrifuged at 3000 RPM for 30 min below 298 K. The supernatant was removed and the remaining nanofibers were washed with additional amounts of toluene and centrifuged, repeat 2-3 times until the supernatant was optically clear. A Soxhelet extraction was performed to verify if minority synthetic impurities affected nanofiber formation. Spectroscopic studies of nanofibers generated from as-is and purified P3HT showed no difference in response.
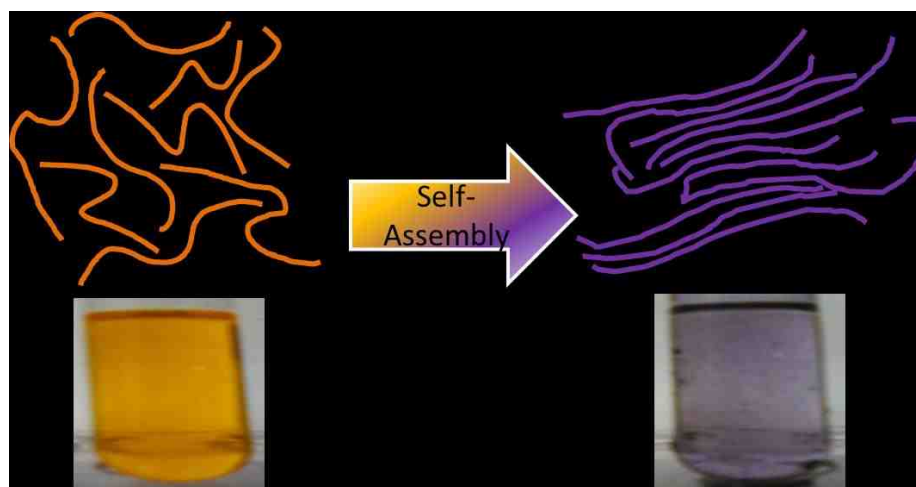
Figure 2.2: P3HT nanofibers made over 24 hours. Yellow solution is P3HT in hot toluene. Colloidal purple solution develops after 24 hours at room temperature.

2.2 P3HT/PCBM Blend Experiments

For the preparation of photovoltaic devices electronic grade, regio-regular poly-(3-hexylthiophene) (MW~87,000 g/mol, Rieke Metals) and [6, 6]-phenyl-C61-butyric acid methyl ester (PCBM, Aldrich), were dissolved in anhydrous chlorobenzene at a concentration of 10 mg/mL and stirred for ~12 hours in a nitrogen. Thin film samples for devices were fabricated on ITO coated slides. A hole transport layer poly(3,4-ethylenedioxythiophene):poly(styrenesulfonate) (PEDOT:PSS, Baytron) was deposited on ITO surfaces by spin casting at 2000 rpm followed by heat curing at 130 ^{o}C for 30 min to remove residual water. P3HT/PCBM thin films were next deposited by spin-casting at 600 rpm for 180 s with 1 : 1, 1 : 2, 1 : 3 and 1 : 4 wt/wt ratios. Aluminum overcoatings were then deposited on the P3HT/PCBM films by thermal vapor deposition using a

shadow mask with ~25 mm^2 squares to define the device active area. Leads were connected to the devices using a silver epoxy paste (Dynaloy); a device shown in Figure 2.3.
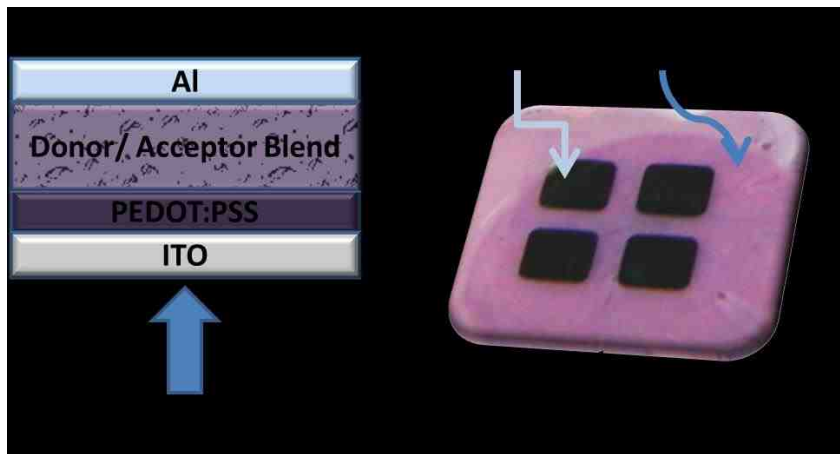
Figure 2.3: Diagram of basic bulk hetrojunction solar cell design and P3HT/PCBM blend device with PEDOT:PSS base on ITO coated glass substrate.

2.3 P3HT/PCBM Blend Characterization

P3HT/PCBM thin films were characterized by absorption and Raman spectroscopy and corrected for wavelength-dependent variations in the detector response. Device EQE and I-V characterization measurements were measured using a homebuilt apparatus described previously.[49] Resonance Raman and photocurrent imaging (RRPI) of P3HT/PCBM solar cells of variable PCBM loadings were performed using a scanning confocal spectrometer system, diagram displayed in Figure 2.1 and was described in detail previously.[3,27] Raman spectra were excited with sinusoidally modulated 488 nm light (20492 cm^{-1}) that excites both aggregated and unaggregated P3HT chains equally

(i.e., similar optical densities). Excitation intensities were kept in the range of ~1 kW/cm^2 and no photodegradation effects were observed on the timescales of spectral acquisition (~100 ms) per scan point. Simultaneous photocurrent measurements are taken for each scan point using a lock-in technique that samples the AC component, and values are stored in a computer and plotted. Excitation power dependent photocurrent measurements were performed to verify response linearity and that deviations from higher order effects such as exciton-exciton annihilation were minimal within the excitation intensity range used, which is shown in Figure 2.4 on the right along with survey optical and AFM images that were measured to help guide the selection of image scan range for each wt/wt loading.
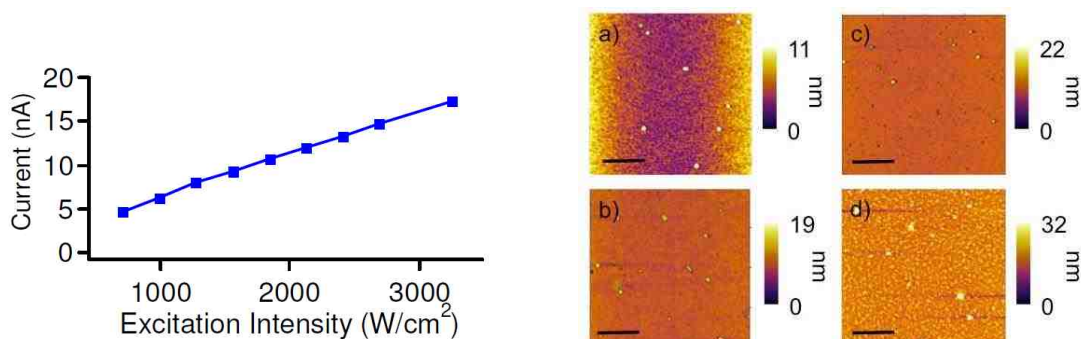
Figure 2.4: Left: Excitation intensity dependent photocurrent response generated from a 1 : 1 wt/wt P3HT/PCBM device illuminated in a widefield mode. Right: Survey AFM micrographs of a) 1 : 1, b) 1 : 2, c) 1 : 3, and d) 1 : 4 annealed P3HT/PCBM thin films (scale bars =5 μm).

2.4 P3HT/ F_4-TCNQ Experiments

Electronic grade, regioregular P3HT (Mn ~50000 g/mol), regiorandom P3HT (Mn ~50000 g/mol) and 2,3,5,6-tetrafluoro-7,7,8,8-tetracyanoquinodimethane (F_4-TCNQ) were purchased from Rieke metals, and Aldrich and used without further purification. Materials were dissolved in chlorobenzene (CB) at a concentration of 10 mg/mL (P3HT), and 1 mg/mL (F_4-TCNQ) for ~12 h. Solutions were mixed with wt/wt with equal volumes aliquots. Absorption and 780 nm Raman spectra were obtained from freshly made blend solution in 100 μm (~65 μl) cuvettes.

X-band EPR spectra of r-Re and r-Ra P3HT solutions doped with F_4-TCNQ were measured in the dark at 298 K for loading up to 50% wt/wt. Polymer samples had similar molecular weights and were prepared with the same final concentration (5 mg/mL). Each

27

EPR spectra represent the average of 4 scans. To avoid reabsorption effects samples were prepared in 1.5 mm capillary tubes with sample height of about 30 mm. then were placed in 4 mm EPR tubes for measurements. Conditions were as follows: 1 G field modulation (100 kHz), receiver gain =6320, time constant =81.92 ms, conversion time =20.48 ms; v =9.61396 ± 0.00519 GHz (2.1 mW).

NMR measurements were performed on pristine and blend solutions in deuterated chloroform (CDCl3) 99.8% chloroform-d –Aldrich, for ^{19}F NMR measurements, kept F_4-TCNQ concentration constant at 1 mg/ml with variable P3HT loadings. The chemical shift was set with external standard, hexafluorobenzene (HFB) and a standard fluorine parameter set was used, signal was locked on $CDCl_3$ and spectra were an average of 64 scans. The spectra were corrected for fluorine background signal from the probe by subtracting free induction decays prior to Fourier transform.

2.5 MDMO-PPV/DDQ Experiments

Poly[2-methoxy-5-(3′,7′-dimethyloctyloxy)-1,4-phenylenevinylene]   (MDMO-PPV), was obtained from American Dye Source (ADS), and mixed with 2,3-Dichloro-5,6-dicyano-1,4-benzoquinone (DDQ) at 5 mg/ml. Absorption, luminescence, and 780 nm Raman spectra were obtained from freshly made blend solution in 100 um (~65 µl) cuvettes. Neat and blend thin films samples were cast from fresh solutions drop cast on $25x25$ mm cover glass. MDMO-PPV was dissolved in chlorobenzene and DDQ was dissolved in THF at 10 mg/ml. MDMO-PPV solutions were mixed with equal volumes of DDQ solutions of different molarities with MDMO-PPV concentration fixed at 5

mg/ml with variable DDQ loadings. Upon mixing of DDQ with MDMO a spontaneous color change was observed in blends as small as 0.1 : 1.

The attenuated total reflectance Fourier transform infrared spectra were obtained from thin films samples removed from substrate and were placed directly on the diamond cell. Same EPR procedures as used above with $v = 9.61661 \pm 0.0026$ GHz (2.1 mW) from 4 to 150 K. For variable low temperature measurements samples were placed in a continuous flow cryostat (Oxford) and evacuated to a base pressure of $\sim 10^{-6}$ mbar. LHe was used as the cryogen and temperature was maintained at ~ 4 K for one hour before measurements using the cryostat thermo-couple controller. The temperature was stabilized for thirty minutes in-between measurements at increased temperatures.

CHAPTER 3

J-Aggregate Behavior in Poly-3-hexylthiophene Nanofibers

(This chapter is based on the previously published article, Journal of Physical Chemistry

Letters, 2012, 3, 259-263.)

3.1 Introduction

Solution-processed thin films of conjugated polymers have demonstrated

considerable promise as active systems for a variety of optoelectronic applications, such

as solar cells and field-effect transistors.   However, reliable control of material

performance in these functional forms has remained difficult owing to the random nature

of molecular conformations, packing, and morphology.   The archetype conjugated

polymer, poly-3-hexylthiophene (P3HT), is one of the few systems that forms quasi-

crystalline domains (aggregates) in thin films. P3HT aggregates are composed of $\pi-\pi$

stacked chains ~3.8 Å apart that are typically 10−30 nm in length,[6,84] but polydispersity

effects modulate the size and order of the aggregate, and interpenetrating amorphous

chains (i.e., P3HT chains of lower regioregularity or, random coils) cause stacking faults

within the aggregate.

Importantly, the structural attributes of aggregated polymer chains have a

significant impact on their electronic properties, which are exposed by optical

spectroscopy.   For example, the face-to-face stacking of P3HT chains in aggregates

usually favors interchain exciton coupling[85] leading to optical lineshapes resembling H-aggregates where, for example, the electronic origin (0−0) transition of the emission spectrum is attenuated because of its forbidden nature.[86] This particular mode of exciton coupling dominates in P3HT thin films owing to the presence of amorphous chains that reduce the overall intrachain order (planarity) and conjugation lengths in the aggregate.[44] However, self-assembly of aggregated P3HT nanostructures offers an attractive means to control both intra- and interchain order by selectively excluding amorphous chains from the aggregate. These techniques can, in principle, overcome the limitations of conventional thin film processing owing to fractionation effects that select a narrow molecular weight distribution of the polymer sample thus lowering effective polydispersity and increasing aggregate crystallinity. Moreover, this approach offers greater potential to tune electronic coupling characteristics beyond what is possible in films. In the following, we show that nanofibers (NFs) of P3HT self-assembled in toluene exhibit pronounced intra-chain exciton coupling, leading to photophysical behavior of J-aggregates (i.e., the 0−0 transition is enhanced relative to the 0−1 sideband).[87,88] This behavior results from an increase in intrachain order of P3HT chains within the aggregate, and the associated increase in intrachain coupling dominates over the interchain (H-aggregate type) exciton coupling. Temperature- and pressure-dependent spectroscopic studies highlight the delicate interplay between intrachain order and interchain coupling that may potentially be exploited to control selectively exciton coupling in polymer nanostructures.

3.2 Results and Analysis

P3HT nanofibers were characterized primarily by UV/vis absorption, emission and Raman spectroscopy. Absorption spectra were recorded in the range of ~400-800 nm. Optical densities of nanofiber dispersions were typically in the range of 0.15-1. Raman spectra were obtained using a scanning confocal microscope described in detail previously.[87] Excitation colors were selected on resonance with the π-π* absorption of P3HT (~450-600 nm) although large fluorescence backgrounds made it difficult to obtain spectra with excitation wavelengths $>$~520 nm. Single particle emission spectra and imaging, emission life times, and high pressure anvil measurements were all obtained using the same microscope system. Because amorphous chains in the supernatant can complicate emission lineshapes, excitation wavelengths were selected to excite only the nanofibers (568 nm). Samples were raster scanned over a diffraction limited laser spot to obtain images using a single photon counting diode as detection. Spectra were then measured by positioning the sample over the laser spot and directing the emitted light into a CCD/spectrograph. Polarized emission spectra and dichroic ratios were measured by placing a half-wave plate mounted on a motorized rotation stage after the microscope exit port which was computer controlled. A polarization scrambler was then placed before the entrance slit of the spectrograph to avoid distortions from the grating.

For single particle spectroscopy, Emission lifetimes and hydrostatic pressure studies, nanofibers were dispersed in 3% wt/wt polystyrene : toluene and either drop- or spin-casted onto rigorously cleaned glass substrates. To avoid dissolution of nanofibers, a small amount of pentane was added to dispersions which is a non-solvent for P3HT.

P3HT nanofibers were then dispersed in very low concentration in polystyrene host matrices with O.D. <0.15.

Emission lifetimes of single NF were measured on dilute nanofibers using time-correlated single photon counting techniques (TCSPC). Sample excitation was achieved using a pulsed laser diode (Edinburgh) with a nominal wavelength of 445 nm. Emission was filtered using a 580 nm edge filter to avoid possible contributions from surrounding amorphous chains. An instrument response function (IRF) was recorded using scattered excitation light. Emission decay profiles were found to be independent of power densities ($\sim 10 - 100$ W/cm^2).

For variable pressure spectroscopy measurements nanofiber dispersions were placed in a diamond anvil cell (Diacell μscope DAC-HT(G)) and pressure was applied using a gas membrane. A long working distance objective (Zeiss plan-fluar, 40×, NA=0.6) was used to 3 focus excitation light into the cell. Pressure was calibrated using the ruby standard and either Nujol or water:methanol (1 : 4 v/v) was used as the pressure-transmitting medium.

Low temperature emission spectra were recorded using a home-built wide-field imaging microscope equipped with a LN$_2$ cooled, deep-depleted CCD camera/spectrograph (Horiba-Jobin Yvon iHR 320). Dilute thin film samples were placed in a continuous flow cryostat (Oxford) and evacuated to a base pressure of $\sim 10^{-6}$ mbar. LN$_2$ was used as the cryogen and temperature was maintained at ~ 77 K using the cryostat thermo-couple and controller. Laser edge filters (Semrock) were used to remove scattered excitation light and spectra were corrected using a tungsten lamp source.
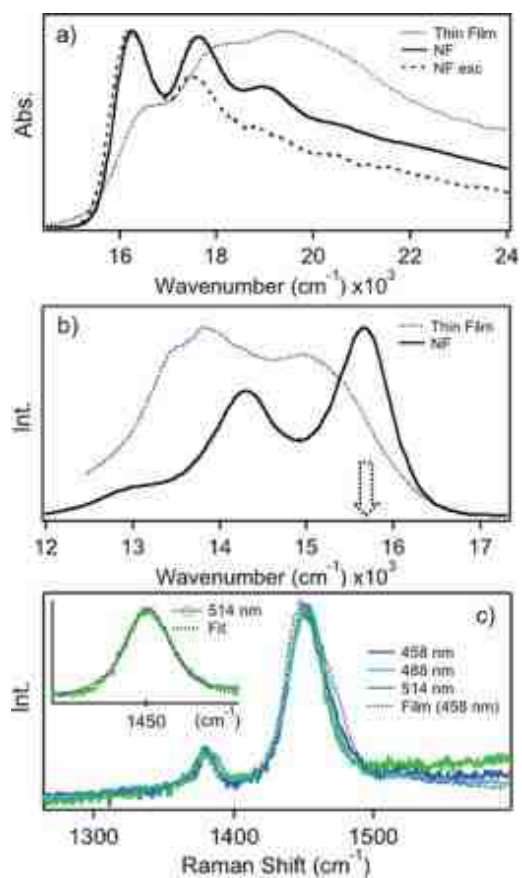
Figure 3.1: (a) Absorption spectra of P3HT thin films (blue dotted trace) and dilute NF suspensions (black solid trace). A dilute NF excitation spectrum (black dotted trace) is included for comparison. (b) Emission spectra of P3HT thin films (blue dotted trace) and dilute NF suspensions (black solid trace). The downward arrow indicates the emission energy used to measure the excitation spectrum in panel a, ~ 15800 cm^{-1}. (c) Excitation color-dependent Raman spectra of P3HT NF (solid traces) and film (dotted trace). Inset: Lorentzian fit of P3HT NF Raman line shape.

Figure 3.1a shows absorption aand fluorescence emission spectra of P3HT thin films and dilute P3HT NF solution dispersions (O.D. ~0.05). Inspection of the NF absorption line shape reveals $0-0/0-1$ oscillator strength ratios slightly larger than 1. P3HT spin-cast thin films typically show $0-0/0-1$ ratios less than 1.0 (~0.5 to 0.8), which is indicative of significant interchain coupling leading to H-aggregate character.[44,85] NF emission lineshapes also show enhanced $0-0/0-1$ ratios (> 2), a clear indication of J-aggregation in these systems,[86-88] compared with thin film emission lineshapes, that possess attenuated 0−0 transitions as expected for H-aggregates. The significantly reduced Stokes shift in NFs compared with films (~500 vs. ~1600 cm^{-1}, respectively) is further evidence of dominant J-like behavior.

Optical spectra were measured to assess the degree of aggregation in NF's. Excitation and emission spectra of dilute nanofibers (O.D. $<$ 0.1) are shown in Figure 3.2. Excitation spectra from P3HT NF bear resemblance to previously reported absorption spectra of highly regioregular P3HT films, which also show a dominant $0-0$ transition.[48] These effects are suppressed by diluting nanofiber suspensions with toluene:pentane mixture. Excitation and emission spectra of dilute nanofibers (O.D. $<$ (0.1) are shown in Figure 3.2. Emission spectra were generated at two different excitation wavelengths and excitation spectra were recorded at two different energies across the emission band.
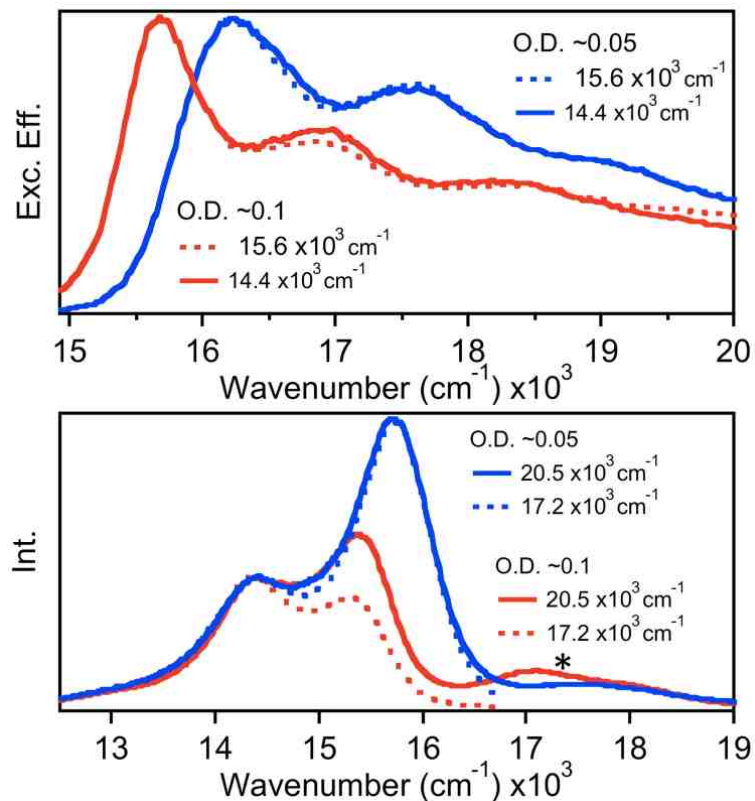
Figure 3.2: Excitation efficiency (top panel) and emission intensity (bottom panel) for two concentrations of nanofibers. Excitation spectra are generated for two emission energies. Emission spectra are excited at two excitation energies that excite only the nanofiber and nanofiber/supernatant. * denotes contributions from amorphous chains in the supernatant.

Inspection of emission lineshapes reveals that re-absorption of the $0 - 0$ transition at higher concentration (O.D.) leads to significant lineshape distortions. This effect leads to apparent irregular vibronic progression intervals, red-shifted bands and large $0 - 0/0 - 1$ ratios which is merely an artifact from self-absorption. However, by

diluting NF suspensions, excitation spectra overlap well with absorption spectra. We found that diluting to O.D. < 0.1 are necessary to completely suppress lineshape distortions due to self-absorption. Although this characteristic was not directly attributed to J-aggregation, comparisons were made to single polydiacetylene (PDA) chains that exhibit pronounced J-like signatures.[87,89]
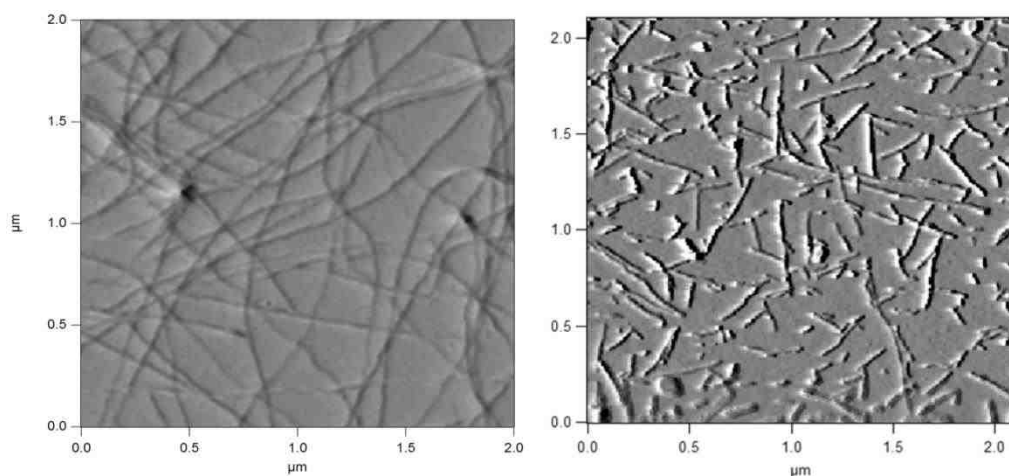
Figure 3.3: Left: AFM micrograph of concentrated nanofibers. Right: dilute nanofibers.

Dilution can also affect the NF structure by partially dissolving the fiber. To further understand how dilution affects nanofiber structure, AFM images were measured for both concentrated and dilute samples. Figure 3.3 shows micrographs of concentrated and dilute nanofibers dispersed on glass by spin-coating. Nanofibers show distinctly smaller aspect ratios upon dilution which is likely due to dissolution. However, this can be mitigated by adding a non-solvent, i.e. pentane, which arrests dissolution and preserves the characteristics of the NF structure.
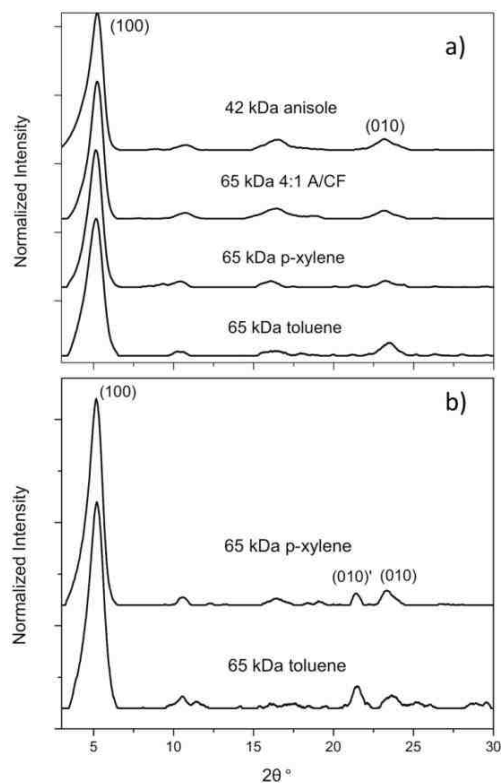
Figure 3.4: a) Powder X-ray diffraction studies of P3HT NF prepared from different solvents. b) Comparison of re-heated toluene and p-xylene NF exhibiting a new packing feature (010)'.

To better understand the structural origins of the anomalous J-aggregate character in P3HT NF assembled from toluene, powder X-ray crystallography studies were performed on samples prepared from different solvents. Figure 3.4 shows powder patterns from nanofibers prepared from anisole, anisole/chloroform, p-xylene, and toluene. Clearly, each type of nanofiber exhibits similar packing of P3HT chains albeit, toluene fibers show higher order. Importantly, toluene appears to direct the high MW

fraction to pack into fibril structures leaving the lower MW fraction in the supernatant. This fractionation effect is crucial for the formation of highly ordered π-π stacks with very few stacking faults, unlike aggregates in spin-cast thin films. Figure 3.5 illustrates a diagram to describe the packing in fiber formation.
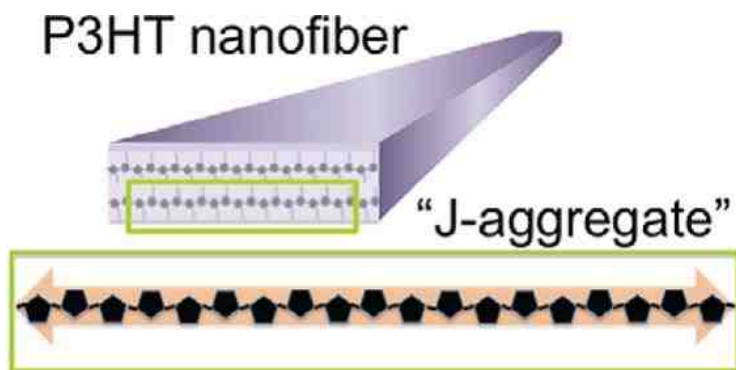
Figure 3.5: Diagram to describe the proposed packing of J-aggregates in nanofibers.

We now use resonance Raman spectroscopy to help resolve how P3HT chain conformation, packing, and order within NF structures differ from aggregates in films. P3HT aggregates can consist of planar, crystalline stacks of chains, amorphous chains (i.e., random coil conformations), or a combination of both. The presence of amorphous chains leads to stacking faults that reduce intra- and inter-chain order. Typical spectroscopic signatures of amorphous P3HT chains are broadened and blue-shifted absorption[44,48] and Raman[27,90] transitions with respect to planar chains. Excitation color dependent NF Raman spectra were measured in the C=C backbone symmetric stretch region (~1450 cm^{-1}), which is a good reporter of the P3HT aggregation state.[27,90] Excitation colors used were >19000 cm^{-1} to avoid large emission backgrounds closer to

the NF $0 - 0$ transition. Virtually no dispersion and only minor changes in linewidths (<2 cm^{-1}) were observed in the $\sim$1450 cm^{-1} mode over the excitation energy range. Linewidths are also relatively narrow ($\sim$16 cm^{-1}) with no discernible contributions from amorphous chains (ca. 1470 cm^{-1}).[27,90] We conclude that NF π-stacks are largely free of amorphous chains and that any high-energy absorption features result from amorphous (i.e., dangling or looping) chains located outside of the aggregated region of the NF that are not capable of $\pi-\pi$ stacking. Zhang et al. also showed that the sizes of amorphous regions are dependent on polydispersity and molecular weight, both of which play an important role in determining the order–disorder boundary of these systems.[17]

The trends outlined thus far are consistent with dominant J-aggregate, or head-to-tail, type coupling between thiophene repeat units within the single P3HT chains comprising the NF structures.[87,88] This behavior originates from the high intrachain order (planarity) within the NF aggregates that supports strong intrachain coupling and, in turn, dominates over interchain exciton coupling.

Previous spectroscopic studies on poly-(3-(2′- methoxy-5′-octylphenyl)thiophene) (POMeOPT) in poor solvents (i.e., toluene) have shown similar spectral properties as the NFs reported here (see Figure 3.1a) and were attributed to crystallite formation.[91] It is noteworthy, however, that interchain spacings in POMeOPT crystallites are $\sim$7 Å compared with $\sim$3.8 Å in P3HT aggregates. Furthermore, studies of dispersed oligo-thiophenes containing up to 16 repeat units have shown similar spectral features to our NF's albeit smaller $0 - 0/0 - 1$ ratios in emission spectra.[92] Comparison with emission spectra of isolated PDA chains, which behave as strongly coupled J-aggregates

$(0 - 0/0 - 1 = 60$, T =13K), also demonstrates that intrachain coupling is smaller in P3HT NF's.[92]
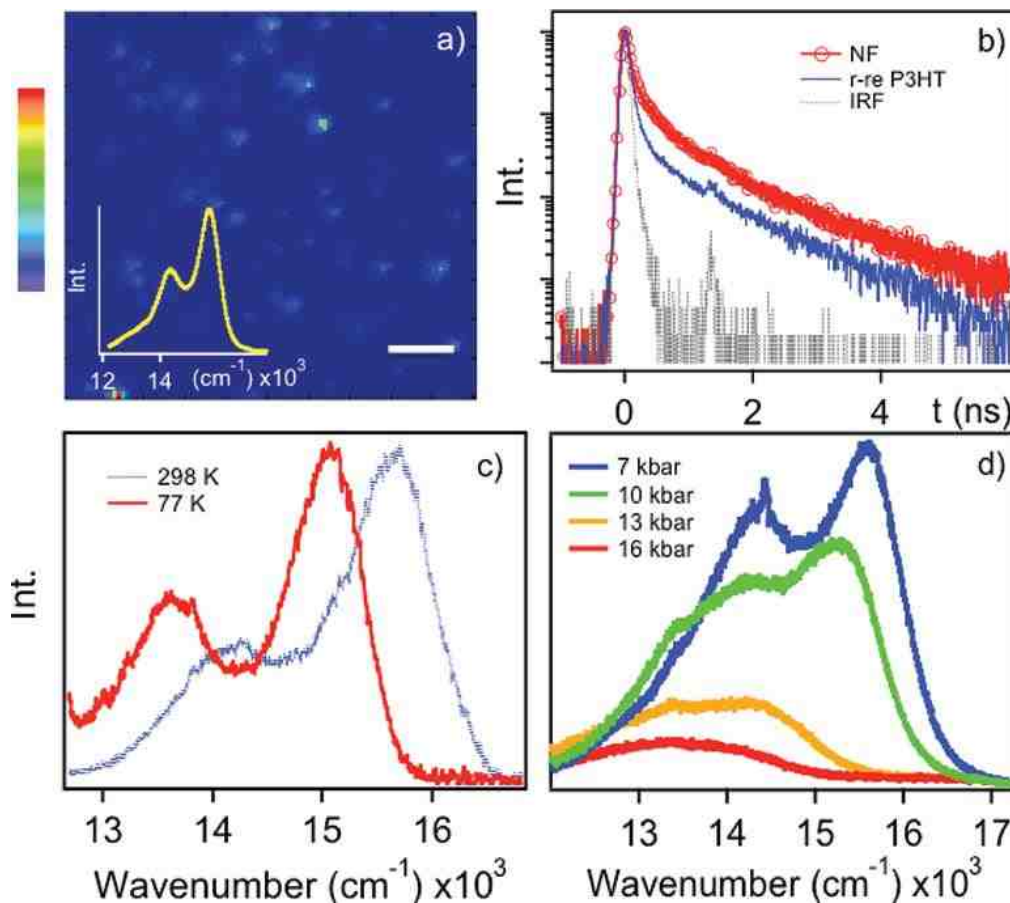
Figure 3.6: (a) Single-particle emission image of P3HT NF dispersed in polystyrene (λ_{exc} =568 nm). Inset: ensemble average spectrum of 35 particles. Scale bar =1 μm. (b) Ensemble emission decays generated from ~25 NF particles (red) and annealed regioregular P3HT thin films (blue). (c) Emission spectra of P3HT NF at 298 (blue) and 77 K (red). (d) Pressure-dependent emission spectra of dilute P3HT NF dispersed in a polystyrene host matrix.

To avoid possible spectral line shape distortions from agglomeration effects in solution, we dispersed P3HT NFs in a polystyrene matrix and studied them by single particle emission spectroscopy techniques. Figure 3.6a shows a representative emission image (298 K) of well-dispersed, diffraction-limited spots corresponding to individual P3HT NFs as well as an ensemble average spectrum composed of over 35 single particles. To verify that the dispersion did not adversely affect the fiber structure emission spectra from single particle averages were compared with concentrated and dilute NF dispersions (see Figure 3.7).
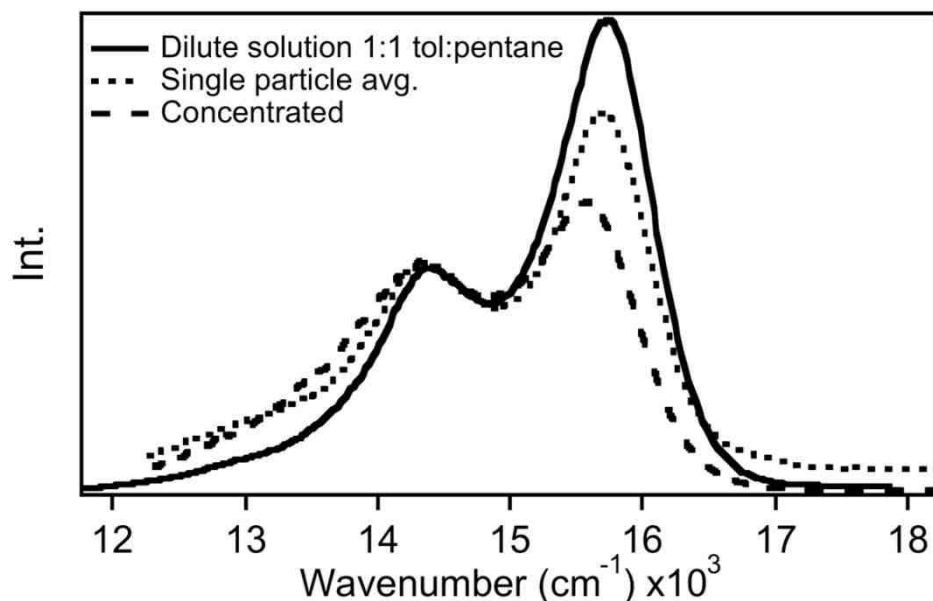
Figure 3.7: P3HT nanofiber emission spectra from, dilute (O.D. ~0.02) solution dispersions (solid), single particle ensemble average (dotted) and concentrated (O.D. ~0.1) dispersions (dashed).

Single particle emission spectra and transients were generated using 568 nm (17605 cm^{-1}) light that preferentially excites the NF. Very little heterogeneity is observed in single NF spectra, which closely resemble those obtained from dilute toluene solutions (Figure 3.1a). To verify that spots in Figure 3.2a were nanofibers and not single molecules, Figure 3.8 displays representative integrated intensity transients that show only small, gradual decreases due to photodegradation effects. The single NF particles display no fluorescence intermittency within the excitation intensity range used ~10−100 W/cm^2. On the other hand, single molecules were expected to show rapid

photobleaching as well as flickering (intermittency) due to photochemical processes demonstrating that the spots in Figure 3.6a are in fact individual NF's rather than single molecules.
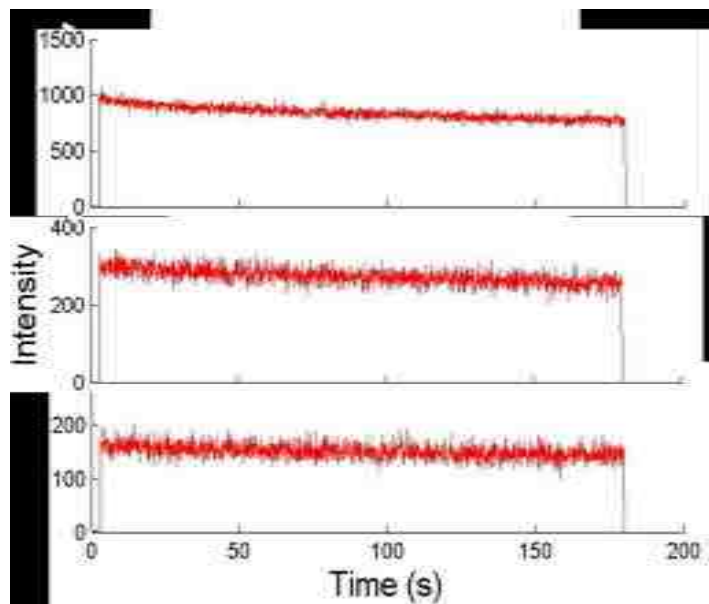
Figure 3.8: Representative fluorescence emission transients from single P3HT NF.

Polarized emission spectra of single nanofibers were recorded to determine if the non-Poissonian lineshapes observed were the result of multiple emission origins. In Figure 3.9 polarized emission spectra of single NF's display only small dichroic effects (<2) and no change in vibronic $0 - 0/0 - 1$ intensity ratio indicating that these lineshapes originate from a single emitting species.
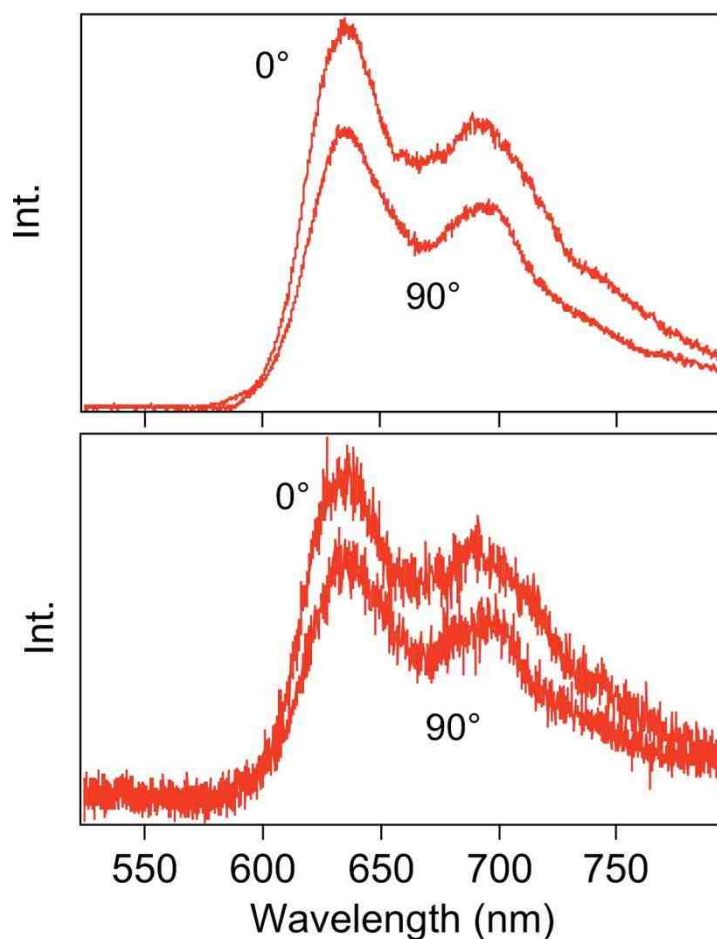
Figure 3.9: Representative polarized emission spectra of single P3HT nanofibers.

Emission lifetimes of single NF particles were recorded using time-correlated single photon counting techniques. In Figure 3.6b an ensemble averaged decay trace generated from ∼25 particles in shown. NF samples exhibit non-exponential behavior with fast, instrument-limited and slow components. The decay profiles were well-described using a fast, instrument-limited (∼50 ps) component (∼54%) and a slow component with a time constant of ∼840 ps (46%). This behavior is likely due to the

close packed nature of the P3HT chains in the aggregate. For comparison, an averaged emission decay profile from an annealed r-Re P3HT film is included that shows a larger fast component (~78%) and a smaller slow component time constant of ~780 ps (~22%). The fast component contributions were independent of excitation intensity for both samples. Previous work on P3HT films dispersed in poly-ethylene matrices has shown that fast torsional relaxation on the ~10 ps timescale occurs in aggregated P3HT, suggesting that interchain torsional relaxation could be responsible for this feature.[53] Exciton annihilation processes was ruled out since this contribution was not dependent on excitation intensity. Furthermore, emission was filtered using a 580 nm longpass filter which also rules out stray excitation light as the source of the instrument-limited component. To test this hypothesis, emission lifetimes were recorded from annealed r-Re and r-Ra P3HT thin films. In the decay traces from these two samples where there a larger (~77% vs. ~24%) contribution from the fast component in the annealed regio-regular films. This feature was found to be independent of excitation intensity as well as either point or widefield excitation. The larger value of the slow component decay time constant in NF samples contradicts our expectations of shorter lifetimes in J-aggregates due to a larger radiative rate constant. However, similar increases in the overall lifetimes were observed in the J-like POMeOPT aggregates. Here the lifetime increase arises from a substantial decrease in the nonradiative rate constant, which masks an increase in the radiative decay rate characteristic of J-aggregates.[91] These trends are consistent with greater chain rigidity and smaller interchain torsional displacements following excitation that should likewise lead to diminished nonradiative rate constants in NFs.

Previous studies of single-chain polydiacetylenes have shown marked increases in the emission $0-0$ transition strength at low temperatures due to increased exciton coherence lengths.[88,89] Low-temperature (77 K) emission spectra of dilute NF samples were measured to determine if similar increases in coherence lengths are possible in NFs. Figure 3.6c shows emission spectra of dilute NF samples at 298 (blue) and 77 K (red). At 77 K, the emission maximum red shifts by ~600 cm^{-1}, and $0-0/0-1$ ratios are slightly smaller than those measured at 298 K (~1.5 vs ~2.5, respectively). The substantial red shifts of the NF line shape at 77 K probably result from low-energy traps, whereas the decrease in $0-0/0-1$ ratio at 77 K is unexpected for a pure J-aggregate and indicates the presence of interchain coupling.

To better understand how changes in NF chain packing affect J-aggregate behavior, we applied hydrostatic pressures to NF samples dispersed in polystyrene, and spectra are shown in Figure 3.6d (λ_{exc} =568 nm). Importantly, the pressure dependent emission line shape shows a loss of intrachain order (J-aggregate character), as seen from decreasing $0-0/0-1$ ratios, increasing linewidths, and a monotonic red shift of ~200 cm^{-1}/kbar. These trends suggest that interchain coupling, sample inhomogeneity, and the amount of low-energy traps all increase with pressure. There are two plausible explanations for the pressure-dependent changes in emission lineshapes: (i) distortions in the alkyl side groups (i.e., change from Type I, end-on, to a Type II, interdigitated, or Type 1′, partially interdigitated, structure[6,84]) lead to torsional defects that reduce intrachain order or (ii) an increase in interchain exciton bandwidth (W) due to shorter interchain packing distances. The higher energy interdigitated forms of P3HT aggregates

could likely be stabilized by pressure, and the closer proximity of side groups may result in deviations from a planar backbone conformation. Previous pressure-dependent spectroscopy studies of P3HT films have shown that whereas chains become more planar, changes in interchain coupling are small at higher pressures.[93] However, P3HT chains in NF π-stacks are already highly planar (unlike aggregates in thin films), and only decreases in interchain packing distances in the $\pi-\pi$ stacks are expected. This situation should favor increases in W, albeit small, that likewise increase exciton mobility, thereby allowing the exciton to sample a larger area of the aggregate before decaying radiatively. As a result, both H-type lineshapes and red shifts should occur because excitons have a higher probability of finding emissive traps within their lifetime. Although we presently cannot exclude either mechanism, no abrupt changes in spectra occurred over the pressure range studied (i.e., no clear evidence of phase transitions), making (i) a less likely possibility.

P3HT NF J-aggregates fall within the weak exciton coupling regime, as seen from the size of the emission $0-0/0-1$ ratios.[86-88] Figure 3.10 shows simulated P3HT NF absorption lineshapes using a multiparticle aggregate model that includes both intra- and interchain coupling (J_0).[87,88]

3.3 Theoretical Modeling

The model is based on a trimer of $\pi-\pi$ stacked polymer chains consisting of 20 thiophene units per chain. Details were discussed in appendix 1. The effective or, mean, intrachain electron$-$hole transfer integral (t) connecting neighboring thiophene units is

fixed at 0.18 eV, several times smaller than that used to simulate single PDA chains[88] to account for intrachain disorder in the NF structure. Holding t and the unit-cell Huang−Rhys factor $(1.6)^{94}$ fixed, J_0 is varied to simulate the conformation- and packing-dependent interplay between intra- and interchain coupling in NF aggregates. With J_0 set to zero, spectra exhibit pronounced J-aggregate character with dominant 0-0 transitions in both absorption and emission spectra. The J-like behavior gradually gives way to H-like behavior with increasing J_0. When $J_0 = 400 \text{ cm}^{-1}$, simulated spectra agree well with the experimental P3HT thin film spectra.[44,85] In this limit, the H-aggregate model of reference 83 works well in describing the photophysics.
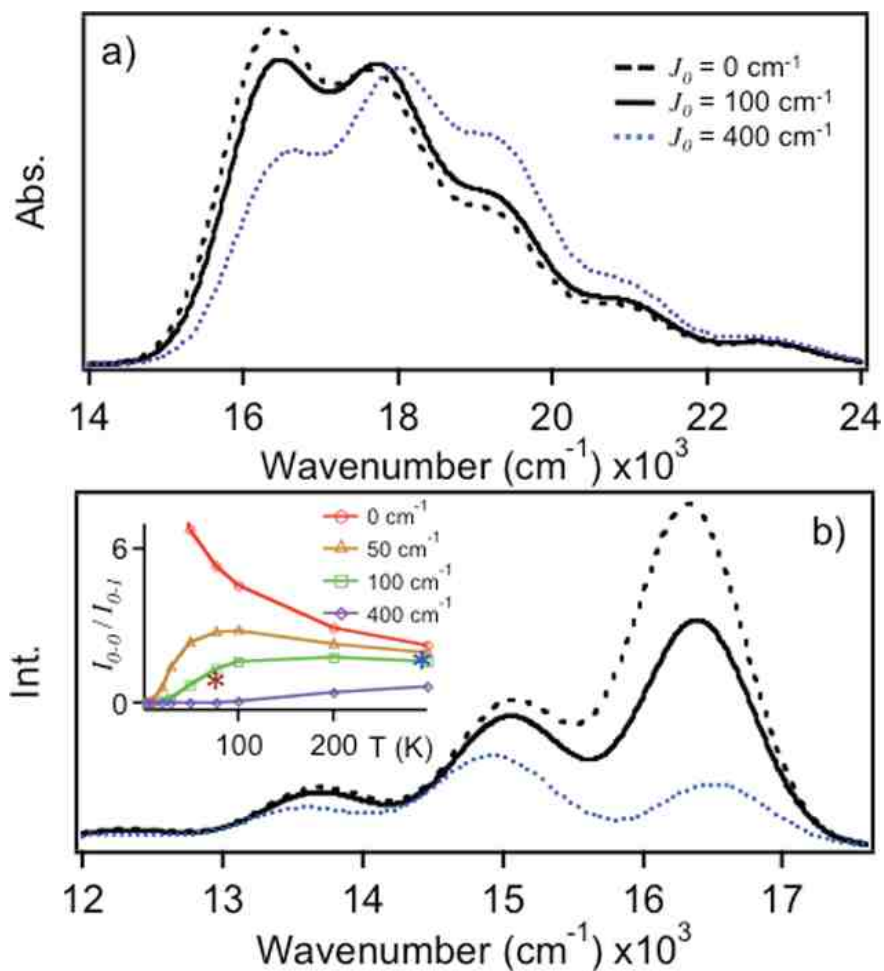
Figure 3.10: Simulated absorption (a) and emission (b) spectra with varying interchain coupling (J_0) at 298 K. Inset: simulated $0-0/0-1$ emission intensity ratios for varying J_0. Asterisks denote the experimental $0-0/0-1$ ratios for P3HT NF's at 298 K (blue) and 77 K (red).

The spectra in Figure 3.10 were calculated by first numerically determining all eigenstates and energies of the Hamiltonian in Equation A.1, and then constructing the absorption and emission spectra as described in earlier papers, for example, see

Reference 83. The effects of increasing temperature in the PL spectra were included by assuming a Boltzmann distribution of emitting excitons.

When disorder is included the 0-0 intensity is no longer zero at T= 0 K because symmetry is destroyed. Hence, in P3HT films at low temperatures (<20 K)[44] the 0-0 intensity is higher than that predicted by the present model which we interpret as evidence for disorder in the films. However, we find that at higher temperatures the neglect of disorder becomes an increasingly better approximation, until at room temperature disorder hardly makes a difference on the PL spectral line shape.[88] Such effects will be discussed at length in a future publication.

Comparison of simulated and experimental spectra suggest that interchain coupling in NF π-stacks lies between $50-100$ cm^{-1}. This small value of J_0 results from the increased intrachain order (conjugation lengths) present in NFs. It has previously been shown that the interchain excitonic coupling (J_0) within a dimer of cofacially aligned oligomers decreases with oligomer length L once L surpasses the intermolecular separation.[95-97] In the polymer limit, we therefore expect negligible excitonic coupling. However, as disorder within the $\pi-\pi$ stacked chains increases, the conjugation length shrinks, and interchain coupling again becomes dominant.[86] Importantly, the simulations accurately predict that a single polymer can display both J- and H-aggregate behavior depending on the relative magnitude of intra- and interchain coupling, which, in turn, strongly depends on the levels of intra- versus inter-chain disorder.

It is also interesting to note that the model predicts virtually no change in the $0-0/0-1$ intensity ratios at 77 versus 298 K for $J_0 = 50 - 100$ cm^{-1}. This result is

contrary to pure, single chain J-aggregates $(J_0 = 0)$, where this ratio is expected to increase with $1/\sqrt{T}$.[87,88] From Figure 3.6c, dilute NF emission $0 - 0/0 - 1$ ratios showed a small decrease at 77 K, which is in good agreement with the simulated ratios for values of $J_0 < 100$ cm^{-1} (Figure 3.10b inset). Furthermore, these simulations demonstrate that P3HT aggregates with nonzero J_0 values undergo an H- to J-like transition with increasing temperature (i.e., the $0 - 0/0 - 1$ ratios at first increase with T, as in H-aggregates, and then decrease with T, as in J-aggregates).
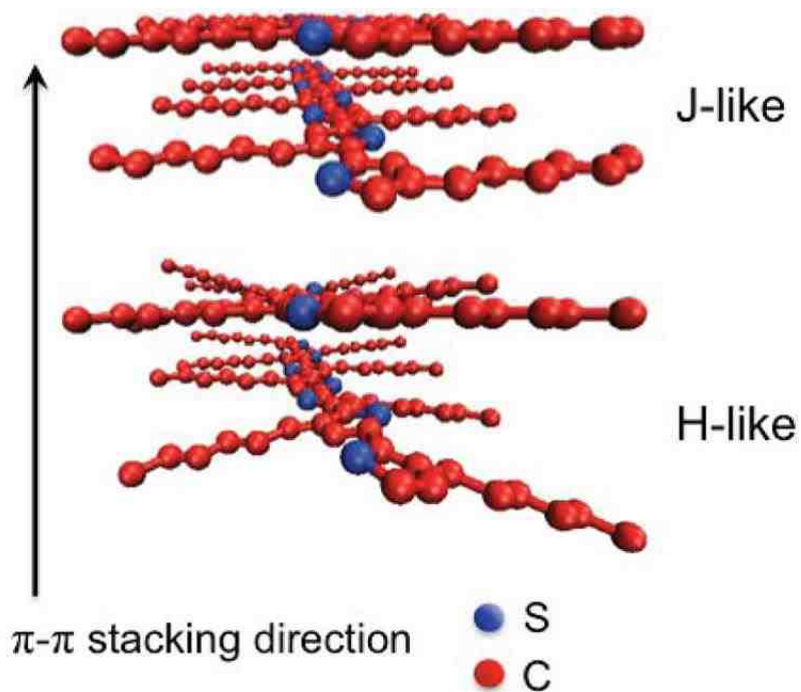
Figure 3.11: Proposed Conformations of P3HT Chains within J-Like and H-Like Aggregates (Hydrogen atoms are omitted for clarity.)

3.4 Conclusion

In summary, P3HT NTs self-assembled in toluene solutions exhibit J-aggregate character in the weak exciton coupling regime. The appearance of J-aggregate behavior in P3HT systems is surprising considering that chain packing characteristics in NF structures (i.e., packing distances, see appendix 1 and reference [54]) are similar to thin films, where H-aggregate behavior prevails. The distinguishing feature of the P3HT NF aggregate is that the self-assembly process selects only the high-molecular weight (MW) fraction, whereas the lower MW (amorphous) fraction remains in the supernatant.[54] This high degree of fractionation results in very few stacking faults within the NF $\pi-\pi$ stacks, due to lower polydispersity, thus promoting long-range intrachain order. Figure 3.11 illustrates this proposed intrachain ordering within P3HT chains for both J-like and H-like aggregates. In the latter, the dihedral angle is expected to deviate significantly about 180°, thus lowering intrachain order and allowing interchain effects to again dominate.

It is also noteworthy that J-type features emerge only when NFs are well-dispersed (i.e., no NF-NF contacts). For example, previous studies of close-packed P3HT NF films grown from slow solvent evaporation exhibit H-type character due to dangling chains on the periphery of the fiber (i.e., amorphous region) that interact with those of neighboring fibers and perturb intrachain order.[17] Because the sizes of these amorphous regions are molecular-weight-dependent,[17] we are presently pursuing studies of P3HT NF fabricated from a range of molecular weights to better understand the order−disorder boundary of the NF structure and its influence on the exciton coupling. Overall, NF assemblies demonstrate that selective control of exciton couplings is possible

and could potentially be exploited to achieve long-range charge and energy transport in new nanoscale polymer functional forms.

CHAPTER 4

Understanding Morphology-Dependent Polymer Aggregation Properties and Photocurrent Generation in Polythiophene/fullerene Solar Cells of Variable Composition

(This chapter is based on the previously published article, Journal of Physical Chemistry C, 2010, 114, 15121-28)

4.1 Introduction

The ability of conjugated polymer molecules to form extended networks of co-facial, π-π stacked chains in thin films is vital for achieving optimal performance in optoelectronic device settings.[41,98-100] In particular, these structures (herein referred to as aggregates) have modified electronic structures that have important implications on charge and energy transfer processes.[101-103] Although the establishment of aggregated polymer networks underlies the performance of all polymeric optoelectronic devices, it is especially important in solar cells due to the need to add substantial amounts of electron acceptor materials (i.e. fullerene derivatives) to polymers that can effectively break up these extended networks. This effect can be partially alleviated by post-processing annealing treatments that permit the fine-tuning of polymer/fullerene morphologies (i.e., phase domain size and composition) and polymer aggregation properties.[104,105]

Unfortunately a detailed knowledge of the types, amounts and spatial variation of aggregated polymer chains throughout thin films has been lacking as well as the specific morphological and composition factors that regulate aggregate formation. Moreover, the impact of these structures on photocurrent generation in solar cells has also been difficult to ascertain on the sub-micron size scale and usually must be inferred from processing-dependent changes in ensemble current-voltage (I-V) and external quantum efficiency (EQE) curves.[105-107] Herein, we systematically perturb thin film morphologies and compositions in a prototypical polymer/fullerene solar cell material to investigate the types and spatial distributions of aggregates and directly correlate these features to local device photocurrent generation efficiency that may help guide new materials design schemes to control the amount and spatial location of aggregates to maximize device performance.

Thin film solar cells consisting of poly-(3-hexylthiophene) (P3HT) and [6,6]-phenyl-C_{61}-butyric acid methyl ester (PCBM) blends in a ~1 : 1 wt/wt ratio have consistently achieved power conversion efficiencies of ~6%, making them the current leader in this field.[108-110] It is widely accepted that the dominant contributor to high efficiency in this system is the establishment of highly ordered (crystalline) polymer regions that promote efficient charge transport.[6,25,26] Molecular structure factors such as side chain group size, molecular weight, polydispersity and P3HT/PCBM loadings all play essential roles in determining the film morphology characteristics and, most importantly, the local aggregation state of P3HT chains. Interestingly, optimal P3HT/PCBM morphologies have arrived from years of extensive, top-down trial and

error studies involving variation of loadings and processing conditions. Only recently, X-ray scattering studies of P3HT/PCBM blends and other promising polymeric candidate systems have demonstrated the importance of key steric factors that must be considered in the design of new material processing and synthetic schemes.[64]

Because the types and amounts of aggregated P3HT chains vary substantially throughout a thin film structures, a sensitive and high spatial resolution imaging technique is required to detect morphology-dependent variation of these structures in a functioning device and correlate their properties to local performance. Previous studies of aggregated polymer chains, particularly for the P3HT system, have been carried out by optical absorption and emission spectroscopy followed by theoretical lineshape analyses that specifically account for aggregation effects.[85,111] In P3HT, H-type (i.e. face-to-face) aggregation is most prevalent that results in non-Poissonian optical lineshapes that are also highly sensitive to film processing conditions that modify chain packing characteristics. Spano and co-workers developed a weakly coupled H-aggregate model to describe these lineshapes in terms of an exciton bandwidth parameter (interchain electronic coupling) that depends on both intra- and intermolecular order effects and conjugation lengths.[32,33,44,51] By fitting H-aggregate lineshapes in polythiophenes, it has been possible to extract microscopic details about the interplay between polymer structure and electronic properties in addition to quantifying the relative amounts of aggregated (ordered) and unaggregated (solution-like) polymer chains. However, absorption spectroscopy studies of aggregates in polymer thin films, especially P3HT/PCBM blends for solar cells, average over many nano- and microscopic size

domains that vary in both composition and structure thus masking the contributions of different regions of polymer aggregation types to the overall lineshapes. On the other hand, direct study of the role of polymer aggregation on photocurrent production in functioning devices can be fraught with complications from other materials necessary for proper device function (i.e. charge transport layers). To overcome these limitations, we use a highly selective resonance Raman and photocurrent imaging technique[3,27] that is capable of uncovering specific details about the local polymer aggregation state as well as the contribution to photocurrent generation.

P3HT/PCBM solar cell devices were fabricated with variable PCBM wt/wt loadings that, due to the lack of evidence of ground state charge transfer transitions, only affect the ability of P3HT molecules to form aggregates thus affecting energy transfer, charge generation and transport processes in the photovoltaic cycle. Absorption spectroscopy measurements are first performed to estimate the average amounts of aggregated and unaggregated (or, solution-like) P3HT chains by analyzing spectral lineshapes using the weakly coupled H-aggregate model of Spano and co-workers. Resonance Raman spectroscopy and imaging are then used to quantify and spatially map polymer aggregation properties on sub-micron scales within functioning devices. This is accomplished by using the P3HT C=C symmetric stretching band that can be decomposed into contributions from aggregated and unaggregated chains.[27] Photocurrent imaging is also performed in a simultaneous manner to establish direct correlations between aggregation characteristics and photocurrent generation efficiency that reveal the structure-function landscapes of these systems in realistic device structures.[3] A major

advantage of this approach is that, by careful selection of excitation energies, Raman signals from only the P3HT component can be resolved owing to the large resonance enhancements of P3HT Raman cross sections ($\sim10^5$) relative to all other material components in the device structure. This feature permits the study of embedded polymer chains and their aggregation properties in a highly selective manner thus avoiding unwanted complications from overlapping bands from hole transport layers and PCBM that could easily overwhelm IR absorption and off-resonance signals.

4.2 Results and Discussion

Linear optical absorption and emission spectroscopy have so far proven most useful for studying aggregation effects and the relative amounts of aggregated species in polythiophene thin films.[44,51,85,111] In particular, the weakly coupled H-aggregate model developed by Spano and co-workers has been successfully applied to polythiophenes to describe their optical absorption and emission lineshapes in terms of the interchain electronic coupling (exciton bandwidth) that is dependent upon both intra- and interchain microscopic order and conjugation lengths.[21-24] We previously extended this model to P3HT/PCBM (1 : 1 wt/wt) films where the amounts and type of aggregated chains were determined from both Raman and optical absorption spectra for different processing conditions.[27] Herein, the PCBM weight fraction and annealing treatments are varied in a controlled manner to modulate P3HT aggregation properties.

4.3 Order and Disorder Characteristics

We first qualitatively consider the impact of variable PCBM loadings and annealing treatments on the P3HT aggregation state by studying the averaged optical and vibrational spectroscopic signatures of P3HT/PCBM thin films. Figure 4.1 presents absorption spectra in the P3HT π-π* region (~15000-25000 cm^{-1}) and Raman spectra depicting the P3HT symmetric stretching backbone region (i.e. C-C, ~1380 cm^{-1}, and C=C, ~1455 cm^{-1}, modes) for as-cast a), b) and annealed c), d) P3HT/PCBM thin films of varying PCBM weight fraction (i.e. 1 : n; n=1-4), respectively. In order to observe the average Raman response from these variable loading films, the spectra in Figure 4.1b,d were obtained by averaging >900 individual Raman spectra over a 20-30 μm area. Because Raman spectra are excited on resonance with π-π* transitions, only Franck-Condon active vibrational modes are selectively enhanced. This feature makes spectra quite simple and the relative intensities of Raman bands are highly sensitive to local fluctuations in composition and morphology that can be exploited to map the P3HT aggregation state.

Absorption and Raman spectra in the P3HT region of both as-cast and annealed films show progressive overall blue-shifts for increasing PCBM content. Interestingly, absorption and Raman lineshapes of as-cast films with >1 : 1 wt/wt loadings change very little and closely resemble dilute solution P3HT spectra (see Figure 4.1) and marked reductions in signal-to-noise ratios are also observed with increased PCBM content. Upon annealing, absorption maxima show apparent red-shifts of the P3HT component of up to ~1000 cm^{-1} and corresponding P3HT C=C symmetric Raman bands show ~20 cm^{-1}

red-shifts. Spectroscopic evidence of aggregated P3HT chains is most apparent from the onset regions of annealed P3HT/PCBM absorption lineshapes (Figure 4.1c) where dominant progressions in the P3HT symmetric stretching C=C mode (~1400 cm^{-1}) are clearly resolved. Surprisingly, vibronic linewidths near the P3HT onset region diminish with increased PCBM concentrations but become increasingly congested from overlapping transitions from unaggregated P3HT chains at energies >20000 cm^{-1} as seen below.
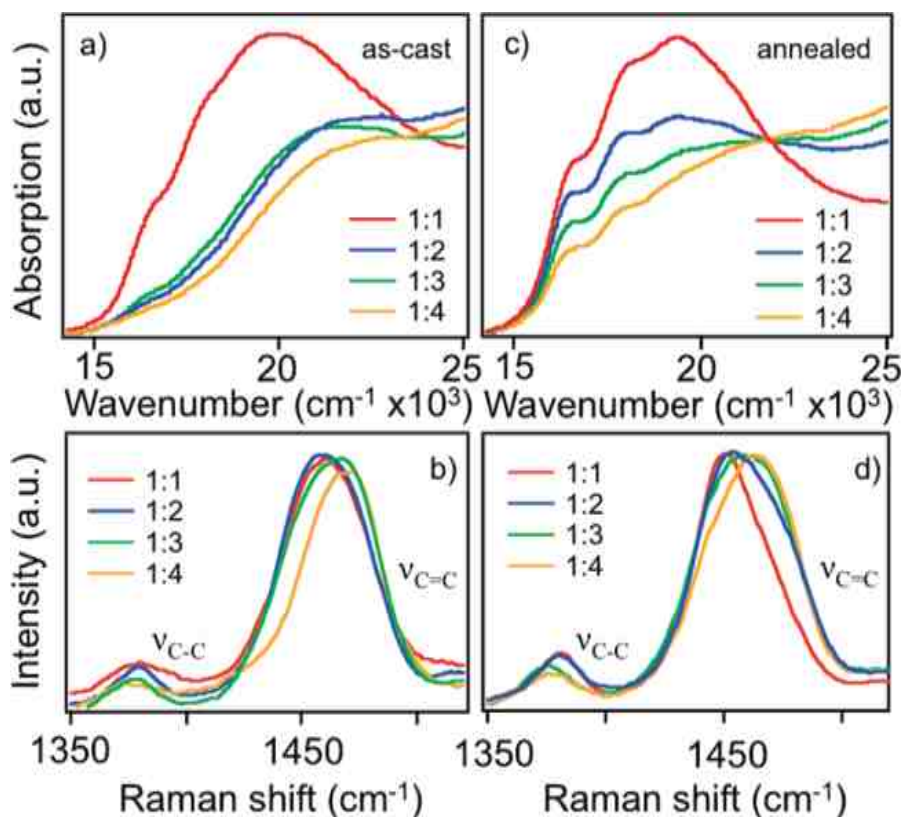
Figure 4.1: Absorption and averaged Raman spectra of 1 : 1, 1 : 2, 1 : 3 and 1 : 4 P3HT/PCBM as-cast a); b) and annealed, c); d) blend thin films. Raman spectra highlight the P3HT symmetric stretching backbone region with the C=C and C-C modes labeled.

Comparatively, P3HT C=C Raman modes exhibit high sensitivity to annealing treatments and PCBM content which is shown in the following to originate from changing amounts of aggregated and unaggregated P3HT chains. Other P3HT skeletal vibrations such as C-C intra- and inter-ring modes as well as thiophene ring C-H bending modes also show marked changes with increasing PCBM loading that can be attributed to

62

subtle changes in chain planarity.[112] Previous absorption and Raman spectroscopic studies of P3HT/PCBM composite films have attributed the large observed spectroscopic lineshape changes and band maxima shifts to changes of either conjugation lengths or crystallinity (order) or both.[113-115] In this framework, the blue-shifts of absorption and Raman spectra with increasing PCBM content result from more disordered P3HT chains due to the ability of PCBM to break up aggregated polymer chains. On the other hand, red-shifts of absorption and Raman spectra with annealing are rationalized by increased phase segregation that promotes polymer aggregation. While qualitatively useful, these largely phenomenological generalizations often fail to capture the impact of local morphology and composition on these important material structure characteristics and their contribution to local device performance. We now delve further into these structure-property relationships and establish useful correlations between the polymer aggregation state and device photocurrent generation on the sub-micron size scale.

4.4 Uncovering Spectroscopic Contributions of Aggregated P3HT Chains

The weakly coupled H-aggregate model is now used to fit the resolved absorption onset region (i.e. 0-0 and 0-1 vibronic transitions) and estimate the effect of variable PCBM content on the type and amounts of aggregated P3HT chains. The model has a single electronic origin with a vibronic progression in the P3HT C=C symmetric stretching mode (ca. 1400 cm^{-1} in the excited state) and a constant Huang-Rhys factor (S) of 1.0. The Gaussian vibronic linewidth (σ), energy of electronic origin (E_{0-0}) and exciton bandwidth (W) parameters are then adjusted to obtain a good fit of $0 - 0/0 - 1$

absorbance ratios. The justification for keeping S fixed in the fitting routine is the fact that inter-chain interactions usually dominate over intra-chain effects, such as bond distortions, from the unique affinity of P3HT to form extended aggregated structures.[51] Fit parameters are collected in Table 4.1 and a slight decrease of these parameters with increased PCBM content is observed.

Table 4.1: Fit parameters used for calculating aggregate component spectra.[a]

P3HT/PCBM wt/wt ratio	W (cm^{-1})	FWHM (cm^{-1})[b]	E$_{0-0}$ (cm^{-1})[b]
1 : 1	980	850	16530
1 : 2	805	830	16500
1 : 3	805	835	16490
1 : 4	870	845	16480

[a.] Huang-Rhys factor (S) was set to 1.0 and the vibrational frequency for the dominant progression forming mode (C=C) was fixed at 1400 cm^{-1} for all simulations. [b] Fit parameter tolerance was approximately +/- 4%.

Figure 4.2 shows experimental spectra (solid red traces with open squares) and fit spectra (dotted trace) for varied wt/wt P3HT/PCBM annealed thin films. Unfortunately, it was not possible to obtain reliable fits from as-cast films of >1 : 1 loadings due to the very small signal- to-noise ratios near the aggregate absorption onset region and we instead concentrate solely on annealed film data. By fitting only the resolved vibronic onset region of the spectrum (i.e. $0-0/0-1$ vibronic peaks) it is immediately apparent that experimental spectra cannot be reproduced by the H-aggregate model alone because

64

of overlapping transitions from unaggregated P3HT chains that increase with PCBM loading.
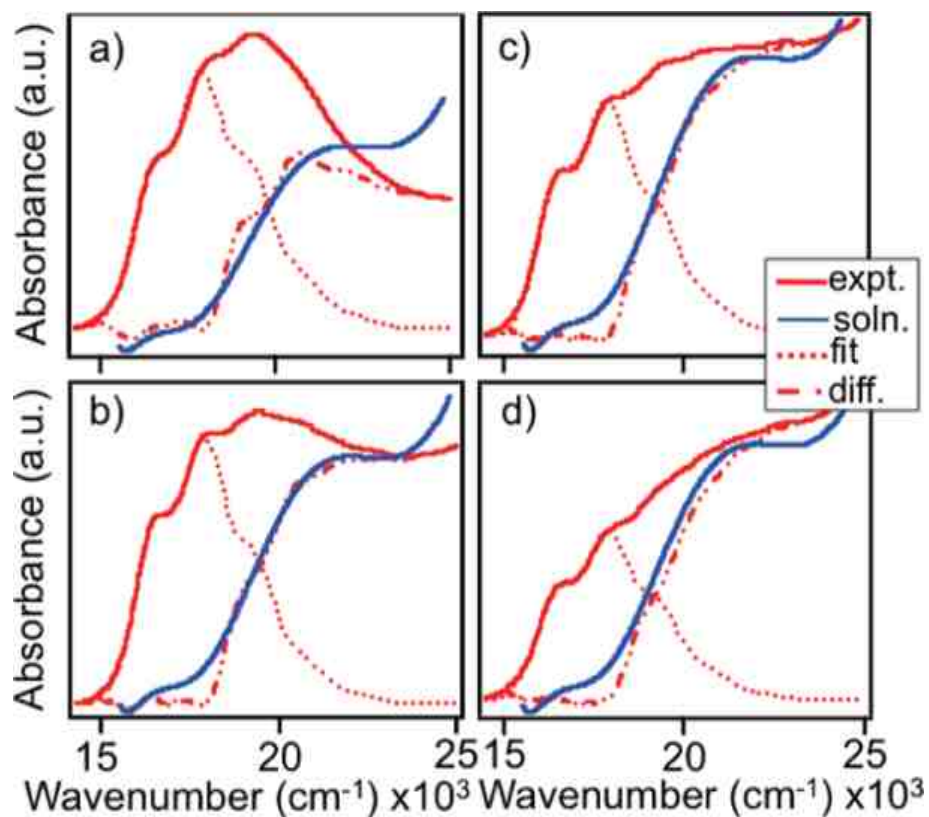
Figure 4.2: Experimental absorption spectra (solid red traces with squares) and fits (dotted traces) using a weakly coupled aggregate model for 1 : 1 (a), 1 : 2 (b), 1 : 3 (c) and 1 : 4 (d) P3HT/PCBM annealed thin films. Fit spectra are subtracted and difference spectra (dash-dot traces) plotted against dilute P3HT solutions (solid blue traces with open circles).

Fit spectra are then subtracted from experimental spectra to reveal contributions from unaggregated chains (dashed traces) that lack resolved vibronic structure

presumably due to large displacements of low frequency torsional vibrations and inhomogeneous broadening. For comparison, we show P3HT dilute solution spectra (solid blue trace) that have similar energies and linewidths as difference spectra. In addition absorption lineshapes of regio-random P3HT thin films have similar features as the dilute solution and unaggregated contributions albeit slightly higher transition energies, displayed in Figure 4.3 but, nonetheless, confirm that unaggregated chains in P3HT/PCBM blends more closely resemble dilute solution conformations with large conformational disorder.
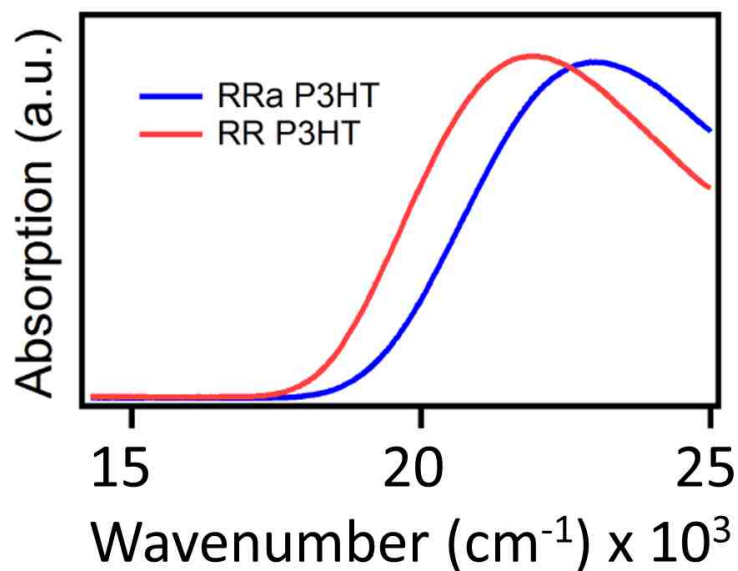
Figure 4.3: Absorption spectra of regio-random P3HT solution (blue) and unaggregated components from P3HT solution (red).

Comparing fit spectra with increased PCBM content reveals small, but discernible, increases in vibronic linewidths and $0 - 0$ absorption strengths in addition to slight red-shifts that correspond to reductions in σ, W, and $E_{0\text{-}0}$ fit parameters, respectively (see Table 4.1). Generally, smaller $0 - 0/0 - 1$ ratios are indicative of larger exciton bandwidth and smaller conjugation lengths. On the other hand, increases in $0 - 0/0 - 1$ ratios indicate reduction of exciton bandwidths due to increased intra-chain order and conjugation lengths. From the small increases in $0 - 0/0 - 1$ absorption ratios it is apparent that, while the overall amount of aggregated chains decrease, these

chains are self-aggregating into ordered conformations which is expected in more PCBM-rich films since extended interchain interactions are less likely to form. A high correlation coefficient (~0.92) was also found for the exciton bandwidth and linewidth fit parameters that further support a shift toward increased intra-chain order and a narrower distribution of conjugation lengths with increased PCBM loading.

Alternatively, the observed lineshape changes for the aggregated P3HT component absorption spectrum could arise from a "chemical pressure" effect whereby larger PCBM contents (domain size) cause a reduction in the Huang-Rhys factor by squeezing the smaller P3HT domains due to unfavorable thermodynamic mixing factors. In order to determine whether these effects are at play in P3HT/PCBM annealed thin films, we allowed the Huang-Rhys parameter to vary while holding the exciton bandwidth term fixed at 980 cm^{-1} from the 1 : 1 wt/wt film. Upon increasing the PCBM loadings from 1 : 1 to 1 : 4, it was found that the Huang-Rhys parameter decreased from 1.0 to 0.76. Assuming no mixing of vibrational modes this corresponds to a decrease of average C=C bond distances of ~0.05Å. Because distortions of this size are only likely to occur under applied hydrostatic pressures of >10 kbar,[93] we instead propose that P3HT chains self-aggregate with larger PCBM content.

From the above fitting procedure, it is useful to estimate the relative amounts of aggregated and unaggregated chains in annealed P3HT/PCBM films. However, increased spectral overlap between unaggregated P3HT transitions and PCBM absorption onsets with higher PCBM content can make accurate estimates difficult. In order to avoid complications from PCBM absorption at higher frequencies (i.e. >23000 cm^{-1}) a

Gaussian function is fitted to the P3HT dilute solution spectrum and scaled to match the onset of the difference spectrum generated from the fitting procedure described above. The ratio of integrated areas from the calculated (aggregate) spectrum and the scaled Gaussian lineshape representing the contribution from unaggregated chains P3HT components ($A_{agg.}/A_{unagg.}$) was found to decrease with higher loadings, namely, 2.6 (1 : 1), 1.88 (1 : 2), 1.44 (1 : 3) to 1.10 (1 : 4). This decrease is consistent with the fact that increased PCBM content can effectively prevent P3HT chain aggregation. In addition to complications arising from the overlap of PCBM absorption onsets, the markedly different lineshapes (Franck-Condon factors) of aggregated and unaggregated components highlight the inherent difficulty of estimating the relative contributions of these chains to the overall absorption lineshape. Fortunately, more reliable estimates can be obtained from Raman spectroscopy that also provides the basis for spatially mapping this important structural feature of the P3HT component on the sub-micron size scale.

4.5 Mapping the Spatial Distributions of Aggregated P3HT Chains

Several research groups have previously employed Raman spectroscopy for understanding the effect of processing conditions on P3HT/PCBM blend thin film morphologies. In particular, large overall red-shifts of the P3HT C=C symmetric stretching Raman bands are observed after annealing[116,117] that are commonly explained in terms of increased polymer conjugation lengths and crystallinity. However, in a previous report, we demonstrated that this band can be decomposed into contributions from both aggregated and unaggregated chains with characteristic frequencies of ~1450

cm^{-1} and ~1470 cm^{-1}, respectively, which are consistent with spectra from ordered (crystalline, regio-regular) and amorphous (solution, regio-random) of related thiophene systems.[35,118,119] In this model, the large overall spectral shifts occurring upon annealing are rationalized in terms of the relative amounts of both species changing with processing conditions that cause apparent shifts in band maxima. This model primarily demonstrates the importance of interchain effects (similar to absorption lineshape changes) since the overall P3HT C=C frequency shifts are too large to occur by increases in conjugation lengths alone. Moreover, the Raman approach for quantifying the amounts of aggregated and unaggregated species is much more reliable than absorption spectroscopy since there are no complications from multiple Franck-Condon vibrational progressions and overlapping PCBM bands. A major goal of this paper will be to extend this model to understand how the P3HT aggregation state is affected by structural perturbations from variable PCBM loadings and determine how do both intra- and intermolecular factors regulate the types and distributions of aggregates.
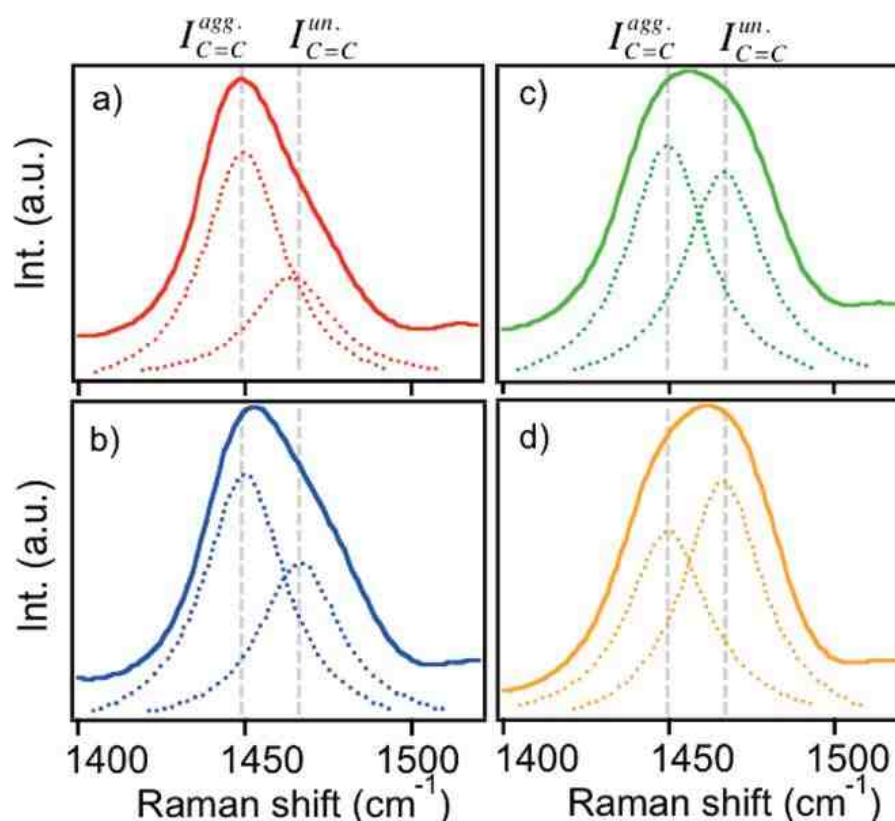
Figure 4.4: Raman spectra of a) 1 : 1, b) 1 : 2, c) 1 : 3, and d) 1 : 4 wt/wt P3HT/PCBM thin films in the C=C symmetric stretching mode region of the P3HT component generated by averaging over 900 spectra from imaging experiments (see Figure 4.6). C=C bands are decomposed into contributions from aggregated (ca. 1450 cm^{-1}) and unaggregated (ca. 1470 cm^{-1}) chains.

Similar to absorption spectra characteristics, P3HT C=C Raman lineshapes (shown in Figures 4.1b, d) also show progressive blue-shifts due to an increase in the amounts of unaggregated P3HT chains with increased PCBM content. In order to quantify the degree of P3HT aggregation from Raman spectra, we use we use idealized Lorentzian lineshape functions for the two components representing both aggregated

(1450 cm^{-1}) and unaggregated (1470 cm^{-1}) P3HT chains are fitted to the experimental C=C Raman band and we use the ratios of integrated areas of these components to estimate the P3HT aggregation ratio, or "R" value ($I_{C=C}^{agg.}/I_{C=C}^{un.}$). Figure 4.4 shows Lorentzian fits of averaged Raman spectra of P3HT/PCBM of variable loadings: a)1 : 1, b) 1 : 2, c) 1 : 3, and d) 1 : 4. As the PCBM concentration increases, the unaggregated component increases confirming that P3HT chains are in increasingly twisted or solution-like conformations. From averaged spectra, the ratios of aggregated/unaggregated P3HT chains were found to be 3.2 (1 : 1), 1.9 (1 : 2), 0.9 (1 : 3), and 0.7 (1 : 4) which are comparable to estimates generated from absorption fits described above. Interference from both PCBM and PEDOT:PSS hole transport materials C=C modes (~1465 cm^{-1}) have a negligible effect on "R" values even at higher loadings due to the large disparity in Raman cross sections that are estimated to be several orders of magnitude smaller than that of P3HT for the excitation wavelength used (488 nm).
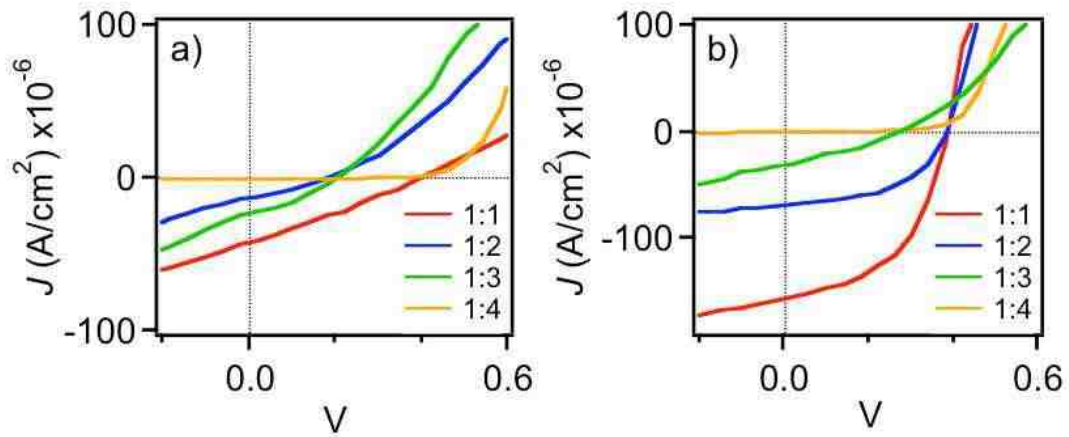
Figure 4.5: Current-voltage (I-V) curves for a) as-cast and b) annealed P3HT/PCBM devices of varying composition under exposure to white light (~100 mW/cm2).

In order to spatially correlate the P3HT aggregation state to local photocurrent generation efficiency, functioning P3HT/PCBM solar cell devices of variable wt/wt loadings were first characterized I-V and EQE measurements to assess the average changes in electrical properties with changing composition and morphology. Generally, short circuit current densities (J_{SC}) and EQEs decrease considerably with increasing PCBM loadings suggesting that charge generation and charge transport efficiencies decrease due to the reduction in P3HT/PCBM interface area and crystalline P3HT regions necessary for splitting photogenerated excitons and extended charge migration pathways, respectively (see Figure 4.5). It is also important to stress that diminished photocurrent production arises from reduced amounts of P3HT chromophores in the device active layers that can be inferred from reductions in the overall P3HT absorption. However, we

focus specifically on the changes incurred in the P3HT component, in particular, its spatially varying aggregation properties determined from the RRPI approach.
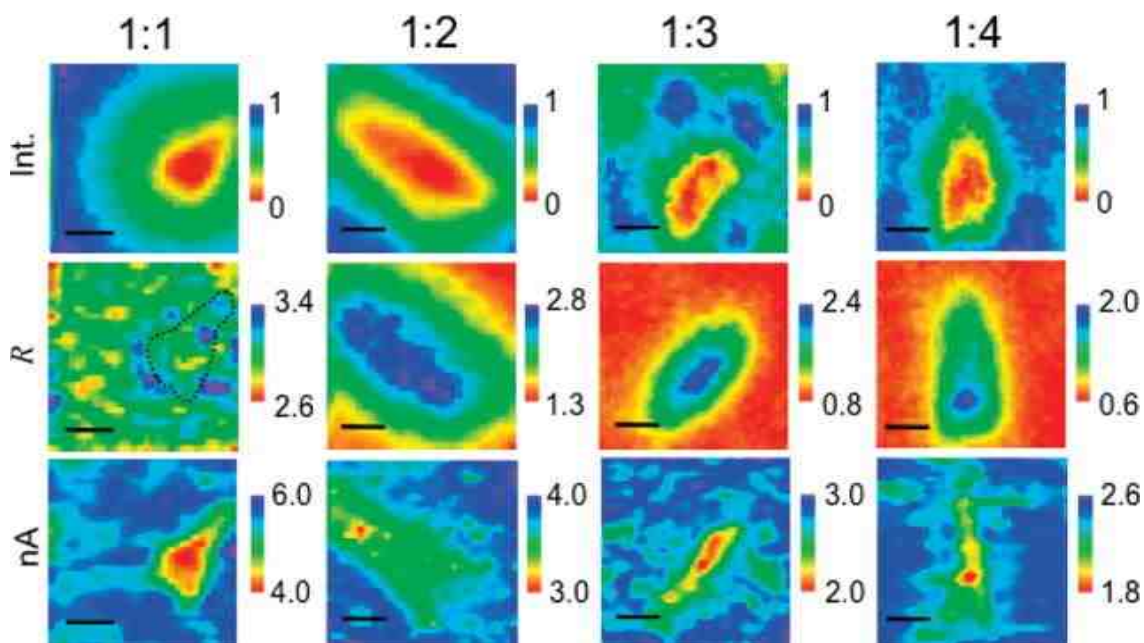
Figure 4.6: Raman intensity (top row), aggregation (R) (middle row), and photocurrent (bottom row) images of annealed P3HT/PCBM solar cell devices (scale bars =3 μm). A sketch outline of the PCBM-rich region in the 1 : 1 wt/wt film is superimposed on the "R" image.

Figure 4.6 shows P3HT C=C mode total integrated intensity, "R" (aggregation state) images, and photocurrent images for P3HT/PCBM thin films of 1 : 1, 1 : 2, 1 : 3 and 1 : 4 wt/wt loadings. We emphasize regions of the films that possess both P3HT and PCBM-rich areas (namely crystallites for the latter) and we observe similar morphological characteristics as seen in previous reports using c-AFM techniques.[120] In

general, P3HT C=C total integrated Raman intensities show significant reductions in PCBM-rich regions which is confirmed by performing bright-field optical imaging in the same area (data displayed in chapter 2). "R" images reveal the spatial variation of the P3HT aggregation state due to local morphology fluctuations. Generally, the largest changes in R values tend to occur around PCBM crystallites for 1 : 1 loadings which is consistent with our previous findings.[3] Surprisingly, minority P3HT chains inside PCBM-rich regions for higher (>1 : 2) PCBM loadings show increased aggregation. This result is quite intriguing since P3HT aggregation should be entirely suppressed due to the small amounts of P3HT in these regions (based on corresponding Raman intensities) from nearly complete phase segregation. Smaller R values of P3HT-rich regions surrounding PCBM crystallites in films of >1 : 1 wt/wt loadings indicate that these chains are primarily unaggregated due to the increased amounts of PCBM that effectively inhibit aggregation. These aggregation maps are consistent with trends observed in absorption spectra but have the distinct advantage that the spatial locations of aggregated chains can be determined. Another possible explanation for the reversal in aggregated chain spatial distributions may be that minority P3HT molecules form a "skin" around the PCBM crystallites as seen in polyphenylenevinylene/fullerene thin films of 1 : 4 wt/wt ratios.[121] While we cannot completely rule out this possibility, we instead believe that P3HT chains become trapped in the PCBM crystallites which forces them to take on ordered but collapsed or, self-aggregated, conformations to minimize interactions with surrounding fullerene molecules that is supported from previous AFM images of P3HT/PCBM blends that clearly show exposed PCBM crystallites surrounded by P3HT-rich regions.[27,120,122]

While it is known that crystalline, or aggregated, P3HT networks are necessary to promote good charge transport and ultimately device performance, very little is understood about how aggregated regions of different sizes and compositions contribute to photocurrent generation. We now attempt to address this issue by comparing R and photocurrent images for variable P3HT/PCBM loadings. Photocurrent images are shown in the bottom row for each loading in Figure 4.6 and, similar to bulk device I-V curves, average photocurrent production decreases with increased PCBM loadings. Further examination of photocurrent images reveals that decreased production occurs from within regions corresponding to PCBM crystallites (i.e. low Raman intensity). However, small reductions of photocurrents are also found in regions of high P3HT aggregation in 1 : 1 P3HT/PCBM devices presumably due to complete phase separation of both components or possibly charge trapping by surrounding unaggregated regions.[3,123] This feature illustrates the sensitivity of local aggregation and composition that must be balanced for optimal performance but is usually difficult to resolve in conventional spectroscopy and scanned probe techniques. Since most aggregated P3HT chains for films with PCBM loadings of 1 : 2 and larger reside within PCBM crystallites, photocurrent decreases are most likely due to the lack of extended P3HT aggregate networks. Unfortunately, photocurrent signal-to-noise ratios of these devices decrease significantly with higher PCBM loadings making a detailed quantitative comparison difficult and we are presently exploring new device architectures to maximize photocurrent collection efficiency. This effect is not only due to both reduced concentrations of P3HT and a greater amount of unaggregated chains, but also the spatial locations of aggregates.

The spatial mapping of the P3HT aggregation state to local photocurrent generation provides valuable insights into the intrinsic variation in polymer packing characteristics that change with PCBM content that augments current understanding borne out from previous ensemble device characterization studies of P3HT/PCBM devices with varying compositions.[124] The unexpected change in the location of aggregated P3HT chains and reduction of interchain exciton couplings in films of 1 : 2 loadings and higher requires further exploration. We now delve into the specific structural (i.e. chain conformational characteristics) factors that regulate the type of aggregation and the locations of aggregated regions as well as key electronic structure parameters previously determined from ensemble absorption spectra.

4.6 P3HT Aggregation Mode Changes with Increased PCBM Content

Along with changes in the dominant P3HT C=C Raman lineshapes due to changes in the relative amounts of aggregated and unaggregated chains, other P3HT skeletal vibrational modes can provide additional insights into the changes of conformational attributes of P3HT chains observed in these films. we previously noted that P3HT C-C mode Raman band frequencies and intensities also increase with annealing treatments in films of 1 : 1 loadings that also coincides with regions greater aggregation amongst P3HT chains.[27] This effect was assigned as an increase in chain planarity which should, intuitively, be correlated to the P3HT aggregation state. From Figures 4.1b,d, the average C-C mode intensities and frequencies decrease with increased PCBM loadings indicating diminished charge density in these bonds due to the more

twisted character of thiophene rings corresponding to lower aggregation (i.e. smaller R values). However, these trends can be misleading since they only report the average over the entire film. On this note, it is more informative to construct maps of P3HT C-C frequencies (v_{C-C}) and the C=C aggregated frequency component ($v_{C=C}^{agg.}$) (shown in Figure 4.7) to uncover spatial correlations between chain planarity and aggregation.
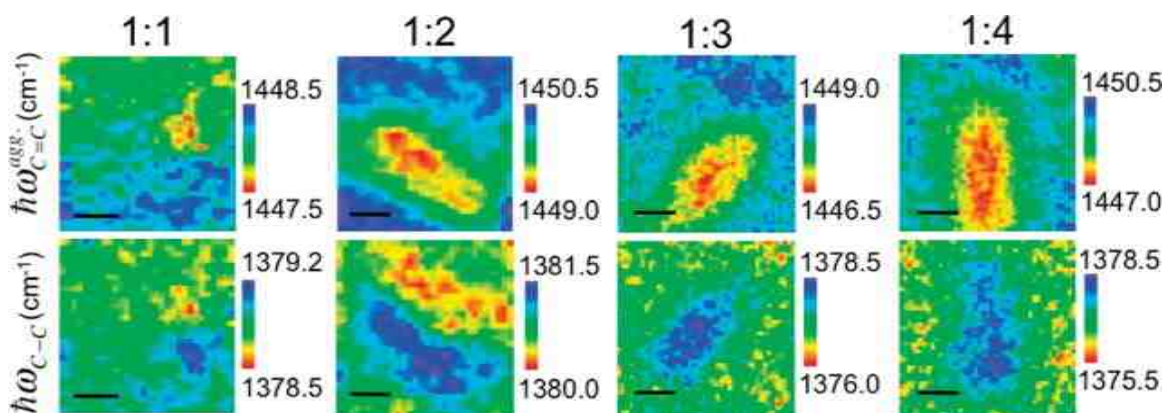
Figure 4.7: P3HT C=C aggregate component and C-C Raman frequency images for variable loading P3HT/PCBM thin film devices (scale bars =3 μm).

Generally, values of $v_{C=C}^{agg.}$ are lower in aggregated regions whereas v_{C-C} show larger values in these same regions. The apparent blue-shifts of the latter also correspond to marked increases in the intensities of this mode. This effect is indicative of increased delocalization amongst chain segments due to enhanced chain planarity and is most distinct in films of >1 : 1 P3HT/PCBM loadings. Unfortunately, it is not possible to compare absolute frequencies due to minor fluctuations in instrument calibration between samples, however, the observed trends did not change. Another intriguing explanation

for the observed increases in the C-C intensities and apparent blue-shifts is the tendency of P3HT chains to adopt a quinoid structure with increased aggregation. While this possibility requires further study, related Raman and absorption spectroscopic studies on both aromatic and quinoidal oligothiophenes reveal similar trends as presented here.[125] [126] Furthermore, the quinoid form could be stabilized by aggregation interactions that become more prevalent with thermal annealing suggesting a cooperative effect between the polymer aggregation state and accessible resonance forms. Additionally, the use of C-C frequencies and intensities as a measure of planarity is also supported from Raman spectra measured of as-cast P3HT/PCBM and regio-random P3HT films that show low C-C band intensities (signal-to-noise ratios <2) and red-shifted frequencies with respect to annealed films due to the highly twisted nature of the thiophene rings in these systems that do not permit aggregation. Based on the effects of chain planarity on aggregation, we now attempt to establish relationships between the above structural characteristics of aggregated P3HT chains to the exciton bandwidth parameter, W, describing the extent of intra- and intermolecular order.
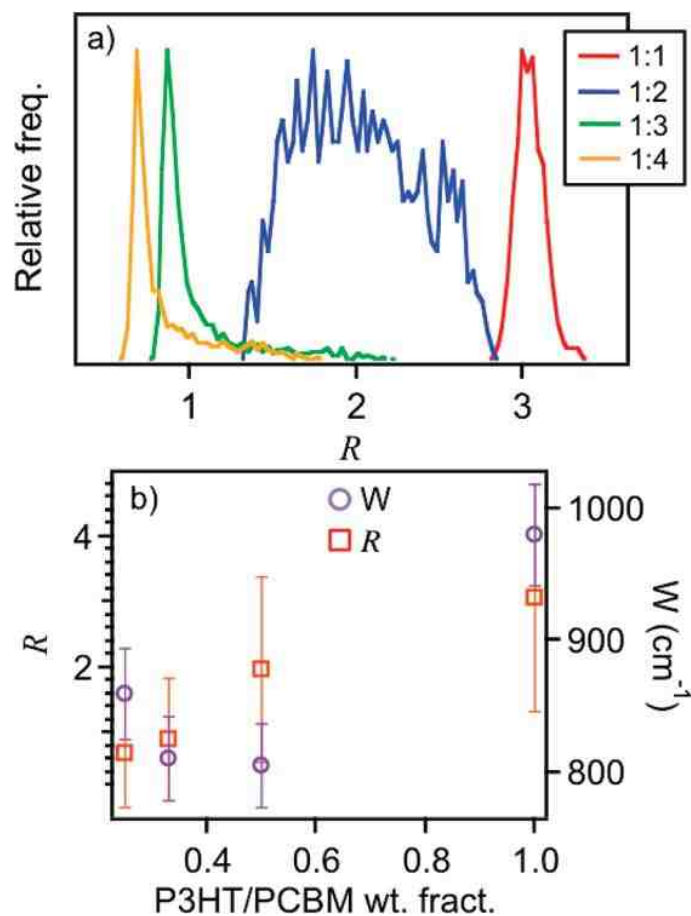
Figure 4.8: a) Histograms of the P3HT C=C "R" values shown in Figure. 4.6 for varying P3HT/PCBM content. b) Average P3HT aggregation (R) and exciton bandwidth (W) absorption spectra fit parameters as a function of P3HT/PCBM weight fraction.

For this comparison, it is helpful to re-cast R values into histograms to show how the distributions of aggregated P3HT chains change with variable loading. Figure 4.8a shows histograms of P3HT aggregation profiles generated from "R" images (Figure 4.6, middle row) revealing changes in the distribution behaviors of aggregation as PCBM

content changes. As the PCBM weight fraction is increased, distributions first become broader (i.e. 1:2) then transition to a relatively narrow maximum at small average R values (<1) with a long tail toward higher R values (i.e. >1 : 2 loadings). We assign aggregated chains in 1 : 1 loadings as interchain aggregates that gradually decrease due to interference from PCBM molecules at higher loadings. Since aggregated chains are known to facilitate charge transport, these histograms reveal changes in the distributions of the types of aggregated species not readily apparent from R images. This aspect is especially important since aggregated P3HT chains are widely believed to be current-carrying species in P3HT/PCBM solar cells and a shift of aggregation type could disrupt charge transport leading to increased recombination. To show dependence of exciton bandwidth parameter, W, on chain order, correlations between interchain coupling and the P3HT aggregation state were established. Fig. 4.8b shows plots of the parameters that decrease with increasing PCBM content that is also consistent with a shift from inter- to intra-chain aggregation interactions. A decrease in W suggests an increase in chain planarity and conjugation lengths for aggregated P3HT chains that result in lower interchain electronic coupling. This trend further explains the effect of self-aggregation of P3HT chains possibly into rod-like conformations that lead to significant reductions in overall photocurrent generation due to the loss of extended interchain aggregated networks that was supported by comparisons of the C-C and the C=C aggregated component frequency images in Figure. 4.7.

4.7 Conclusions

We have shown that increasing PCBM loadings result in a decrease of P3HT interchain aggregation interactions in P3HT/PCBM thin films that cause reductions in solar cell device performance. These morphology- and composition-dependent changes are manifested as increases in the $0-0/0-1$ absorption vibronic peak ratios in the aggregate portion of the blend thin film ensemble absorption spectrum in addition to decreases in P3HT C=C Raman aggregated vs. unaggregated component averaged intensity ratios. By constructing spatial maps of the P3HT aggregation state and local photocurrent generation, we are able to resolve the role of polymer aggregation in photocurrent production. Surprisingly, the majority of aggregated P3HT chains for films with PCBM loadings >1 : 1 were found to be localized within PCBM-rich regions which was not apparent from absorption spectra or device EQE studies. Fit spectra generated from the weakly coupled H-aggregate model also showed significant decreases in the exciton bandwidth parameter indicating increased intra-chain order. P3HT C-C and aggregated C=C mode frequency images supported this result and uncovered important correlations between the polymer aggregation state and chain planarity that, together with aggregation image profiles, are consistent with a shift from predominantly inter- to intra-chain aggregation. Histograms of P3HT aggregation state (R values) distributions as well as were also used to show the transition of the type of aggregated P3HT chains from a primarily interchain type to intra-chain (self) aggregated chains within PCBM-rich areas. Moreover, the spatial location of aggregates revealed from these RRPI studies also sheds light on previously misunderstood relationships. We thus conclude that optimal device

performance is achieved when P3HT chain aggregation is largely of interchain type which is only realized in films of 1 : 1 wt/wt ratios. Although previous trial and error studies of varying film composition and processing conditions have alluded to the importance of such aggregation effects, this work now reveals the molecular structure factors that govern not only aggregate concentration but also its spatial location in the film. Overall, the combined RRPI and weakly coupled H-aggregate model fits of absorption spectra reveal new insights into the structural attributes and roles of aggregated chains on material performance that are not available from conventional device characterization techniques.

CHAPTER 5

Aggregates Promote Efficient Charge Transfer Doping of

Poly(3-hexylthiophene)

(Submitted)

5.1 Introduction

Charge transfer doping of conjugated polymers by small molecule acceptors has seen increased use for tuning the electronic properties (i.e., Fermi levels) of these optoelectronic materials.[7,8,11] Efficient doping is usually realized when sufficient offset exists between the polymer HOMO and acceptor LUMO levels.[7,9,127] One of the best studied polymer/dopant systems meeting this criterion is poly(3-hexylthiophene) (P3HT) doped with 2,3,5,6-tetrafluoro-7,7,8,8-tetracyanoquinodimethane (F$_4$-TCNQ) where the P3HT HOMO lies at ~5 eV compared to the LUMO of F$_4$-TCNQ at ~5.3 eV.[11,94,127-130] Surprisingly, the maximum doping efficiency in P3HT/F$_4$-TCNQ is only about 5% indicating that charges remain tightly bound.[10] Pingel and Neher recently showed compelling evidence for the integer charge transfer description where, as opposed to a hybrid complex, free charges form immediately upon P3HT and F$_4$-TCNQ contact but most remain in a bound state, hence, lower than expected doping efficiencies.[10,127] The interaction between P3HT and F$_4$-TCNQ was also shown recently by Duong et al. to result in a new, ordered mixed phase.[131] Despite advances toward understanding the

basic mechanisms of doping with F_4-TCNQ, the role of polymer conformation and packing (aggregation) characteristics on doping efficiency remains relatively unexplored.[7-10] This is especially important for doping solution-processed polymers since solvent-solute interactions regulate the folding and packing of chains and P3HT/F_4-TCNQ charge transfer occurs in the solution phase prior to deposition of thin films.[11,131]
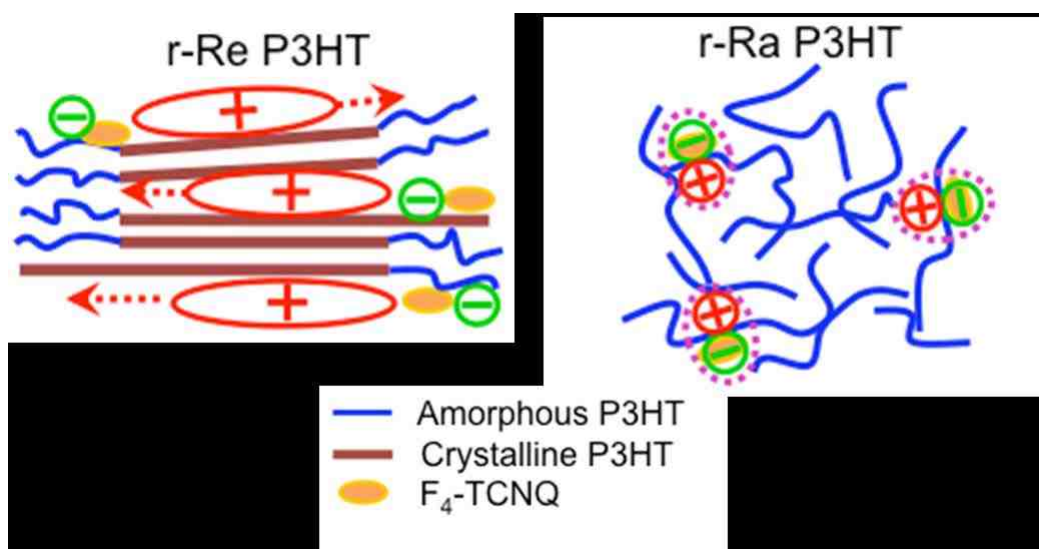
Figure 5.1: Diagram of proposed D/A interactions in r-Re and r-Ra P3HT/F_4-TCNQ blends.

We use a combination of electron paramagnetic resonance (EPR), NMR, optical absorption and Raman spectroscopy on regio-regular (r-Re) and regio-random (r-Ra) P3HT variants doped with F_4-TCNQ to understand how conformation and packing of polymer chains influences the nature of interaction with the dopant and doping efficiency. The primary difference between these two P3HT forms is their ability to form

π-stacked aggregate structures, which is only possible in r-Re samples.[132,133] Additionally, charge (hole) injection favors increased quinoidal character[134-137] resulting in increased chain rigidity, planarity and greater intrachain charge delocalization. Aggregated P3HT chains are expected to more readily adopt quinoid forms owing to the relatively high intrachain order (planarity) already possessed implying smaller torsional reorganization energy barriers.[17] Importantly, the fact that the amounts and sizes of P3HT aggregates in solution may place an upper limit on the maximum achievable doping efficiency in solution processed doped polymers.
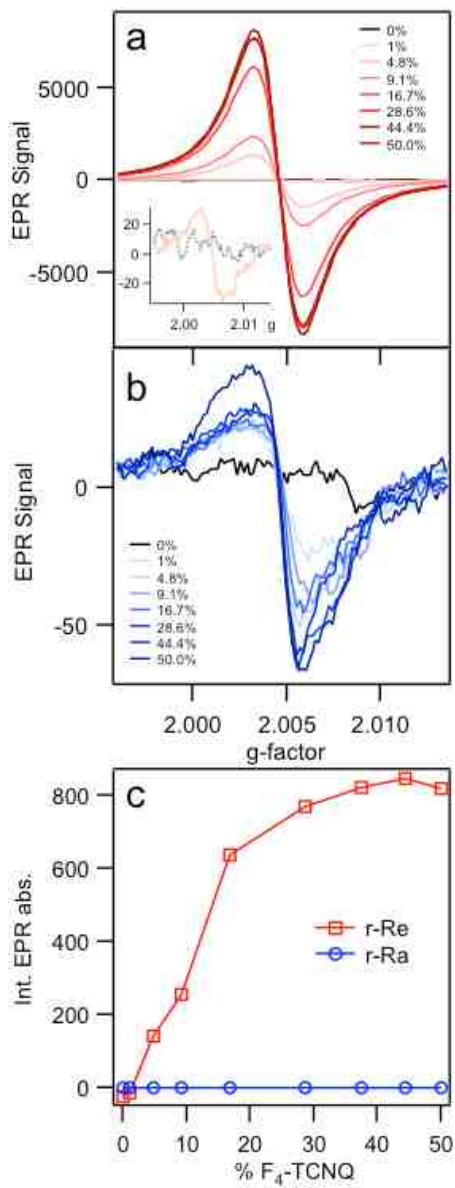
Figure 5.2: X-band EPR spectra of F_4-TCNQ doped P3HT chlorobenzene solutions. a) regio-regular (r-Re), b) regio-random (r-Ra), c) comparison of integrated EPR signals from both forms as a function of dopant concentration.

5.3 Electron Paramagnetic Resonance

We begin by evaluating EPR spectra in the X-band range of r-Re and r-Ra P3HT in chlorobenzene (CB) solutions with varying amounts of F_4-TCNQ (Figure 5.2). Samples preparation and details of instrumentation are provided in chapter 2. Importantly, both pristine P3HT and F_4-TCNQ solutions are EPR silent as shown in Figures 5.2 and 5.4 but a distinct resonance appears at 3346.35 Gauss once F_4-TCNQ is added. EPR spectra of doped r-Re P3HT thin film samples displayed in Figure 5.3 showed similar behavior as spectra in Figure 5.2. A small interaction between F_4-TCNQ and chlorobenzene was observed in aged samples exposed to air (Figure 5.4), but much weaker than signals obtained from doped P3HT samples in fresh solutions.
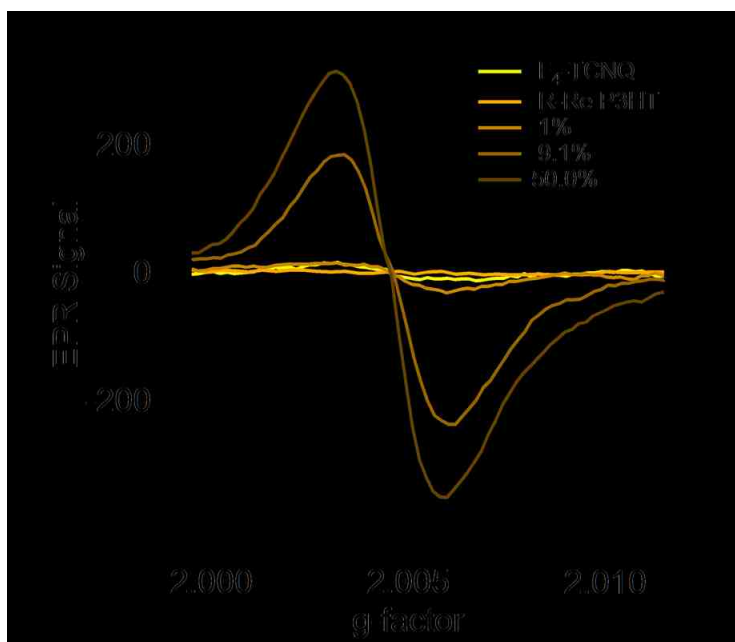
Figure 5.3: EPR spectra of r-Re P3HT/F_4-TCNQ blend thin film samples.

EPR spectra of r-Re samples (Figure 5.2a) show significant amounts of paramagnetic species formed at dopant levels as small as ~1%. The observed signal shows little anisotropy and corresponds to a g-value of ~2.0046 which is slightly larger than that of a free electron (g =2.0023) but within the range commonly observed for organic radicals.[138] A rapid increase of the signal was observed for up to ~20% F_4-TCNQ loading followed by only gradual changes at larger loadings. In contrast, EPR spectra of r-Ra P3HT doped with F_4-TCNQ show much smaller signals (i.e., several orders of magnitude lower) indicating very few paramagnetic species formed compared to those found in r-Re samples, albeit the g-value is similar. Integrated EPR absorption for both P3HT types for the same dopant loadings are highlighted in Figure 5.2c.
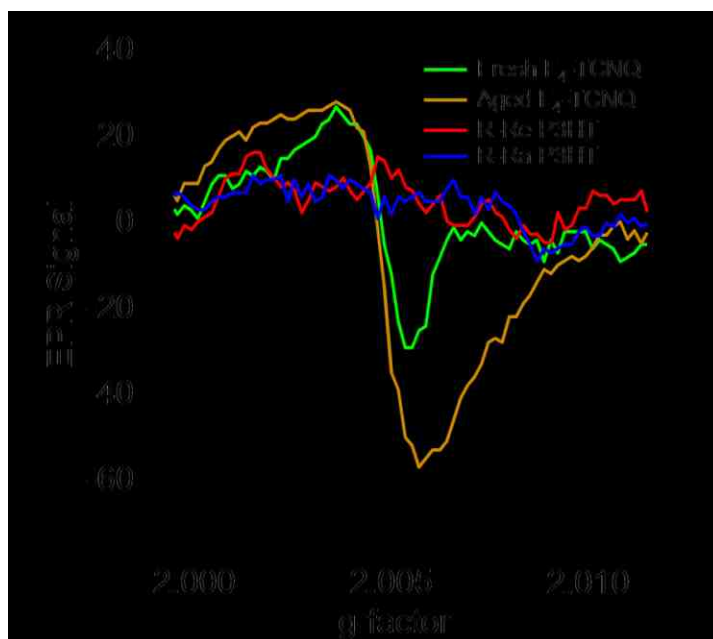
Figure 5.4: EPR spectra of r-Re and r-Ra P3HT samples in chloroform solution and comparison of EPR signals from fresh and aged (over one month exposed to air) F_4-TCNQ chlorobenzene solutions.

Putatively, the rapid increase of the doped r-Re sample EPR signal when F_4-TCNQ loadings are below 20% corresponds to the dopant filling accessible P3HT sites. The saturation of the EPR signal at F_4-TCNQ loadings higher than ~25% likely corresponds to the lack of dopant binding sites possibly indicating that formation of a new mixed phase is complete. It is proposed that efficient doping is realized by P3HT aggregates, which is only possible in r-Re P3HT.[139,140] This arises from the greater planarity (intrachain order) of P3HT chains in the aggregate π-stack that facilitate quinoidal distortions leading to delocalization of hole polarons.

5.4 ^{19}F NMR

A different perspective of polymer/dopant interactions and doping efficiency can be obtained from ^{19}F NMR spectroscopy to track the signatures of fluorine atoms on F_4-TCNQ using P3HT as the dopant. We start with neat F_4-TCNQ in deuterated chloroform solution, which shows a characteristic resonance at -131 ppm originating from the equivalent fluorine atoms on F_4-TCNQ as displayed in Figure 5.6.[141] Small quantities of r-Ra or r-Re P3HT are added eventually causing a loss of ^{19}F signal due to P3HT/F_4-TCNQ interactions.   Integrated spin densities of ^{19}F NMR spectra from F_4-TCNQ solutions with varying amounts of r-Re and r-Ra P3HT are shown in Figure 5.5. Interestingly, both P3HT types show a similar decrease in signal at P3HT loadings of <10%, indicating strong interactions with F_4-TCNQ. However, r-Re samples show rapid decay to background levels with ~10% P3HT added whereas r-Ra samples exhibit a more gradual decay to background levels only at much larger P3HT content (~70%).
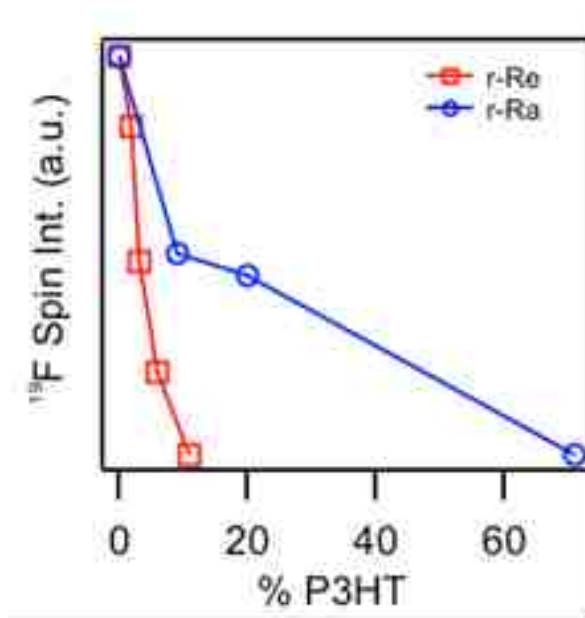
Figure 5.5: Integrated ^{19}F NMR intensities of F_4-TCNQ with varying amounts of r-Re and r-Ra P3HT in deuterated chloroform solutions.

There are two probable origins for the disappearance of the ^{19}F signal; i) reduction in the amount of neutral, diamagnetic F_4-TCNQ, and ii) paramagnetic species acting as a relaxation agent,[142] which may both be operative. At low P3HT levels (~1%), both types are expected to behave similarly due to the large excess of F_4-TCNQ, hence, the similar decrease in ^{19}F signals. The rapid loss of ^{19}F signal in r-Re samples is expected to originate from creation of paramagnetic relaxation centers which are much more efficient in quenching the ^{19}F signal of pristine, uncomplexed F_4-TCNQ. The slower decay of the ^{19}F signal for larger r-Ra P3HT loadings either results from tightly bound separated charges on donor/acceptor pairs or, integer charge transfer does not occur and instead

signal loss arises from encounter complex interactions. At this stage it is difficult to rule out either mechanism, which requires a deeper understanding of the molecular level interactions between P3HT and F_4-TCNQ.
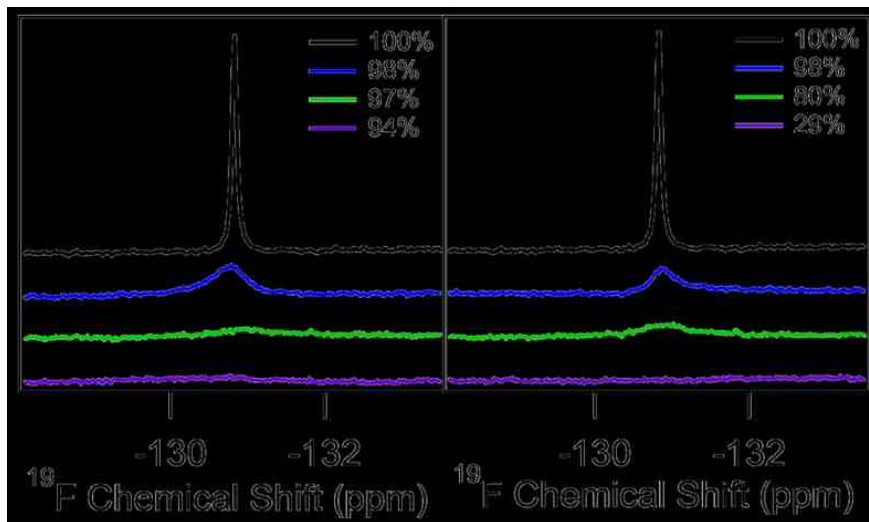
Figure 5.6: ^{19}F NMR spectra of F_4-TCNQ with varying amounts of a) r-Re and b) r-Ra P3HT in deuterated chloroform. The percentage shown in the graphs is F_4-TCNQ by weight with respect to the polymer.

5.5 Optical Absorption

We next turn to optical absorption spectroscopy, which should produce distinctly different lineshapes depending on whether charges remain bound or completely separate following encounter between each P3HT variant and F_4-TCNQ dopants.[10] For example, absorption transitions from F_4-TCNQ anions are apparent in the NIR region in r-Re P3HT samples that can only be explained by the integer charge transfer model.[10] If integer charge transfer is not operative, a hybrid transition corresponding to a charge

transfer complex between P3HT and F_4-TCNQ is expected.[10] However, it is also possible that tightly bound charges on the respective components following an initial integer charge transfer could give rise to a similar feature owing to their highly localized nature resulting in better overlap between hole and electron wavefunctions. Absorption spectra of r-Re and r-Ra P3HT in chlorobenzene solutions were recorded at several F_4-TCNQ amounts and displayed in Figure 5.7. The characteristic F_4-TCNQ anion absorption transition emerges in the NIR region for r-Re samples from both solution and thin film samples (see Figure 5.7 and Figure 5.8, respectively).[10,131] Similar to trends in EPR spectra, the F_4-TCNQ anion absorption lineshape reaches a maximum in the range of ~30-40% dopant concentration and shows only gradual increases past this level. It is also noteworthy that P3HT centered transitions with resolved vibronic structure appear and concomitantly increase with F_4-TCNQ amounts with a distinct peak at ~615 nm. Although this lineshape bears similarity to P3HT aggregate absorption transitions (i.e., well-resolved vibronic structure), we do not expect hole injection by F_4-TCNQ to induce aggregation similar to pristine P3HT. Instead, hole injection should increase P3HT backbone planarity most likely from increased quinoidal character that promotes greater chain rigidity and planarity.[134-137] This view is consistent with expected facile delocalization of hole carriers in these chains thus creating fully separated charge pairs (i.e., efficient doping). Thus, prior to filling all available sites on a P3HT chain, the excitons from these hyper-planarized doped chains resemble J-type aggregates, which is apparent from the prominent 0-0 transition. In a related study involving doping of P3HT/PCBM blends, we demonstrated that pristine type P3HT aggregates decrease with

increasing F_4-TCNQ loading and optical spectra show increased J-type exciton coupling indicating increased chain planarity (intra-chain order).[143,144] The emergence of a new, ordered mixed phase reported by Duong et al. at the expense of pristine P3HT aggregates confirms this assignment.[131] At larger dopant loading, all pristine aggregates are converted to this mixed phase and doping efficiency plateaus, as observed in EPR data in Figure 5.1.
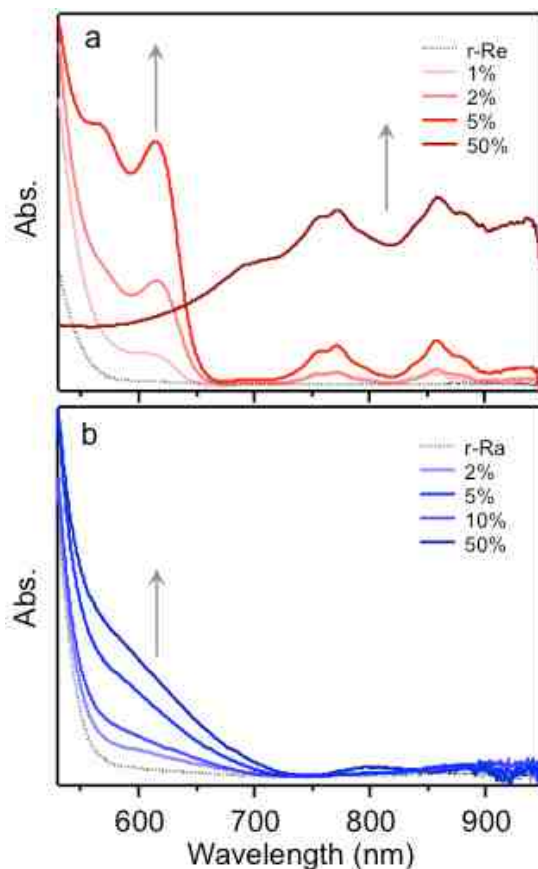
Figure 5.7: Optical absorption spectra of F_4-TCNQ doped a) r-Re and b) r-Ra P3HT solution normalized to the P3HT maximum.

Conversely, addition of F_4-TCNQ to r-Ra P3HT samples shows barely discernible F_4-TCNQ anion transitions above backgrounds similar with trends observed in EPR spectra in Figure 5.2b. A weak and broadened transition does appear on the red onset of the pristine-type singlet exciton transition suggesting a charge transfer complex type absorption band.[145] Alternatively, this band might correspond to transitions from tightly bound charges following integer charge transfer but seems unlikely since evidence of free charges would be expected at larger F_4-TCNQ loadings.
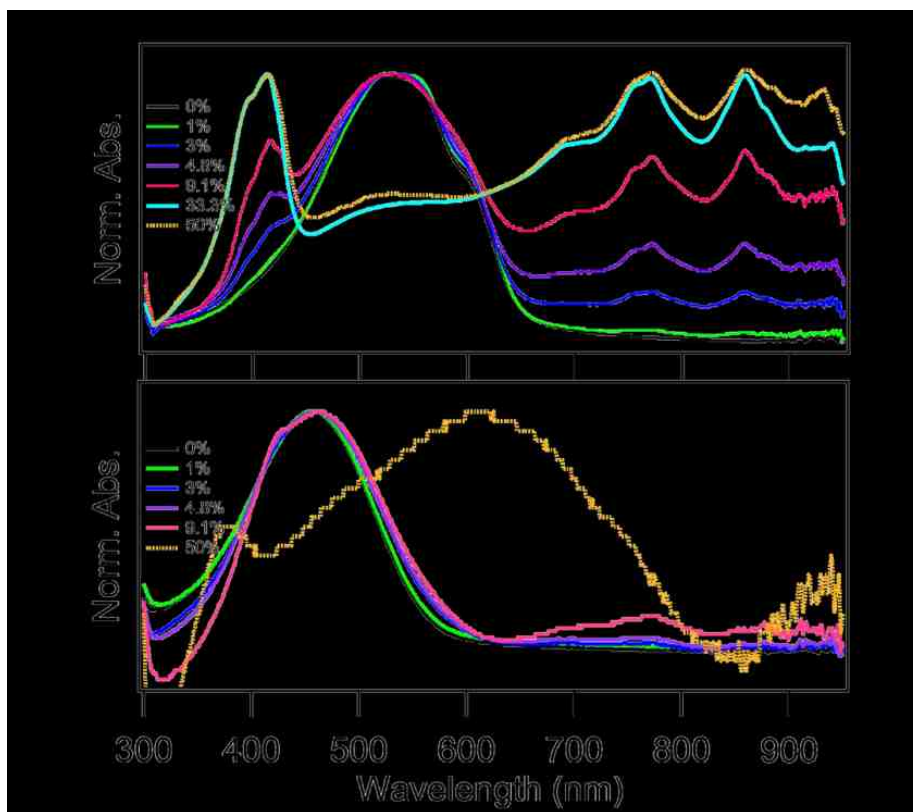
Figure 5.8: Optical absorption spectra of F_4-TCNQ doped a) r-Re and b) r-Ra P3HT thin films normalized to the P3HT maximum.

5.6 Near Infrared Absorption Raman Spectroscopy

Unfortunately, optical spectra do not provide conclusive evidence of the exact nature of P3HT/F_4-TCNQ interactions and whether the integer charge transfer model strictly applies to both types of P3HT forms. Additional insight into the roles of P3HT conformation and aggregation properties on doping efficiency can be obtained from Raman spectroscopy. Figure 5.9 shows Raman spectra of r-Re and r-Ra P3HT solutions with varying amounts of F_4-TCNQ are measured using NIR laser excitation (λ_{exc} =780 nm). This excitation wavelength is off resonance with P3HT optical transitions ensuring that excited state contributions from P3HT are negligible. Comparison between r-Re and r-Ra samples (Figures 5.9a and 5.9b, respectively) show noteworthy differences in lineshapes as well as their dependence on dopant loading. Doped r-Re P3HT samples exhibit large changes in the characteristic backbone stretching region (~1370—1515 cm^{-1}) with the appearance of a shoulder on the blue edge of the dominant C=C symmetric stretch (~1450 cm^{-1}) in addition to clusters of lower frequency modes in the region of the pristine C-C symmetric stretch (~1370 cm^{-1}). Dopant-induced changes in Raman spectra are similar to previous reports of polythiophene doped electrochemically or using other dopants (e.g., I_2 and HNO_3) and it is generally believed that the polymer backbone undergoes quinoidal distortions to stabilize charge.[146-151]

Raman spectra from r-Ra samples with varying F_4-TCNQ content show significant changes with addition of the dopant. However, features from pristine r-Ra are still discernible while r-Re spectra show drastic changes upon addition of even small amounts of F_4-TCNQ and almost complete loss of the pristine form. Transitions from F_4-

TCNQ anions appear in r-Re spectra, namely, peaks at ~1400 and ~1650 cm^{-1} gain in intensity with increased dopant loading (see Figure 5.8a)[152,153] but these features are considerably weaker in r-Ra P3HT samples indicating that free charges are not present in significant amounts. It is also interesting to note that the Raman excitation wavelength is now on resonance with the F_4-TCNQ anion absorption observed only in doped r-Re samples (Figure 5.9c), which may suggest some resonance enhancement contribution from this species. Although we do not attempt to assign the new features in Raman spectra, the lack of free charges in doped r-Ra P3HT could likely explain the differences in Raman spectra for these two forms.

Raman spectra from r-Ra samples with varying F_4-TCNQ content do in fact show significant changes with addition of the dopant. However, features from pristine r-Ra are still discernible while r-Re spectra show drastic changes upon addition of even small amounts of F_4-TCNQ and almost complete loss of the pristine form. Transitions from F_4-TCNQ appear in r-Re spectra, namely, peaks at ~1400 and ~1650 cm^{-1} with increased dopant loading (see Figure 5.9a)[152,153] but these features are considerably weaker in r-Ra P3HT samples indicating that free charges are not present in significant amounts. It is also interesting to note that the Raman excitation wavelength comes on resonance with the F_4-TCNQ anion absorption observed only in doped r-Re samples (Figure 5.8a), which may suggest some resonance enhancement contribution from this species. Although we do not attempt to assign the new features in Raman spectra, the lack of free charges in doped r-Ra P3HT could likely explain the differences in Raman spectra for these two forms due to resonance enhancement effects from F_4-TCNQ anions in doped r-Re forms.
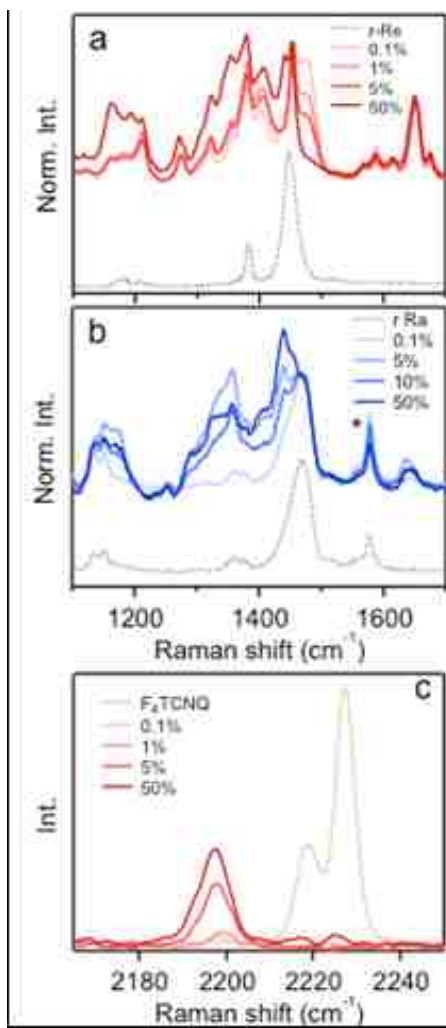
Figure 5.9: Raman spectra of F_4-TCNQ doped a) r-Re, and b) r-Ra P3HT chlorobenzene solutions at selected dopant loadings (λ_{exc} =780 nm). Asterisk denotes a chlorobenzene (solvent) Raman peak. c) Raman spectra of doped r-Re P3HT in the region of the CN stretch of F_4-TCNQ.

The data demonstrate thus far that while charge transfer interactions occur for both r-Re and r-Ra forms, charge separation and, therefore, efficient doping is only

appreciable in r-Re samples. The apparent preference of the dopant for P3HT aggregates is consistent with the fact that these chains already exist in ordered (planarized) conformations corresponding to lower torsional reorganizational barriers to adopt the quinoid form expected in the new phase.[154] We further speculate that F_4-TCNQ most likely interacts with dangling or looping chains on the periphery of nascent aggregates in solution and subsequent hole injection is promoted by nearby ordered segments. Subsequent loss of pristine type aggregate precursors upon doping probably arises from increased P3HT chain rigidity that destabilizes these structures. Hole injection from delocalization along the P3HT backbone should also translate into fast relaxation processes and EPR signals from these carriers do not appear at room temperature, meaning that the characteristic EPR signal Figure 5.1 originates from the F_4-TCNQ anion owing to its highly localized nature. This view is consistent with optical spectra of P3HT polarons that are broad and weak with low energy lineshapes extending into the NIR region.[52,155] Similar dependences of doping efficiency with P3HT conformation and packing have also been reported in previous studies involving r-Re and r-Ra P3HT using small molecule dopants, such as I_2.[151] Namely, EPR spectra showed much stronger signals from doped r-Re P3HT samples indicating efficient charge separation and subsequent delocalization along the backbone.

5.7 Conclusion

Overall, we have demonstrated that P3HT aggregates are necessary for efficient charge transfer doping by F_4-TCNQ. Although r-Ra P3HT interacts with the dopant,

charge separation is poor and the system instead remains tightly bound as a complex. The results have significant implications for maximum doping efficiency, which can be limited by conventional solution processing where most of the P3HT chains are unaggregated. This may potentially be overcome by using self-assembly methods to fabricate semi-crystalline nanofibers[25] that enable reliable control of P3HT aggregation characteristics, such as intrachain order, and possibly doping efficiency.

CHAPTER 6

Future Work

6.1 Introduction

Based on the structural and electronic changes observed after formation of a charge transfer salt in P3HT/F$_4$-TCNQ research, studies using related donor acceptor systems were initiated. This research will be described below.

6.2 Preliminary Studies of New Charge Transfer Complex

In order to better understand how D/A interactions affect polymer structure, poly[2-methoxy-5-(3′,7′-dimethyloctyloxy)-1,4-phenylenevinylene] (MDMO-PPV) was blended with the strong electron acceptor 2,3-dichloro-5,6-dicyano-p-benzoquinone (DDQ). The LUMO of DDQ was 0.2 eV lower in energy than the HOMO of MDMO-PPV for an energetically favorable formation of a charge transfer salt. The data demonstrated an increase in population of a more ordered state of PPV after the formation of a charge transfer salt. Parashchuk et al. recently reported X-ray crystallography of a MEH-PPV blend which displayed an increase in order after interactions with the strong electron acceptor trinitrofluorinone (TNF).[156] The data verified that the polymer's bimodal distribution of species can be controlled with loadings in D/A blends.

MDMO-PPV mixed with DDQ displayed similar characteristics of integer charge transfer, as shown in the research of chapter five. A new low energy absorption band was observed in paramagnetic samples along with a red shift in frequency of the fundamental Raman mode. However, unlike P3HT, ordered structures are uncommon in MDMO-PPV due to its tendency toward amorphous conformations. A bimodal distribution of disordered and ordered species was observed previously by Kim et al.[157] Kohler et al. showed temperature dependence on the population of each species and measured the absorption of MDMO down to 77 K where the low energy species dominated the electronic transition.[158]

This chapter reviewed how to use MDMO-PPV/DDQ blends to control the bimodal distribution of ordered and disordered species at room temperature with different loadings of DDQ. EPR spectra revealed that the formation of radical ions in the D/A blends coincided with a red shift in optical absorption and changes in: ^{13}C NMR and ^{1}H NMR chemical shift, and phonon frequencies and relative intensities observed in pre-resonance Raman and IR spectroscopy. These observations suggested electron transfer resulted in structural relaxation of the polymer backbone and increased the population of a more ordered species of the polymer.

The interactions of PPV with acceptors were unclear. MDMO-PPV/PCBM interactions increased disorder in the chain; however, blends with stronger acceptors showed increased polymer chain order.[78,159] The formation of a charge transfer salt introduced a formal charge and an unpaired electron on the polymer backbone. Spectroscopy was used to point out the nuclear reorganization and the changes in

electronic structure of MDMO-PPV that occurred after salt formation. The formal charge on the radial species in charge transfer salts were stabilized by polymer structures with reduced torsional degrees of freedom. This can be described by a change in bonding order along the polymer backbone as observed in more quinoid type structures of PPV's. To test this theory, correlated spectroscopic methods were used to show the physical and electronic structure changes that occurred after the charge transfer salt was formed.

6.3 Electron Paramagnetic Resonance

To determine which conditions paramagnetic electrons were formed EPR measurements were attained. Figure 6.1 displays the EPR signal from a 1 : 1 (wt/wt) MDMO-PPV/DDQ thin film at room temperature. The inset displays EPR spectra of a 1 : 1 blend solution and that there was no signal from pristine forms of MDMO-PPV and DDQ.
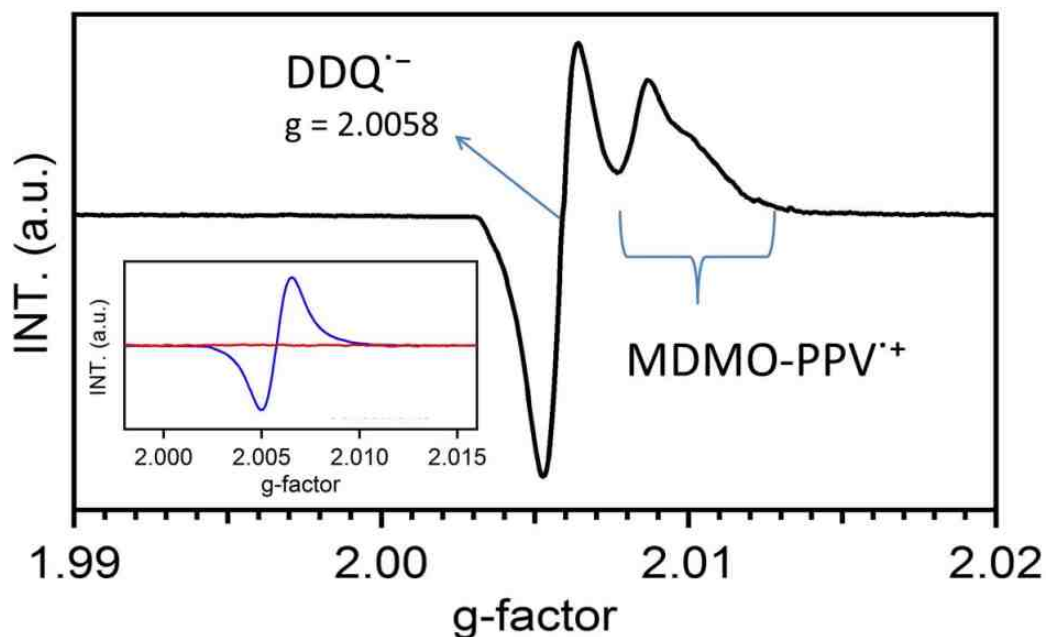
Figure 6.1: Room temperature spectra of 1 : 1 MDMO-PPV/DDQ thin film. Inset displays a 1 : 1 solution blend and the absence of signal in pristine samples.

The lineshape of the thin film blend sample resembled LEPR spectra recorded from MDMO-PVV/PCBM blends.[70,72,74] This type of lineshape resulted from overlapping signals of two paramagnetic species, the radical cation and anion. The lower g-value at 2.0058 was assigned to the DDQ anion from previous research that documented a 2.0052 g-value for DDQ.[138]
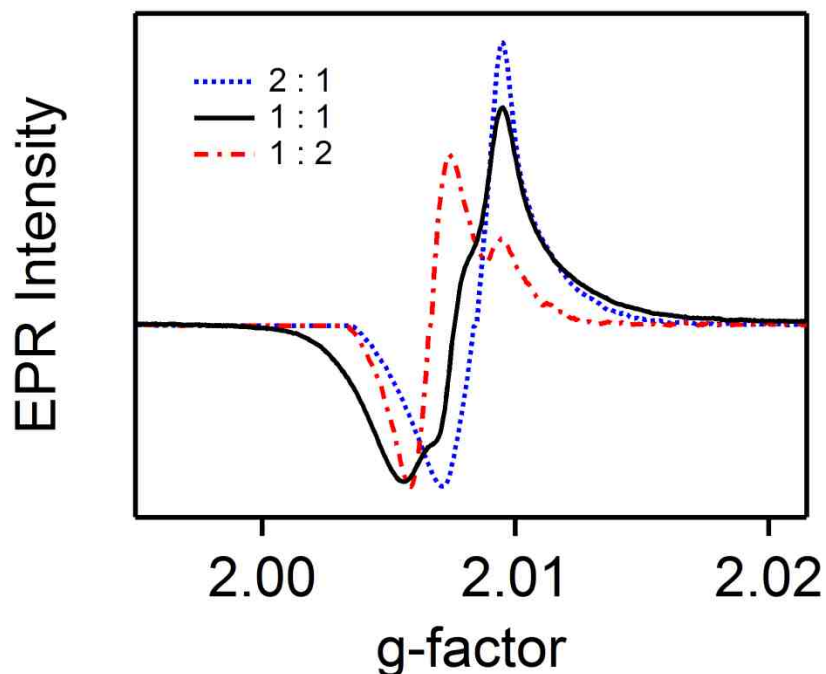
Figure 6.2: Low temperature (4K) EPR spectra from different loading of MDMO-PPV/DDQ thin films: 2 : 1 is blue dotted trace, 1 : 1 is black solid trace, and 0.5 : 1 is red dash-dot trace.

To further understand the origin of the EPR lineshape at room temperature, samples were placed in a LHe cryostat and variable temperatures were measured up from 4 K to room temperature. Displayed in Figure 6.2 is a clear shift to a higher g-value with a change in line shape as weight ratio of polymer increased to a lineshape that closely resembled a single derivative at the 2 : 1 ratio with a g-value of 2.0088. The spectra shifted toward the g-value assigned to DDQ as the polymer ratio decreased in the samples. This observation supported the earlier assignment of DDQ to g-value at 2.0058.
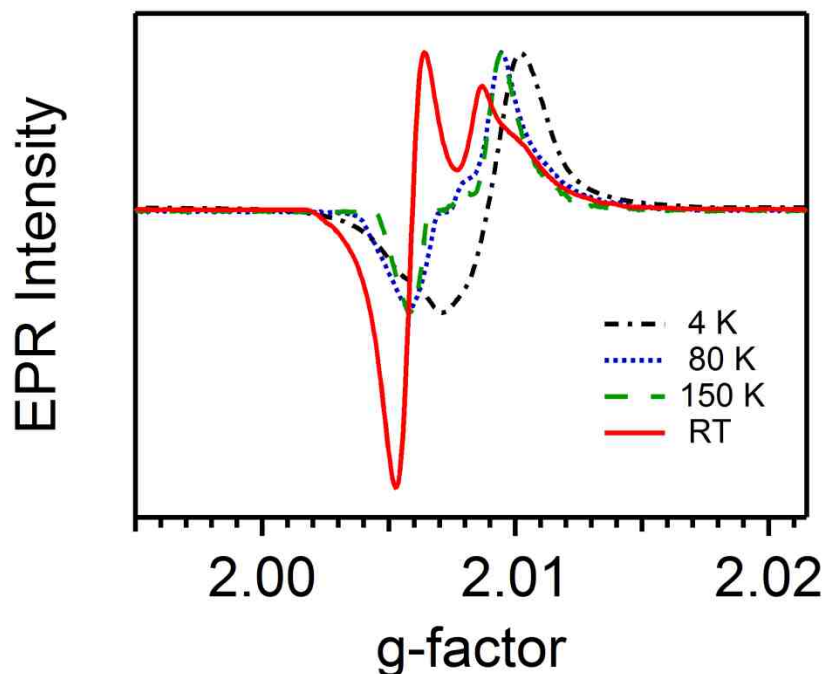
Figure 6.3: Variable temperature EPR spectra from 1 : 1 MDMO-PPV/DDQ blend thin films: room temperature is red solid trace, 150 K is green dashed trace, 80 K is blue dotted trace, and 4 K is black dash-dot-dot trace.

To further emphasize how the lineshapes changed, a variable temperature study of the 1 : 1 thin film sample was performed. Figure 6.3 displays a similar trend as Figure 6.2. This temperature dependent g-value shift behavior was indicative of two species with different electron spin relaxation rates.[160-162] ^{13}C and ^{1}H chemical shifts were used to evaluate structure changes in the paramagnetic samples.
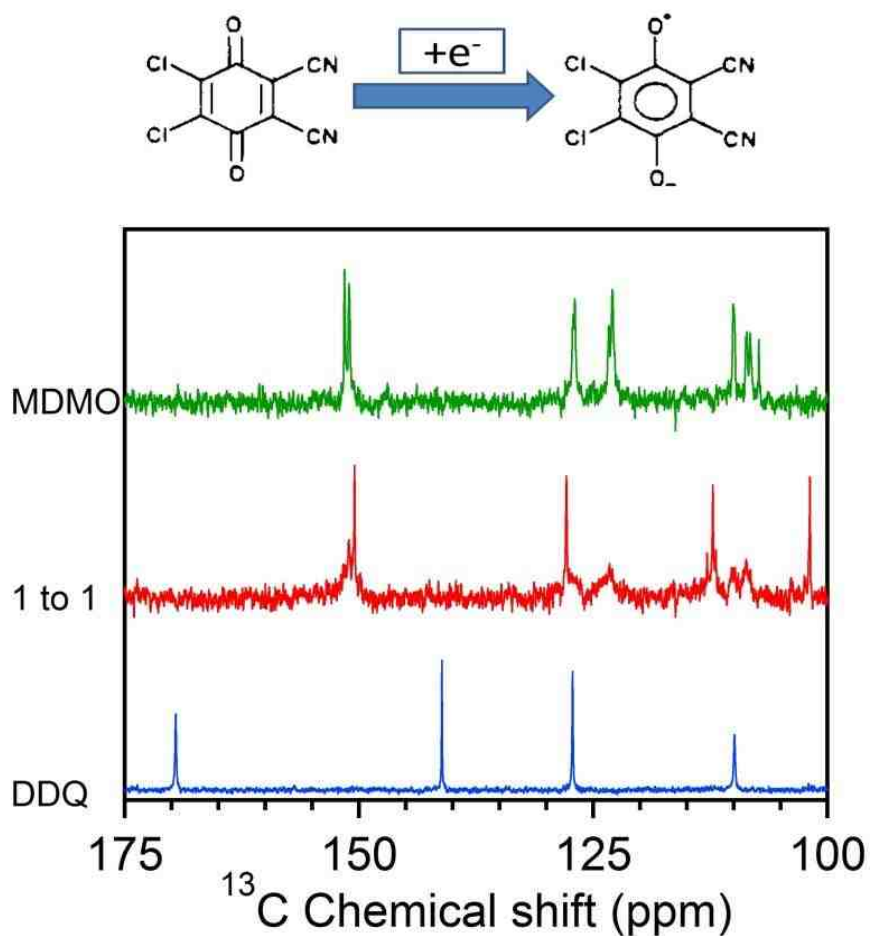
Figure 6.4: Bond rearrangement of reduced DDQ. ^{13}C NMR spectra in region of DDQ and the vinyl and phenyl carbons on the polymer backbone: pristine MDMO-PPV is green trace, MDMO-PPV/DDQ 1 : 1 wt/wt blend with concentration 5 mg/ml is red trace, and DDQ is blue trace.

Carbon NMR spectra confirmed nuclear reorganization of the DDQ molecule in blend mixtures. The four chemical shifts of DDQ at: 169.6, 142.3, 126.6, 108.4 ppm,

shown in blue trace, were not present in blend mixture (red trace) and four new chemical shifts were observed at 150.5, 127.8, 112.8, 101.9 ppm. The signal to noise ratio of the MDMO-PPV was poor in blend mixtures and changes were difficult to assign. Next ^{1}H NMR was used to look at proton chemical shifts on the polymer with the advantage that the DDQ molecule is absent of protons and signal changes will represent only effects of *D/A* interactions.
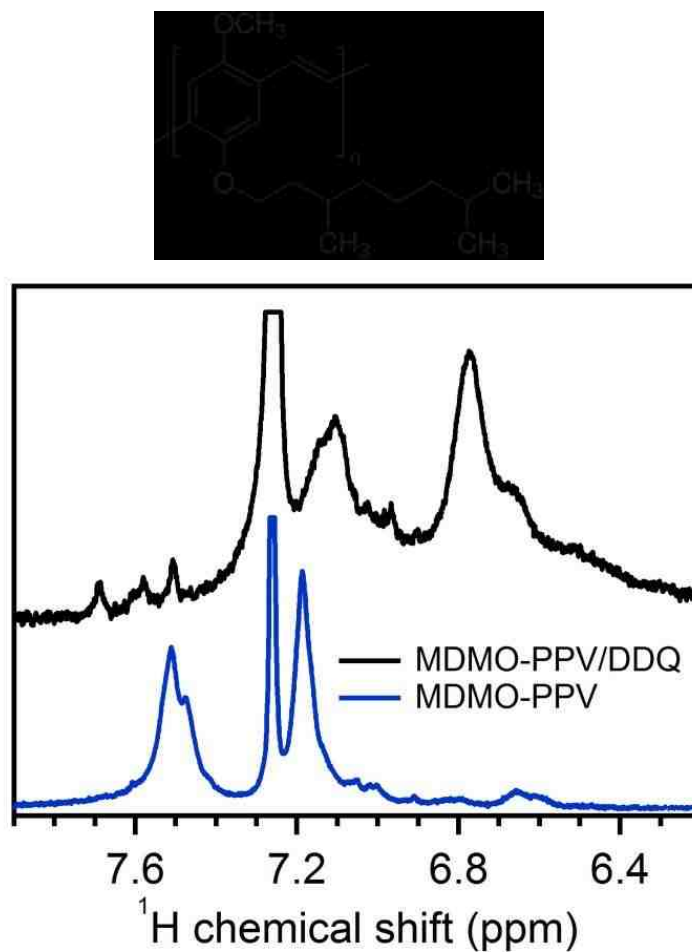
Figure 6.5: Structure of MDMO-PPV monomer and ^{1}H NMR spectra in region of vinyl and phenyl proton chemical shifts on the backbone of pristine MDMO-PPV (blue) and MDMO-PPV/DDQ 1 : 1 wt/wt (black).

In Figure 6.5 the spectra display the polymer backbone proton chemical shifts: vinyl at ~7.2 and phenyl at ~7.5 ppm. In the blend both peaks shifted up-field ~0.4 ppm. The increase in electron density on the atoms may have resulted from a decrease in the

out of plane motion of the protons. The truncated peak at 7.26 ppm was from the small amount of $CDCl_3$ added to the blend solution sample for a lock signal. Deviations in the permanent dipole moment of the vinyl proton out of plane wag at ~ 960 cm^{-1} were evaluated with IR spectroscopy to help understand changes in the proton chemical shift, displayed in Figure 6.6.

<u>6.5 Infrared and Raman Spectroscopy</u>
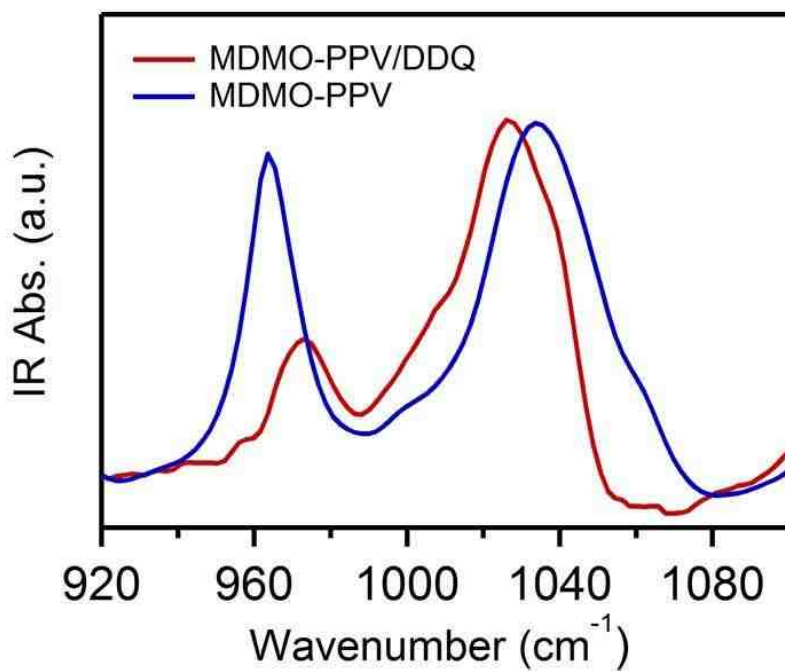
Figure 6.6: IR spectra from thin film samples of the out of plane proton wag on the vinyl group. Blue trace is pristine MDMO-PPV, red trace is the 1 : 1 MDMO-PPV/DDQ blend.

The large change in relative intensity of the 960 cm^{-1} frequency between pristine film and blend film displayed in Figure 6.6 was indicative of less out of plane distortions in the polymer chains. The full range of IR spectra are displayed in Figure 6.7 to relate the changes in ^{13}C NMR DDQ to changes in the DDQ C=O vibration at 1670 cm^{-1}.
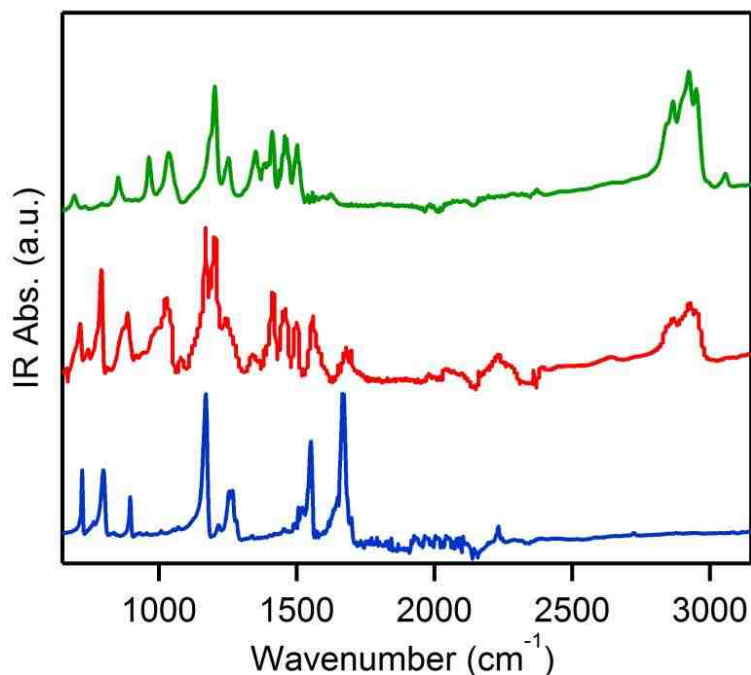
Figure 6.7: IR spectra from thin film samples: MDMO-PPV is green trace, 1 : 1 MDMO-PPV/DDQ blend is red trace, and DDQ is the blue trace. Note C=O peak at 1670 cm^{-1} reduce in relative intensity in blend film.

The change in relative intensity of the peak at 1670 cm^{-1} from DQQ (blue trace) to 1 : 1 (red trace) blend coincided with the changes observed in ^{13}C NMR chemical shifts. The diagram of bond changes after charge transfer in DDQ displayed in Figure

6.4 showed the expected transition of the DDQ from a quinone to a benzone. The π bond of the C=O was broken down to a single bond to accommodate the charge and the unpaired electron. Next, pre-resonance Raman spectroscopy was used to show changes in Raman scattering that resulted from the accommodation of unpaired electrons and formal charges on the polymer backbone.
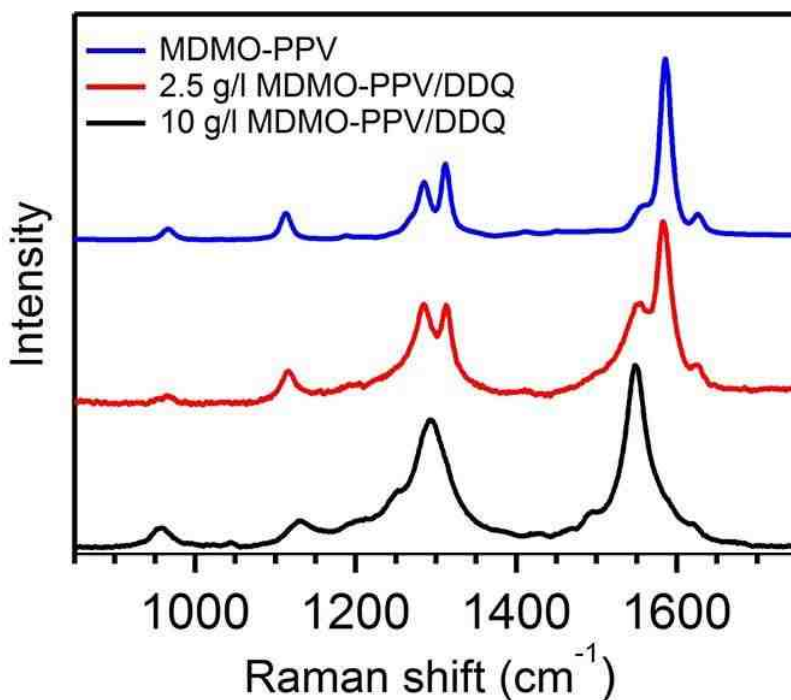
Figure 6.8: 780 nm Raman spectra from thin film samples: MDMO-PPV is blue, MDMO-PPV/DDQ 2 : 1 is red, and 1 : 1 is black.

Figure 6.8 displays 780 nm Raman spectra of pristine MDMO-PPV and different blend ratios. The DDQ Raman cross section was much lower than MDMO-PPV which rendered DDQ bands indistinguishable in blend spectra. Increased DDQ loadings

revealed two overlapping sets of vibrational modes from two different species. The red shift in the fundament transition mode, the symmetric stretching vibrations of the phenyl ring from 1580 to 1550 cm^{-1} was the most apparent This large change may be attributed to a shift of the polymer backbone structure to more of a quinoid type bond order. Other characteristic changes represented this as well. The relative intensity of the vinyl symmetric stretching vibrations at 1310 and 1280 cm^{-1} shifted to favor the lower energy mode and the out of plane C-H bending mode of the vinyl group red shifted 8 cm^{-1} in frequency. These changes in vibrational frequencies of the polymer backbone were all consistent with the data presented thus far that showed a more planar state was favored by the introduction of charge radicals to the polymer backbone.
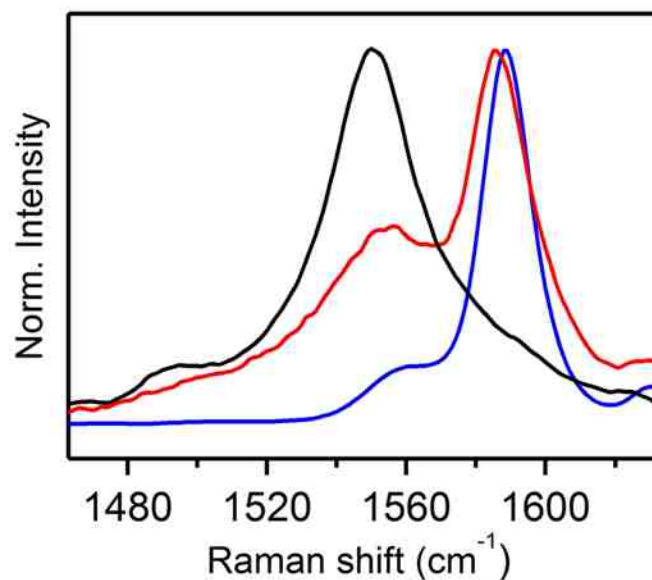
Figure 6.9: Raman spectra of fundament transition mode of MDMO-PPV from 780 nm excitation of neat MDMO-PPV (blue) and MDMO-PPV/DDQ 1 : 1 (red) and 1 : 2 (black.).

Figure 6.9 is important for modeling the species transition in MDMO-PPV. Similar to the Lorentzian lineshape fit method used in chapters three and four to deconvolute the Raman fundamental transition at 1450 and 1470 cm^{-1} of P3HT, a similar approach with MDMO-PPV could be implemented to determine relative amounts of ordered and disorder species. This leaves exciting work for my group members to dive into.
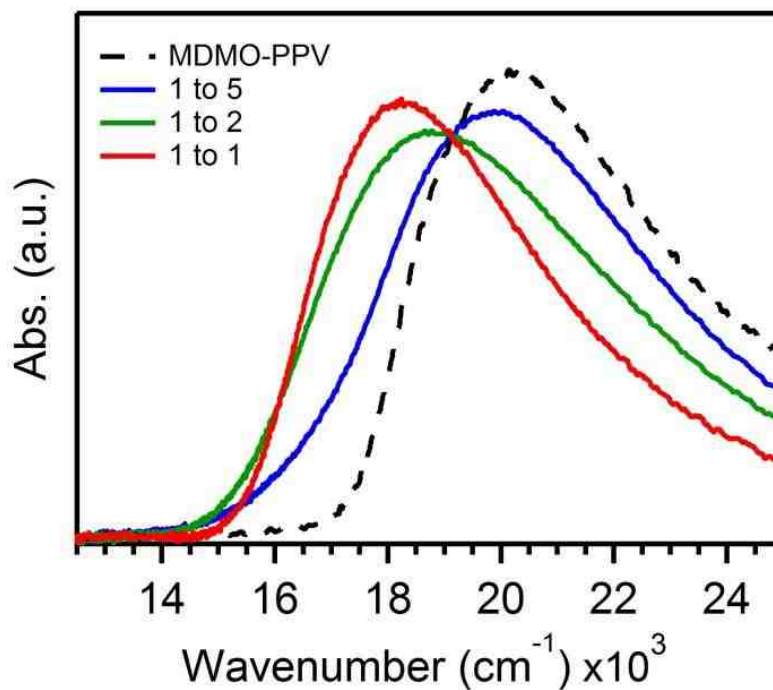
Figure 6.10: (a) Thin film absorption of neat MDMO-PPV (black dotted trace) and MDMO-PPV/DDQ blends (solid traces) cast from chlorobenzene solutions with constant MDMO concentration of 2.5 mg/ml.   (b) Solution absorption spectra of MDMO-PPV/DDQ blends at different loadings solution spectra.

The optical absorption spectra will be reviewed to tie in changes of electronic transitions with the structure changes presented thus far. Figure 6.10 displays thin film absorption spectra of varied blend ratios. An isosbestic point was presented to highlight the absorption lineshape alterations that resulted from the change in population of two distinct species, one shifted to lower energy from the other. The new optical transition resulted from a change in structure of the polymer backbone that led to an increase in

116

effective conjugation lengths. Figure 6.11 shows the interactions happen in solution and were retained after the solution processing.
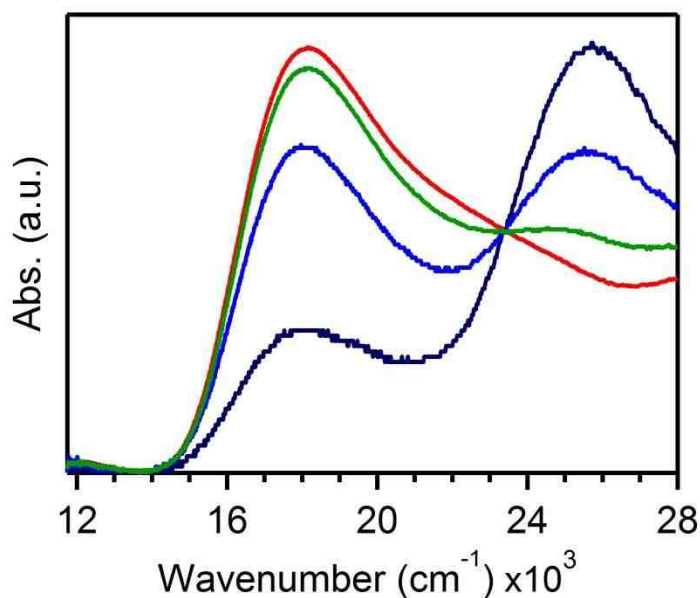
Figure 6.11: Room temperature spectra of 1 : 1 MDMO-PPV/DDQ thin film. Inset displays solution blend and the absence of signal in pristine samples.

6.7 Conclusion

This chapter presented spectroscopic evidence that ground state charge transfer in MDMO-PPV/DDQ blends promoted structural relaxation of the polymer backbone and a change in species of the polymer from a disorder blue conformation to a more ordered red one. The structure changes were correlated to paramagnetic resonance and a low energy electronic transition. The data demonstrated change in D/A structures that

resulted from the nuclear reorganization required to stabilize the ions on the D/A molecules after the formation of a paramagnetic species with a formal charge.

APPENDICES

APPENDIX A

Supporting information for Chapter 3

A.1 Nanofiber Exciton Coupling Theory

In modeling P3HT p-stacks within NF's or thin films we assume a 3-polymer stack as shown in Figure A.1. Each chain within the stack is described using a coarse-grained one-dimensional Wannier exciton Hamiltonian including vibronic coupling as described in detail in Reference.[87] To parameterize each chain we take the electron (t_e) and hole (t_h) transfer integrals connecting the LUMO's and HOMO's on neighboring thiophene units to satisfy, $t_e = t_h = 0.18\ eV$, while the difference in the electron-hole binding energy for an electron/hole pair within a single thiophene unit and an electron/hole pair on neighboring units is 1 eV. The resulting intrachain coupling is therefore significantly reduced compared with polydiacetylene (PDA).[87] The difference is in large part due to the effective nature of $t \equiv (t_e = t_h)$ in the present calculation; t is considered to be the mean electron and hole transfer integral, reduced by intrachain disorder (torsional defects) compared with the intrinsic value exhibited by single-chain PDA polymerized in situ from the monomer crystal, in which defects are virtually absent.[163]
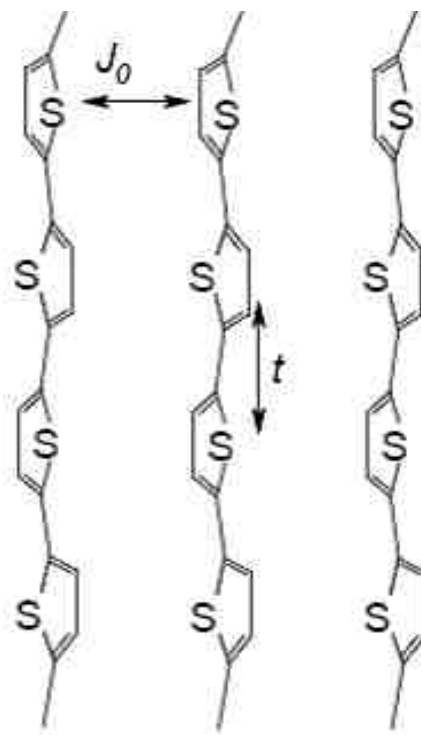
Figure A.1: A π-stack showing intra- (t) and inter (J_0) thiophene electronic interactions (reference144.)

In order to describe vibronic coupling to the symmetric vinyl stretching mode at approximately 0.17 eV (1400 cm^{-1}) within a given chain we take the HR factor describing the nuclear displacement associated with an electron/hole excitation within a single thiophene unit to be 1.6. As shown in Reference 84 increasing t results in an increase in the 0-0 absorption peak relative to the 0-1 peak, as is characteristic of J-aggregates. The *effective* HR factor for a single chain, as determined from the ratio of the 0-0 and 0-1 peaks, therefore decreases with t. Given the single unit HR factor of 1.6 and our assumed value of $t = 0.18 \ eV$ results in an effective HR factor close to unity, in agreement with

experiments on isolated P3HT chains, which show the 0-0 and 0-1 peaks to be approximately equal.[92] (We further take the HR factors for the ionic states of the thiophene unit to be half the neutral value, i.e. 0.8. However, because the intrachain coupling is weak, the resulting absorption and emission spectra are almost entirely independent of the ionic HR factors, unlike the case for PDA – see reference. 84).

The Hamiltonian used to describe the p-stack is given by,

$$H_{\pi-stack} = \sum_s \hat{H}_s + \sum_s \sum_n J_0 \{|n,s><n,s+1| + |n,s+1><n,s|\} \quad \text{(A.1)}$$

where H_s represents the Wannier-like Hamiltonian for the sth chain (s =1,2,3) given in Reference 84, $|n,s>$ represents an electron-hole excitation on the nth thiophene unit of the sth chain. In the current calculation we assume long-range inhomogeneous broadening such that the electron/hole excitations energies are the same for all three chains. We further assume periodic boundary conditions.

In Equation A.1 the through-space, interchain coupling J_0 is limited to adjacent (same n) thiophene units on neighboring chains. With this simplification the interchain exciton bandwidth is $W = 4J_0$, as in the H-aggregate model. In reality, a given thiophene unit on one chain interacts with *all* thiophene units on another. The absorption spectrum depends only on the $k = 0$ interaction sum, denoted as $\tilde{J}_{n,n}(k = 0)$, which is the sum of interactions between all thiophene units on one chain and a given thiophene unit on a neighboring one (assuming periodic boundary conditions). In our simplified Hamiltonian we have, $\tilde{J}_{n,n}(k = 0) = J_0$, and therefore view J_0 as the *effective* through-space interaction between two chains, representing the entire inter-chain sum.

Several analyses have shown that $\tilde{J}_{n,n}(k=0)$ reduces to practically zero as the chain length increases to infinity.[95-97] Hence, short oligomers interact more strongly than polymers. Using the simplified Hamiltonian in Equation A.1, small oligomers are distinguished from larger polymers by adjusting the value of the effective interaction, J_0. The value of J_0 is ultimately determined empirically by comparing the calculated $0-0/0-1$ absorption spectral ratio using Equation A.1 with the experimentally measured value. For the NF's in the present study such an analysis yields J_0 to be approximately 100 cm^{-1}, significantly smaller than the value of 400 cm^{-1} used to model thin films (see Figure. 3.11a). From this we conclude that the conjugation lengths of the polymers involved in p-stacking are significantly greater within the NF's.

As the insert in Figure 3.11b shows the 0-0 PL intensity at $T = 0\ K$ is zero. This is due to the symmetry-forbidden nature of the 0-0 transition in H-aggregates in the absence of disorder, which was assumed in our model. Increasing temperature allows emission from the thermally excited $(k = 0)$ exciton which can terminate on the vibrationless ground state, thereby adding intensity in the $0-0$ region of the PL spectrum. Hence the $0-0/0-1$ peak ratio grows with temperature as observed in the inset of Figure 3.11b.

REFERENCES CITED

124

(1)   Chang, J.-F.; Sun, B.; Breiby, D. W.; Nielsen, M. M.; Soelling, T. I.; Giles, M.; McCulloch, I.; Sirringhaus, H. *Chem. Mater.* **2004**, *16*, 4772.

(2)   Osterbacka, R.; An, C. P.; Jiang, X. M.; Vardeny, Z. V. *Synth. Met.* **2001**, *116*, 317.

(3)   Zhao, K.; Xue, L.; Liu, J.; Gao, X.; Wu, S.; Han, Y.; Geng, Y. *Langmuir* **2010**, *26*, 471.

(4)   Shirakawa, H.; Louis, E. J.; MacDiarmid, A. G.; Chiang, C. K.; Heeger, A. J. *Journal of the Chemical Society, Chemical Communications* **1977**, *0*, 578.

(5)   Tang, C. W. *Applied Physics Letters* **1986**, *48*, 183.

(6)   Prosa, T. J.; Winokur, M. J.; McCullough, R. D. *Macromolecules* **1996**, *29*, 3654.

(7)   Walzer, K.; Maennig, B.; Pfeiffer, M.; Leo, K. *Chemical Reviews* **2007**, *107*, 1233.

(8)   Lüssem, B.; Riede, M.; Leo, K. *physica status solidi (a)* **2013**, *210*, 9.

(9)   Mityashin, A.; Olivier, Y.; Van Regemorter, T.; Rolin, C.; Verlaak, S.; Martinelli, N. G.; Beljonne, D.; Cornil, J.; Genoe, J.; Heremans, P. *Advanced Materials* **2012**, *24*, 1535.

(10)   Pingel, P.; Neher, D. *Physical Review B* **2013**, *87*, 115209.

(11)   Loiudice, A.; Rizzo, A.; Biasiucci, M.; Gigli, G. *The Journal of Physical Chemistry Letters* **2012**, *3*, 1908.

(12)   Yang, C.; Orfino, F. P.; Holdcroft, S. *Macromolecules* **1996**, *29*, 6510.

(13)   Al-Ibrahim, M.; Roth, H. K.; Schroedner, M.; Konkin, A.; Zhokhavets, U.; Gobsch, G.; Scharff, P.; Sensfuss, S. *Organic Electronics* **2005**, *6*, 65.

(14)   Oregan, B.; Gratzel, M. *Nature* **1991**, *353*, 737.

(15)   Baldo, M. A.; Thompson, M. E.; Forrest, S. R. *Nature (London)* **2000**, *403*, 750.

(16)   Seoul, C.; Kim, N.-H. *Fibers Polym.* **2000**, *1*, 25.

(17)   Zhang, R.; Li, B.; Iovu, M. C.; Jeffries-El, M.; Sauvé, G.; Cooper, J.; Jia, S.; Tristram-Nagle, S.; Smilgies, D. M.; Lambeth, D. N.; McCullough, R. D.; Kowalewski, T. *Journal of the American Chemical Society* **2006**, *128*, 3480.

(18)   Bao, Z.; Dodabalapur, A.; Lovinger, A. J. *Applied Physics Letters* **1996**, *69*, 4108.

(19)   Chua, L.-L.; Zaumseil, J.; Chang, J.-F.; Ou, E. C. W.; Ho, P. K. H.; Sirringhaus, H.; Friend, R. H. *Nature (London, United Kingdom)* **2005**, *434*, 194.

(20)   Gross, M.; Muller, D. C.; Nothofer, H. G.; Scherf, U.; Neher, D.; Brauchle, C.; Meerholz, K. *Nature* **2000**, *405*, 661.

(21)   Horowitz, G. *Adv. Mater. (Weinheim, Ger.)* **1998**, *10*, 365.

(22)   Sandberg, H. G. O.; Frey, G. L.; Shkunov, M. N.; Sirringhaus, H.; Friend, R. H.; Nielsen, M. M.; Kumpf, C. *Langmuir* **2002**, *18*, 10176.

(23)   Umeda, T.; Hashimoto, Y.; Mizukami, H.; Shirakawa, T.; Fujii, A.; Yoshino, K. *Synthetic Metals* **2005**, *152*, 93.

(24)   Zaumseil, J.; Donley, C. L.; Kim, J.-S.; Friend, R. H.; Sirringhaus, H. *Advanced Materials (Weinheim, Germany)* **2006**, *18*, 2708.

(25)   Vukmirovic, N.; Wang, L.-W. *J. Phys. Chem. B* **2009**, *113*, 409.

(26)   Lan, Y.-K.; Huang, C.-I. *J. Phys. Chem. B* **2009**, *113*, 14555.

(27)   Gao, Y.; Grey, J. K. *J. Am. Chem. Soc.* **2009**, *131*, 9654.

(28)   Gao, Y.; Martin, T. P.; Thomas, A. K.; Grey, J. K. *The Journal of Physical Chemistry Letters* **2009**, *1*, 178.

(29)   Maillard, A.; Rochefort, A. *Phys. Rev. B: Condens. Matter Mater. Phys.* **2009**, *79*, 115207/1.

(30)   Melis, C.; Colombo, L.; Mattoni, A. *The Journal of Physical Chemistry C* **2011**, *115*, 576.

(31)   Nelson, J.; Kwiatkowski, J. J.; Kirkpatrick, J.; Frost, J. M. *Acc. Chem. Res.* **2009**, *42*, 1768.

(32)   Spano, F. C. *J. Chem. Phys.* **2005**, *122*, 234701.

(33)   Spano, F. C. *Chem. Phys.* **2006**, *325*, 22.

(34)   Chen, T.-A.; Wu, X.; Rieke, R. D. *J. Am. Chem. Soc.* **1995**, *117*, 233.

(35)   Louarn, G.; Trznadel, M.; Buisson, J. P.; Laska, J.; Pron, A.; Lapkowski, M.; Lefrant, S. *J. Phys. Chem.* **1996**, *100*, 12532.

(36)   Oosterbaan, W. D.; Bolsée, J.-C.; Gadisa, A.; Vrindts, V.; Bertho, S.; D'Haen, J.; Cleij, T. J.; Lutsen, L.; McNeill, C. R.; Thomsen, L.; Manca, J. V.; Vanderzande, D. *Adv. Funct. Mater.* **2010**, *20*, 792.

(37)   Chang, J.-F.; Clark, J.; Zhao, N.; Sirringhaus, H.; Breiby, D. W.; Andreasen, J. W.; Nielsen, M. M.; Giles, M.; Heeney, M.; McCulloch, I. *Phys. Rev. B* **2006**, *74*, 115318.

(38)   Yang, H.; Shin, T. J.; Yang, L.; Cho, K.; Ryu, C. Y.; Bao, Z. *Adv. Funct. Mater.* **2005**, *15*, 671.

(39)   Yang, H.; Shin, T. J.; Bao, Z.; Ryu, C. Y. *J. Polym. Sci., Part B: Polym. Phys.* **2007**, *45*, 1303.

(40)   Wu, P.-T.; Xin, H.; Kim, F. S.; Ren, G.; Jenekhe, S. A. *Macromolecules* **2009**, *42*, 8817.

(41)   Sirringhaus, H.; Brown, P. J.; Friend, R. H.; Nielsen, M. M.; Bechgaard, K.; Langeveld-Voss, B. M. W.; Spiering, A. J. H.; Janssen, R. A. J.; Meijer, E. W.; Herwig, P.; de Leeuw, D. M. *Nature* **1999**, *401*, 685.

(42)   Shimomura, T.; Takahashi, T.; Ichimura, Y.; Nakagawa, S.; Noguchi, K.; Heike, S.; Hashizume, T. *Phys. Rev. B* **2011**, *83*, 115314.

(43)   Pascui, O. F.; Lohwasser, R.; Sommer, M.; Thelakkat, M.; Thurn-Albrecht, T.; Saalwaὶˆchter, K. *Macromolecules* **2010**, *43*, 9401.

(44)   Clark, J.; Silva, C.; Friend, R. H.; Spano, F. C. *Phys. Rev. Lett.* **2007**, *98*, 206406/1.

(45)   Newbloom, G. M.; Kim, F. S.; Jenekhe, S. A.; Pozzo, D. C. *Macromolecules* **2011**, *44*, 3801.

(46)   Cheng, H.-L.; Lin, J.-W.; Jang, M.-F.; Wu, F.-C.; Chou, W.-Y.; Chang, M.-H.; Chao, C.-H. *Macromolecules* **2009**, *42*, 8251.

(47)   Spano, F. C.; Clark, J.; Silva, C.; Friend, R. H. *J. Chem. Phys.* **2009**, *130*, 074904/1.

(48)   Sandstedt, C. A.; Rieke, R. D.; Eckhardt, C. J. *Chem. Mater.* **1995**, *7*, 1057.

(49)   Gao, Y.; Martin, T. P.; Niles, E. T.; Wise, A. J.; Thomas, A. K.; Grey, J. K. *The Journal of Physical Chemistry C* **2010**, *114*, 15121.

(50)   Kasha, M. *RADIATION. RESEARCH* **1963**, *20*, 55.

(51)   Clark, J.; Chang, J.-F.; Spano, F. C.; Friend, R. H.; Silva, C. *Appl. Phys. Lett.* **2009**, *94*, 163306/1.

(52)   Brown, P. J.; Sirringhaus, H.; Harrison, M.; Shkunov, M.; Friend, R. H. *Physical Review B* **2001**, *63*, 125204.

(53)   Parkinson, P.; MuÌ^ller, C.; Stingelin, N.; Johnston, M. B.; Herz, L. M. *J. Phys. Chem. Lett.* **2010**, *1*, 2788.

(54)   Roehling, J. D.; Arslan, I.; Moule, A. J. *J. Mater. Chem.*, *22*, 2498.

(55)   Knupfer, M. *Appl. Phys. A: Mater. Sci. Process. FIELD Full Journal Title:Applied Physics A: Materials Science & Processing* **2003**, *77*, 623.

(56)   Scully, S. R.; McGehee, M. D. *Journal of Applied Physics* **2006**, *100*, 034907/1.

(57)   Quist, P. A. C.; Sweelssen, J.; Koetse, M. M.; Savenije, T. J.; Siebbeles, L. D. A. *J. Phys. Chem. C* **2007**, *111*, 4452.

(58)   Coakley, K. M.; Liu, Y.; McGehee, M. D. *Polymer Preprints (American Chemical Society, Division of Polymer Chemistry)* **2004**, *45*, 207.

(59)   Kline, R. J.; McGehee, M. D.; Toney, M. F. *PMSE Preprints* **2005**, *92*, 611.

(60)   Ma, W.; Yang, C.; Gong, X.; Lee, K.; Heeger, A. J. *Adv. Funct. Mater.* **2005**, *15*, 1617.

(61)   Yu, G.; Heeger, A. J. *Journal of Applied Physics* **1995**, *78*, 4510.

(62)   Onoda, M.; Tada, K.; Zakhidov, A. A.; Yoshino, K. *Thin Solid Films* **1998**, *331*, 76.

(63)   Kohler, A.; Dos Santos, D. A.; Beljonne, D.; Shuai, Z.; Bredas, J. L.; Holmes, A. B.; Kraus, A.; Mullen, K.; Friend, R. H. *Nature (London)* **1998**, *392*, 903.

(64)   Mayer, A. C.; Toney, M. F.; Scully, S. R.; Rivnay, J.; Brabec, C. J.; Scharber, M.; Koppe, M.; Heeney, M.; McCulloch, I.; McGehee, M. D. *Advanced Functional Materials* **2009**, *19*, 1173.

(65)   Stamires, D. N.; Turkevich, J. *Journal of the American Chemical Society* **1963**, *85*, 2557.

(66)   Soos, Z. G. *Annual Review of Physical Chemistry* **1974**, *25*, 121.

(67)   Sariciftci, N. S.; Braun, D.; Zhang, C.; Srdanov, V. I.; Heeger, A. J.; Stucky, G.; Wudl, F. *Applied Physics Letters* **1993**, *62*, 585.

(68)   Sariciftci, N. S.; Smilowitz, L.; Heeger, A. J.; Wudl, F. *Science* **1992**, *258*, 1474.

(69)   Mulliken, R. S. *The Journal of Chemical Physics* **1939**, *7*, 20.

(70)   Konkin, A. L.; Sensfuss, S.; Roth, H. K.; Nazmutdinova, G.; Schroedner, M.; Al-Ibrahim, M.; Egbe, D. A. M. *Synthetic Metals* **2005**, *148*, 199.

(71)   Murata, K.; Shimoi, Y.; Abe, S.; Kuroda, S.; Noguchi, T.; Ohnishi, T. *Chemical Physics* **1998**, *227*, 191.

(72)   Ceuster, J. D.; Goovaerts, E.; Bouwen, A.; Hummelen, J. C.; Dyakonov, V. *Physical Review B* **2001**, *64*, 195206.

(73)   Krinichnyi, V. I.; Yudanova, E. I. *AIP Advances* **2011**, *1*, 022131.

(74)   Schultz, N. A.; Scharber, M. C.; Brabec, C. J.; Sariciftci, N. S. *Physical Review B* **2001**, *64*, 245210.

(75)   Rosokha, S. V.; Kochi, J. K. *Accounts of Chemical Research* **2008**, *41*, 641.

(76)   Banerji, N.; Cowan, S.; Vauthey, E.; Heeger, A. J. *The Journal of Physical Chemistry C* **2011**, *115*, 9726.

(77)   Muller, J. G.; Lupton, J. M.; Feldmann, J.; Lemmer, U.; Scharber, M. C.; Sariciftci, N. S.; Brabec, C. J.; Scherf, U. *Phys. Rev. B: Condens. Matter Mater. Phys.* **2005**, *72*, 195208/1.

(78)   Bruevich, V. V.; Makhmutov, T. S.; Elizarov, S. G.; Nechvolodova, E. M.; Paraschuk, D. Y. *The Journal of Chemical Physics* **2007**, *127*, 104905.

(79)   Parashchuk, O. D.; Bruevich, V. V.; Paraschuk, D. Y. *Physical Chemistry Chemical Physics* **2010**, *12*, 6021.

(80)   Marcus, R. A. *The Journal of Chemical Physics* **1956**, *24*, 966.

(81)   Marcus, R. A. *The Journal of Chemical Physics* **1984**, *81*, 4494.

(82)   Marcus, R. A. *Annual Review of Physical Chemistry* **1964**, *15*, 155.

(83)   Tretiak, S.; Saxena, A.; Martin, R. L.; Bishop, A. R. *Phase Transitions* **2002**, *75*, 725.

(84)   Brinkmann, M. *J. Polym. Sci., Part B: Polym. Phys.*, *49*, 1218.

(85)   Brown, P. J.; Thomas, D. S.; Kohler, A.; Wilson, J. S.; Kim, J.-S.; Ramsdale, C. M.; Sirringhaus, H.; Friend, R. H. *Phys. Rev. B: Condens. Matter Mater. Phys.* **2003**, *67*, 064203/1.

(86)   Spano, F. C. *Acc. Chem. Res.* **2010**, *43*, 429.

(87)   Yamagata, H.; Spano, F. C. *J. Chem. Phys.* **2011**, *135*, 054906/1.

(88)   Spano, F. C.; Yamagata, H. *J. Phys. Chem. B* **2011**, *115*, 5133.

(89)   Lecuiller, R.; Berrehar, J.; Ganiere, J. D.; Lapersonne-Meyer, C.; Lavallard, P.; Schott, M. *Phys. Rev. B: Condens. Matter Mater. Phys.* **2002**, *66*, 125205/1.

(90)   Tsoi, W. C.; James, D. T.; Kim, J. S.; Nicholson, P. G.; Murphy, C. E.; Bradley, D. D. C.; Nelson, J.; Kim, J.-S. *J. Am. Chem. Soc.* **2011**, *133*, 9834.

(91)   Theander, M.; Svensson, M.; Ruseckas, A.; Zigmantas, D.; Sundstrom, V.; Andersson, M. R.; Inganas, O. *Chem. Phys. Lett.* **2001**, *337*, 277.

(92)   Kanemoto, K.; Sudo, T.; Akai, I.; Hashimoto, H.; Karasawa, T.; Aso, Y.; Otsubo, T. *Phys. Rev. B: Condens. Matter Mater. Phys.* **2006**, *73*, 235203/1.

(93)   Hess, B. C.; Kanner, G. S.; Vardeny, Z. *Physical Review B* **1993**, *47*, 1407.

(94)   Adachi, T.; Brazard, J.; Ono, R. J.; Hanson, B.; Traub, M. C.; Wu, Z.-Q.; Li, Z.; Bolinger, J. C.; Ganesan, V.; Bielawski, C. W.; Vanden Bout, D. A.; Barbara, P. F. *The Journal of Physical Chemistry Letters* **2011**, *2*, 1400.

(95)   Barford, W. *The Journal of Chemical Physics* **2007**, *126*, 134905.

(96)   Manas, E. S.; Spano, F. C. *J. Chem. Phys.* **1998**, *109*, 8087.

(97)   Cornil, J.; dos, S. D. A.; Crispin, X.; Silbey, R.; Bredas, J. L. *J. Am. Chem. Soc.* **1998**, *120*, 1289.

(98)   Schwartz, B. J. *Annu. Rev. Phys. Chem.* **2003**, *54*, 141.

(99)   Cornil, J.; Beljonne, D.; Calbert, J.-P.; Bredas, J.-L. *Adv. Mater. (Weinheim, Ger.)* **2001**, *13*, 1053.

(100)   Tessler, N.; Preezant, Y.; Rappaport, N.; Roichman, Y. *Adv. Mater. (Weinheim, Ger.)* **2009**, *21*, 2741.

(101)   Yah, W. O.; Wang, Z.; Otsuka, H.; Kato, K.; Kim, J.; Takata, M.; Takahara, A. *ACS Appl. Mater. Interfaces* **2009**, *1*, 1544.

(102)   Yang, X.; Lu, G.; Li, L.; Zhou, E. *Small* **2007**, *3*, 611.

(103)   Zhang, Y.; de Boer, B.; Blom, P. W. M. *Advanced Functional Materials* **2009**, *19*, 1901.

(104)   Guo, T.-F.; Wen, T.-C.; L'Vovich Pakhomov, G.; Chin, X.-G.; Liou, S.-H.; Yeh, P.-H.; Yang, C.-H. *Thin Solid Films* **2008**, *516*, 3138.

(105)   Li, G.; Shrotriya, V.; Huang, J.; Yao, Y.; Moriarty, T.; Emery, K.; Yang, Y. *Nat Mater* **2005**, *4*, 864.

(106)   Li, G.; Yao, Y.; Yang, H.; Shrotriya, V.; Yang, G.; Yang, Y. *Advanced Functional Materials* **2007**, *17*, 1636.

(107)   Chen, L.-M.; Hong, Z.; Li, G.; Yang, Y. *Advanced Materials* **2009**, *21*, 1434.

(108)   Guenes, S.; Neugebauer, H.; Sariciftci, N. S. *Chem. Rev. (Washington, DC, U. S.)* **2007**, *107*, 1324.

(109)   Peet, J.; Heeger, A. J.; Bazan, G. C. *Accounts of Chemical Research* **2009**, *42*, 1700.

(110)   Thompson, B. C.; Frechet, J. M. J. *Angew. Chem., Int. Ed.* **2008**, *47*, 58.

(111)   Kobayashi, T.; Hamazaki, J.-i.; Kunugita, H.; Ema, K.; Endo, T.; Rikukawa, M.; Sanui, K. *Physical Review B* **2003**, *67*, 205214.

(112)   Lapkowski, M.; Pron, A. *Synthetic Metals* **2000**, *110*, 79.

(113)   Zhokhavets, U.; Erb, T.; Gobsch, G.; Al-Ibrahim, M.; Ambacher, O. *Chemical Physics Letters* **2006**, *418*, 347.

(114)   Chen, C. W.; Chen, K. H.; Wu, J. J.; Pong, W. F.; Su, W. F.; Chen, L. C. *ECS Trans.* **2008**, *16*, 49.

(115)   Moulè̀ • , A. J.; Allard, S.; Kronenberg, N. M.; Tsami, A.; Scherf, U.; Meerholz, K. *The Journal of Physical Chemistry C* **2008**, *112*, 12583.

(116)   Janssen, G.; Aguirre, A.; Goovaerts, E.; Vanlaeke, P.; Poortmans, J.; Manca, J. *The European Physical Journal - Applied Physics* **2007**, *37*, 287.

(117)   Miller, S.; Fanchini, G.; Lin, Y.-Y.; Li, C.; Chen, C.-W.; Su, W.-F.; Chhowalla, M. *Journal of Materials Chemistry* **2008**, *18*, 306.

(118)   Louarn, G.; Buisson, J. P.; Lefrant, S.; Fichou, D. *The Journal of Physical Chemistry* **1995**, *99*, 11399.

(119)   Louarn, G.; Trznadel, M.; Zagorska, M.; Lapkowski, M.; Pron, A.; Buisson, J. P.; Lefrant, S. *Synthetic Metals* **1997**, *84*, 579.

(120)   Dante, M.; Peet, J.; Nguyen, T.-Q. *The Journal of Physical Chemistry C* **2008**, *112*, 7241.

(121)   Hoppe, H.; Niggemann, M.; Winder, C.; Kraut, J.; Hiesgen, R.; Hinsch, A.; Meissner, D.; Sariciftci, N. S. *Advanced Functional Materials* **2004**, *14*, 1005.

(122)   Huang, Y.-C.; Chuang, S.-Y.; Wu, M.-C.; Chen, H.-L.; Chen, C.-W.; Su, W.-F. *Journal of Applied Physics* **2009**, *106*, 034506.

(123)   Kaake, L. G.; Barbara, P. F.; Zhu, X. Y. *J. Phys. Chem. Lett.* **2010**, *1*, 628.

(124)   Kim, D. H.; Park, Y. D.; Jang, Y.; Kim, S.; Cho, K. *Macromol. Rapid Commun.* **2005**, *26*, 834.

(125)   Casado, J.; Zgierski, M. Z.; Ewbank, P. C.; Burand, M. W.; Janzen, D. E.; Mann, K. R.; Pappenfus, T. M.; Berlin, A.; PÃ©rez-Inestrosa, E.; Ortiz, R. o. P.; LÃ³pez Navarrete, J. T. *Journal of the American Chemical Society* **2006**, *128*, 10134.

(126)   Zerbi, G.; Magnoni, M. C.; Hoogmartens, I.; Kiebooms, R.; Carleer, R.; Vanderzande, D.; Gelan, J. *Advanced Materials* **1995**, *7*, 1027.

(127)   Pingel, P.; Schwarzl, R.; Neher, D. *Applied Physics Letters* **2012**, *100*, 143303.

(128)   Zhang, Y.; Blom, P. W. M. *Applied Physics Letters* **2010**, *97*, 083303.

(129)   Fujita, H.; Yuan, Y.; Michinobu, T. *Journal of Photopolymer Science and Technology* **2011**, *24*, 311.

(130)   Hu, J.; Clark, K. W.; Hayakawa, R.; Li, A.-P.; Wakayama, Y. *Langmuir* **2013**.

(131)   Duong, D. T.; Wang, C.; Antono, E.; Toney, M. F.; Salleo, A. *Organic Electronics* **2013**, *14*, 1330.

(132)   Jiang, X. M.; Österbacka, R.; Korovyanko, O.; An, C. P.; Horovitz, B.; Janssen, R. A. J.; Vardeny, Z. V. *Advanced Functional Materials* **2002**, *12*, 587.

(133)   Tsoi, W. C.; Spencer, S. J.; Yang, L.; Ballantyne, A. M.; Nicholson, P. G.; Turnbull, A.; Shard, A. G.; Murphy, C. E.; Bradley, D. D. C.; Nelson, J.; Kim, J.-S. *Macromolecules* **2011**, *44*, 2944.

(134)   Brédas, J. L.; Thémans, B.; Fripiat, J. G.; André, J. M.; Chance, R. R. *Physical Review B* **1984**, *29*, 6761.

(135)   Navarrete, J. T. L.; Zerbi, G. *The Journal of Chemical Physics* **1991**, *94*, 965.

(136)   Bredas, J. L.; Street, G. B. *Accounts of Chemical Research* **1985**, *18*, 309.

(137)   Brédas, J. L.; Wudl, F.; Heeger, A. J. *Solid State Communications* **1987**, *63*, 577.

(138)   Miller, J. S.; Krusic, P. J.; Dixon, D. A.; Reiff, W. M.; Zhang, J. H.; Anderson, E. C.; Epstein, A. J. *Journal of the American Chemical Society* **1986**, *108*, 4459.

(139)   Park, Y. D.; Lee, S. G.; Lee, H. S.; Kwak, D.; Lee, D. H.; Cho, K. *Journal of Materials Chemistry* **2011**, *21*, 2338.

(140)   Moulé, A. J.; Meerholz, K. *Advanced Materials* **2008**, *20*, 240.

(141)   Rainbolt, J. E.; Koech, P. K.; Polikarpov, E.; Swensen, J. S.; Cosimbescu, L.; Von Ruden, A.; Wang, L.; Sapochak, L. S.; Padmaperuma, A. B.; Gaspar, D. J. *Journal of Materials Chemistry C* **2013**, *1*, 1876.

(142)   Galya, L. G.; McCord, E. F.; Adamsons, K. *International Journal of Polymer Analysis and Characterization* **1996**, *2*, 293.

(143)   Gao, J.; Roehling, J. D.; Li, Y.; Guo, H.; Moulé, A. J.; Grey, J. K. **2013**.

(144)   Niles, E. T.; Roehling, J. D.; Yamagata, H.; Wise, A. J.; Spano, F. C.; Moule, A. J.; Grey, J. K. *J. Phys. Chem. Lett.* **2012**, *3*, 259.

(145)   Panda, P.; Veldman, D.; Sweelssen, J.; Bastiaansen, J. J. A. M.; Langeveld-Voss, B. M. W.; Meskers, S. C. J. *The Journal of Physical Chemistry B* **2007**, *111*, 5076.

(146)   Yong, C.; Renyuan, Q. *Solid State Communications* **1985**, *54*, 211.

(147)   Cao, Y.; Guo, D.; Pang, M.; Qian, R. *Synthetic Metals* **1987**, *18*, 189.

(148)   Tashiro, K.; Kobayashi, M.; Kawai, T.; Yoshino, K. *Polymer* **1997**, *38*, 2867.

(149)   Li, Y.; Qian, R. *Synthetic Metals* **1993**, *53*, 149.

(150)   Elsenbaumer, R. L.; Jen, K. Y.; Miller, G. G.; Shacklette, L. W. *Synthetic Metals* **1987**, *18*, 277.

(151)   Ukai, S.; Ito, H.; Marumoto, K.; Kuroda, S.-i. *Journal of the Physical Society of Japan* **2005**, *74*, 6.

(152)   Kim, J.-S.; Lee, S.-K.; Lee, H.-J.; Noh, D.-Y. *The Bulletin of the Korean Chemical Society* **2010**, *31*, 4.

(153)   Kuzmany, H.; Stolz, H. J. *Journal of Physics C: Solid State Physics* **1977**, *10*, 2241.

(154)   Roncali, J. *Macromolecular Rapid Communications* **2007**, *28*, 1761.

(155)   Österbacka, R.; An, C. P.; Jiang, X. M.; Vardeny, Z. V. *Science* **2000**, *287*, 839.

(156)   Parashchuk, O. D.; Grigorian, S.; Levin, E. E.; Bruevich, V. V.; Bukunov, K.; Golovnin, I. V.; Dittrich, T.; Dembo, K. A.; Volkov, V. V.; Paraschuk, D. Y. *The Journal of Physical Chemistry Letters* **2013**, *4*, 1298.

(157)   Kim, D. Y.; Grey, J. K.; Barbara, P. F. *Synthetic Metals* **2006**, *156*, 336.

(158)   Köhler, A.; Hoffmann, S. T.; Bässler, H. *Journal of the American Chemical Society* **2012**, *134*, 11594.

(159)   Wise, A. J.; Grey, J. K. *Physical Chemistry Chemical Physics* **2012**, *14*, 11273.

(160)   Khakhar, M. P.; Prabhananda, B. S.; Das, M. R. *Journal of the American Chemical Society* **1967**, *89*, 3100.

(161)   Ji-Liang, S.; Cheng-Ming, Z.; Hu-Nan, Y.; Zhi-Hai, Q.; Yao-Hong, F.; Xi-Kui, J. *Chinese Journal of Chemistry* **1998**, *16*, 397.

(162)   Sensfuss, S.; Al-Ibrahim, M. *Opt. Sci. Eng. FIELD Full Journal Title:Optical Science and Engineering* **2005**, *99*, 529.

(163)   Schott, M. **2006**, *edited by G. Lanzani (Wiley-VCH, Weinheim, 2006)*, 49.